



ANNUAL
REVIEWS **Further**

Click [here](#) to view this article's online features:

- Download figures as PPT slides
- Navigate linked references
- Download citations
- Explore related articles
- Search keywords

The Eccentric Kozai-Lidov Effect and Its Applications

Smadar Naoz

Department of Physics and Astronomy, University of California, Los Angeles,
California 90095; email: snaoz@astro.ucla.edu

Annu. Rev. Astron. Astrophys. 2016. 54:441–89

First published online as a Review in Advance on
July 29, 2016

The *Annual Review of Astronomy and Astrophysics* is
online at astro.annualreviews.org

This article's doi:
[10.1146/annurev-astro-081915-023315](https://doi.org/10.1146/annurev-astro-081915-023315)

Copyright © 2016 by Annual Reviews.
All rights reserved

Keywords

dynamics, binaries, triples, exoplanets, stellar systems, black holes

Abstract

The hierarchical triple-body approximation has useful applications to a variety of systems from planetary and stellar scales to supermassive black holes. In this approximation, the energy of each orbit is separately conserved, and therefore the two semimajor axes are constants. On timescales much larger than the orbital periods, the orbits exchange angular momentum, which leads to eccentricity and orientation (i.e., inclination) oscillations. The orbits' eccentricity can reach extreme values, leading to a nearly radial motion, which can further evolve into short orbit periods and merging binaries. Furthermore, the orbits' mutual inclinations may change dramatically from pure prograde to pure retrograde, leading to misalignment and a wide range of inclinations. This dynamical behavior is coined the “eccentric Kozai-Lidov mechanism.” The behavior of such a system is exciting, rich, and chaotic in nature. Furthermore, these dynamics are accessible from a large part of the triple-body parameter space and can be applied to a diverse range of astrophysical settings and used to gain insights into many puzzles.

Contents

1. INTRODUCTION	442
2. THE HIERARCHICAL THREE-BODY SECULAR APPROXIMATION	444
2.1. Physical Picture	447
2.2. Circular Outer Body	448
2.3. Eccentric Outer Orbit	453
3. THE VALIDITY OF THE APPROXIMATION AND THE STABILITY OF THE SYSTEM	462
4. SHORT-RANGE FORCES AND OTHER ASTROPHYSICAL EFFECTS	465
4.1. General Relativity	465
4.2. Tides and Rotation	468
5. APPLICATIONS	470
5.1. Solar System	470
5.2. Planetary Systems	471
5.3. Stellar Systems	476
5.4. Compact Objects	480
6. BEYOND THE THREE-BODY SECULAR APPROXIMATION	483
7. SUMMARY	484

1. INTRODUCTION

Triple systems are common in the Universe. They are found in many different astrophysical settings covering a large range of mass and physical scales, such as triple stars (e.g., Tokovinin 1997, 2014a,b; Eggleton et al. 2007) and accreting compact binaries with a companion (for example, companions to X-ray binaries; e.g., Grindlay et al. 1988, Prodan & Murray 2012). In addition, it seems that supermassive black hole binaries and higher multiples are common, and thus any star in their vicinity forms a triple system (e.g., Valtonen 1996, Di Matteo et al. 2005, Khan et al. 2012, Kulkarni & Loeb 2012). Furthermore, considering the Solar System, binaries composed of near-Earth objects, asteroids, or dwarf planets (of which a substantial fraction seems to reside in a binary configuration; e.g., Polishook & Brosh 2006, Nesvorný et al. 2011, Margot et al. 2015) naturally form a triple system with our Sun. Lastly, hot Jupiters are likely to have a faraway companion, forming a triple system of a star-hot Jupiter binary with a distant perturber (e.g., Knutson et al. 2014, Ngo et al. 2015, Wang et al. 2015). Stability requirements yield that most of these systems are hierarchical in scale, with a tight inner binary orbited by a tertiary on a wider orbit, forming the outer binary. Therefore, in most cases the dynamical behavior of these systems takes place on timescales much longer than the orbital periods.

The study of secular perturbations (i.e., long-term phase-averaged evolution over timescales longer than the orbital periods) in triple systems can be dated back to Lagrange, Laplace and Poincaré. Many years later, the study of secular hierarchical triple system was addressed by Lidov (1961, where the English translation version was published only in 1962). He studied the orbital evolution of artificial satellites that was caused by gravitational perturbations from an axisymmetric outer potential. A short time after that, Kozai (1962) studied the effects of Jupiter’s gravitational perturbations on an inclined asteroid in our own Solar System. In these settings a relatively tight inner binary composed of a primary and a secondary (in these initial studies it was assumed to be a test particle) is orbited by a faraway companion. We denote the inner (outer) orbit semimajor axis

as a_1 (a_2). In this setting the secular approximation can be utilized. This implies that the energy of each orbit is conserved separately (as well as is the energy of the entire system); thus, a_1 and a_2 are constants during the evolution. The dynamical behavior is a result of angular momentum exchange between the two orbits. Kozai (1962), for example, expanded the three-body Hamiltonian in semimajor axis ratio (because the outer orbit is far away, a_1/a_2 is a small parameter). He then averaged over the orbits, and lastly he truncated the expansion to the lowest order, called the quadrupole, which is proportional to $(a_1/a_2)^2$. Both Kozai (1962) and Lidov (1962) found that the inner test particle's inclination and eccentricity oscillate on timescales much larger than its orbital period. In these studies the outer perturber was assumed to carry most of the angular momentum, and thus under the assumption of an axisymmetric outer potential the inner and outer orbits' z -components of the angular momenta (along the total angular momentum) are conserved. This led to large variations between the eccentricity and inclination of the test particle orbit.

Although the Kozai-Lidov mechanism seemed interesting it was largely ignored for many years. However, about 15–20 years ago, probably correlating with the detection of the eccentric planet 6 Cyg B (Cochran et al. 1996) or the close-to-perpendicular stellar Algol system (Eggleton et al. 1998, Baron et al. 2012), the Kozai-Lidov mechanism received its deserved attention. However, though the mechanism seemed very promising in addressing these astrophysical phenomena, it was limited to the narrow parts of the parameter space (favoring close-to-perpendicular initial orientation between the two orbits; e.g., Marchal 1990, Morbidelli 2002, Valtonen & Karttunen 2006, Fabrycky & Tremaine 2007) and produced only moderate eccentricity excitations. Most of the studies that investigated different astrophysical applications of the Kozai-Lidov mechanism used the Kozai (1962) and Lidov (1962) test particle, axisymmetric outer orbit quadrupole-level approximation or TPQ approximation.

This approximation has an analytical solution that describes (for initially highly inclined orbits $\sim 40^\circ$ – 140° ; see below) the large amplitude oscillations between the inner orbit's eccentricity and inclination with respect to the outer orbit (e.g., Kinoshita & Nakai 1999, Morbidelli 2002). These oscillations have well-defined maximum and minimum eccentricities and inclinations and limit the motion to either prograde ($\leq 90^\circ$) or retrograde ($\geq 90^\circ$) with respect to the outer orbit. The axisymmetric outer orbit quadrupole-level approximation is applicable for an ample number of systems. For example, this approximation has appropriately described the motion of Earth's artificial satellites under the influence of gravitational perturbations from the moon (e.g., Lidov 1962). Other astrophysical systems for which this approximation is applicable include (but are not limited to) the effects of the Sun's gravitational perturbation on planetary satellites, because in this case indeed the satellite mass is negligible compared to the other masses in the system, and the planet's orbit around the Sun is circular. Indeed, the axisymmetric outer orbit quadrupole-level approximation can successfully be used to study the inclination distribution of the Jovian irregular satellites (e.g., Carruba et al. 2002, Nesvorný et al. 2003) or in general the survival of planetary outer satellites (e.g., Kinoshita & Nakai 1991), as well as the dynamical evolution of the orbit of a Kuiper Belt object satellite due to perturbation from the Sun (e.g., Perets & Naoz 2009, Naoz et al. 2010). This approximation is useful and can be applied in the limit of a circular outer orbit and a test particle inner object.

Recently, Naoz et al. (2011, 2013a) showed that relaxing either one of these assumptions leads to qualitatively different dynamical evolution. Considering systems beyond the test particle approximation, or a circular orbit, requires the next level of approximation, called the octupole level of approximation (e.g., Harrington 1968, 1969; Ford et al. 2000b; Blaes et al. 2002). This level of approximation is proportional to $(a_1/a_2)^3$. In the octupole level of approximation, the inner orbit eccentricity can reach extremely high values and does not have a well-defined value, as

the system is chaotic in general (Ford et al. 2000b; Naoz et al. 2013a; Teyssandier et al. 2013; Li et al. 2014a,b). In addition, the inner orbit inclination can flip its orientation from prograde, with respect to the total angular momentum, to retrograde (Naoz et al. 2011). We refer to this process as the eccentric Kozai-Lidov (EKL) mechanism. We follow the literature-coined acronym “EKL” as opposed to the more chronologically accurate acronym “ELK.”

As is discussed below the EKL mechanism taps into larger parts of the parameter space (i.e., beyond the $\sim 40^\circ$ – 140° range) and results in a richer and far more exciting dynamical evolution. As a consequence this mechanism is applicable to a wide range of systems that allow for eccentric orbits or three massive bodies, from exoplanetary orbits over stellar interactions to black hole dynamics. The prospect of forming eccentric or short-period planets through three-body interactions was the source of many studies (e.g., Innanen et al. 1997; Wu & Murray 2003; Fabrycky & Tremaine 2007; Wu et al. 2007; Veras & Ford 2010; Batygin et al. 2011; Correia et al. 2011; Naoz et al. 2011, 2012; Petrovich 2015a,b). It also promoted many interesting applications for stellar dynamics from stellar mergers (e.g., Perets & Fabrycky 2009, Naoz & Fabrycky 2014, Witzel et al. 2014, Stephan et al. 2016) to compact binary mergers that may prompt supernova explosions for double white dwarf (WD) mergers (e.g., Thompson 2011, Katz & Dong 2012) or gravitational wave (GW) emission for neutron star (NS) or black hole binary mergers (e.g., Blaes et al. 2002, Seto 2013).

2. THE HIERARCHICAL THREE-BODY SECULAR APPROXIMATION

In the three-body approximation, dynamical stability requires that either the system has circular, concentric, coplanar orbits or a hierarchical configuration, in which the inner binary is orbited by a third body on a much wider orbit, the outer binary (**Figure 1**). In this case the secular approximation (i.e., phase-averaged, long-term evolution) can be applied, where the interaction between two nonresonant orbits is equivalent to treating the two orbits as massive wires (e.g., Marchal 1990). Here the line density is inversely proportional to orbital velocity, and the two orbits torque each other and exchange angular momentum but not energy. Therefore the orbits can change shape and orientation (on timescales much longer than their orbital periods) but not semimajor axes of the orbits. The gravitational potential is then expanded in a semimajor axis ratio of a_1/a_2 , where a_1 (a_2) is the semimajor axis of the inner (outer) body (Kozai 1962, Lidov 1962). This ratio is a small parameter due to the hierarchical configuration.

The hierarchical three-body system consists of a tight binary (m_1 and m_2) and a third body (m_3). We define \mathbf{r}_{in} to be the relative position vector from m_1 to m_2 and \mathbf{r}_{out} the position vector of m_3 relative to the center of mass of the inner binary (see **Figure 1**). Using this coordinate system, the dominant motion of the triple can be reduced to two separate Keplerian orbits: the first describes the relative tight orbit of bodies 1 and 2, and the second describes the wide orbit of body 3 around the center of mass of bodies 1 and 2. The Hamiltonian for the system can be decomposed accordingly into two Keplerian Hamiltonians plus a coupling term that describes the (weak) interaction between the two orbits. Let the semimajor axes of the inner and outer orbits be a_1 and a_2 , respectively. Then the coupling term in the complete Hamiltonian can be written as a power series in the ratio of the semimajor axes, $\alpha = a_1/a_2$ (e.g., Harrington 1968). In a hierarchical system, by definition, this parameter α is small.

The complete Hamiltonian expanded in orders of α is (e.g., Harrington 1968)

$$\mathcal{H} = \frac{k^2 m_1 m_2}{2a_1} + \frac{k^2 m_3 (m_1 + m_2)}{2a_2} + \frac{k^2}{r_{\text{out}}} \sum_{n=2}^{n=\infty} \left(\frac{r_{\text{in}}}{r_{\text{out}}} \right)^n M_n P_n(\cos \Phi), \quad (1)$$

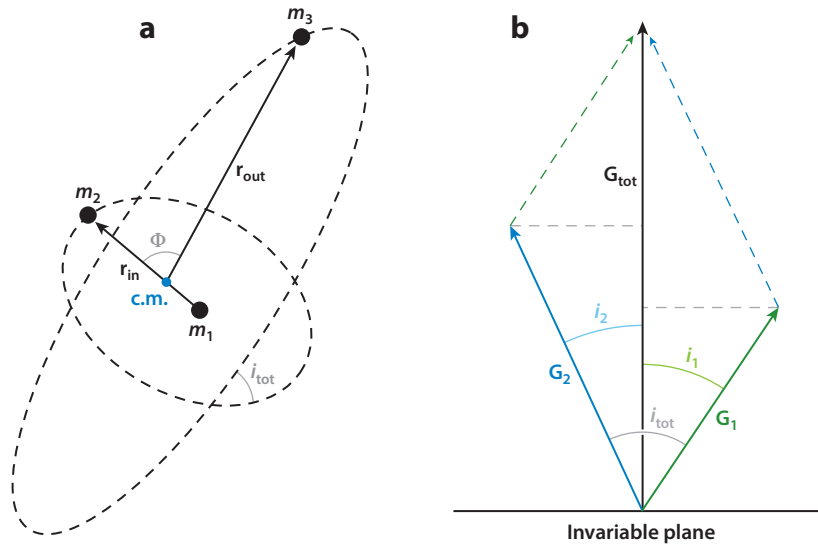


Figure 1

Schematic description of the coordinate system and the angles used (not to scale). (a) The three bodies and the relative vectors. Here “c.m.” denotes the center of mass of the inner binary, containing objects of masses m_1 and m_2 . The separation vector \mathbf{r}_{in} points from m_1 to m_2 ; \mathbf{r}_{out} points from the c.m. to m_3 . The angle between the vectors \mathbf{r}_{in} and \mathbf{r}_{out} is Φ . (b) Geometry of the angular momentum vectors and the definition of the relevant inclination angles. We show the total angular momentum vector (\mathbf{G}_{tot}), the angular momentum vector of the inner orbit (\mathbf{G}_1) with inclination i_1 with respect to \mathbf{G}_{tot} and the angular momentum vector of the outer orbit (\mathbf{G}_2) with inclination i_2 with respect to \mathbf{G}_{tot} . The angle between \mathbf{G}_1 and \mathbf{G}_2 defines the mutual inclination $i_{\text{tot}} = i_1 + i_2$. The invariable plane is perpendicular to \mathbf{G}_{tot} ; in other words, the z axis is parallel to \mathbf{G}_{tot} .

and in terms of the semimajor axes a_1 and a_2 , we have

$$\mathcal{H} = \frac{k^2 m_1 m_2}{2a_1} + \frac{k^2 m_3 (m_1 + m_2)}{2a_2} + \frac{k^2}{a_2} \sum_{n=2}^{\infty} \left(\frac{a_1}{a_2}\right)^n M_n \left(\frac{\mathbf{r}_{\text{in}}}{a_1}\right)^n \left(\frac{a_2}{\mathbf{r}_{\text{out}}}\right)^{n+1} P_n(\cos \Phi), \quad (2)$$

where k^2 is the gravitational constant, P_n are Legendre polynomials, Φ is the angle between \mathbf{r}_{in} and \mathbf{r}_{out} (see **Figure 1**), and

$$M_n = m_1 m_2 m_3 \frac{m_1^{n-1} - (-m_2)^{n-1}}{(m_1 + m_2)^n}. \quad (3)$$

The right term of Equation 2 is often called the perturbing function as it describes the gravitational perturbations between the two orbits. The two left terms in Equation 2 are simply the energy of the inner and outer Kepler orbits. Note that the sign convention for this Hamiltonian is positive.

The frame of reference chosen throughout this review is the invariable plane for which the z axis is set along the total angular momentum, which is conserved during the secular evolution of the system (see **Figure 1**) (e.g., Lidov & Ziglin 1974). Another description used in the literature is the vectorial form (e.g. Katz et al. 2011, Boué & Fabrycky 2014a), which has been proven useful for addressing different astrophysical settings. Considering the invariable plane it is convenient to adopt the canonical variables known as Delaunay’s elements (e.g., Valtonen & Karttunen 2006). These describe for each orbit three angles and three conjugate momenta.

The first set of angles are the mean anomalies, M_1 and M_2 (also often denoted in the literature as l_1 and l_2), which describe the position of the object in their orbit. Their conjugate momenta are

$$L_1 = \frac{m_1 m_2}{m_1 + m_2} \sqrt{k^2 (m_1 + m_2) a_1}, \quad (4)$$

$$L_2 = \frac{m_3 (m_1 + m_2)}{m_1 + m_2 + m_3} \sqrt{k^2 (m_1 + m_2 + m_3) a_2},$$

where subscripts 1 and 2 denote the inner and outer orbits, respectively. The second set of angles are the arguments of periastron, ω_1 and ω_2 (g_1 and g_2), which describe the position of the eccentricity vector (in the plane of the ellipse). Their conjugate momenta are the magnitude of the angular momenta vector of each orbit G_1 and G_2 (often used as J_1 and J_2):

$$G_1 = L_1 \sqrt{1 - e_1^2}, \quad G_2 = L_2 \sqrt{1 - e_2^2}, \quad (5)$$

where e_1 (e_2) is the inner (outer) orbit eccentricity. The last set of angles are the longitudes of ascending nodes, Ω_1 and Ω_2 (b_1 and b_2). Their conjugate momenta are

$$H_1 = G_1 \cos i_1, \quad H_2 = G_2 \cos i_2, \quad (6)$$

often denoted as $J_{1,z}$ and $J_{2,z}$. Note that G_1 and G_2 are the magnitudes of the angular momentum vectors (\mathbf{G}_1 and \mathbf{G}_2), and H_1 and H_2 are the z -components of these vectors (recall that the z axis is chosen to be along the total angular momentum \mathbf{G}_{tot}). In **Figure 1**, we show the configuration of the angular momentum vectors of the inner and outer orbit (\mathbf{G}_1 and \mathbf{G}_2 , respectively), and H_1 and H_2 are the z -components of these vectors, where the z axis is chosen to be along the total angular momentum \mathbf{G}_{tot} . This conservation of the total angular momentum G_{tot} yields a simple relation between the z -component of the angular momenta and the total angular momentum magnitude:

$$G_{\text{tot}} = H_1 + H_2. \quad (7)$$

The equations of motion are given by the canonical relations (for these equations, we use the l, g, b notation):

$$\frac{dL_j}{dt} = \frac{\partial \mathcal{H}}{\partial l_j}, \quad \frac{dl_j}{dt} = -\frac{\partial \mathcal{H}}{\partial L_j}, \quad (8)$$

$$\frac{dG_j}{dt} = \frac{\partial \mathcal{H}}{\partial g_j}, \quad \frac{dg_j}{dt} = -\frac{\partial \mathcal{H}}{\partial G_j}, \quad (9)$$

$$\frac{dH_j}{dt} = \frac{\partial \mathcal{H}}{\partial b_j}, \quad \frac{db_j}{dt} = -\frac{\partial \mathcal{H}}{\partial H_j}, \quad (10)$$

where $j = 1, 2$. Note that these canonical relations have the opposite sign relative to the usual relations (e.g., Goldstein 1950) because of the sign convention typically chosen for this Hamiltonian.

As apparent from the Hamiltonian Equation 2, if the semimajor axis ratio is indeed a small parameter, then for the zeroth approximation each orbit can be described as a Keplerian orbit for which its energy is conserved. Thus, we can average over the short timescale and focus on the long-term dynamics of the triple system. This process is known as the secular approximation, in which the energy (semimajor axis) is conserved, and the orbits exchange angular momentum. The short timescale's terms in the Hamiltonian depend on l_1 and l_2 , and eliminating them is done via a canonical transformation. The technique used is known as the von Zeipel transformation (Brouwer 1959). In this canonical transformation, a time-independent-generating function is defined to be periodic in l_1 and l_2 , which allows the elimination of the short-period terms in the Hamiltonian;

the details of this procedure are described by Naoz et al. (2013a, their appendix A2). Eliminating these angles from the Hamiltonian means that their conjugate momenta L_1 and L_2 are conserved (see Equation 8), thus yielding $a_1 = \text{Const.}$ and $a_2 = \text{Const.}$, as expected. In the most general case of this three-body secular approximation there are only two parameters that are conserved, i.e., the energy of the system (which also means that the energy of the inner and the outer orbits are conserved separately) and the total angular momentum G_{tot} .

The time evolution for the eccentricity and inclination of the system can easily be achieved from Equations 8–10:

$$\frac{de_j}{dt} = \frac{\partial e_j}{\partial G_j} \frac{\partial \mathcal{H}}{\partial g_j}, \quad (11)$$

and

$$\frac{d(\cos i_j)}{dt} = \frac{\dot{H}_j}{G_j} - \frac{\dot{G}_j}{G_j} \cos i_j, \quad (12)$$

where $j = 1$ and 2 for the inner and outer orbits, respectively. See the full set of the equations of motion in Equations 78–84 (see **Supplemental Text 1: The Secular Equations**; follow the **Supplemental Material link** from the Annual Reviews home page at <http://www.annualreviews.org>).

The lowest order of approximation, which is proportional to $(a_1/a_2)^2$, is called the quadrupole level, and we find that an artifact of the averaging process results in conservation of the outer orbit angular momentum G_2 ; in other words the system is symmetric for the rotation of the outer orbit. This was coined the “happy coincidence” by Lidov & Ziglin (1976, p. 475). Its significant consequence is that this approximation should be used only for an axisymmetric outer potential such as circular outer orbits (Naoz et al. 2013a).

The next level of approximation, the octupole, is proportional to $(a_1/a_2)e_2/(1-e_2^2)$ (see below), and thus the TPQ approximation can be successfully applied when this parameter is small for low inclinations (see below for numerical studies). However, close-to-perpendicular systems are extremely sensitive to this parameter.

A popular procedure that was done in earlier studies (e.g., Kozai 1962) used “elimination of nodes” (e.g., Jefferys & Moser 1966, p. 570). This describes the a simplification of the Hamiltonian by setting

$$b_1 - b_2 = \pi. \quad (13)$$

This relation holds in the invariable plane when the total angular momentum is conserved, such as in our case. Some studies that exploited explicitly this relation in the Hamiltonian incorrectly concluded (using Equation 10) that the z -components of the orbital angular momenta are always constant. As shown by Naoz et al. (2011, 2013a), this leads to qualitatively different evolution for the triple-body system. We can still use the Hamiltonian with the nodes eliminated, instead of using the canonical relations, as long as the equations of motion for the inclinations are derived from the total angular momentum conservation (Naoz et al. 2013a).

2.1. Physical Picture

Considering the quadrupole level of approximation (which is valid for axisymmetric outer orbit potential) for an inner test particle (either m_1 or m_2 goes to zero), the conserved quantities are the energy and the z -component of the angular momentum. In other words the Hamiltonian does not depend on longitude of ascending nodes (b_1 , also denoted as Ω_1), and thus the z -component of the inner orbit angular momentum, H_1 , is conserved and the system is integrable. In this case the equal precession rate of the inner orbit’s longitude of ascending nodes (Ω_1) and the longitude

 Supplemental Material

of the periapsis ($\varpi = \Omega_1 + \omega_1$) mean that an eccentric inner orbit feels an accumulating effect on the orbit. The resonant angle, $\omega_1 = \varpi_1 - \Omega_1$, will librate around 0° or 180° , which causes large amplitude eccentricity oscillations of the inner orbit.

In that case (circular outer orbit, in the test particle approximation, i.e., TPQ approximation) the conservation of the z -component of the angular momentum $j_z = \sqrt{1 - e_1^2} \cos i_{\text{tot}} = \text{Const.}$ yields oscillations between the eccentricity and inclination. The inner orbit is more eccentric for smaller inclinations and less eccentric for larger inclinations.

2.2. Circular Outer Body

In this case the gravitational potential set by the outer orbit is axisymmetric, and thus the quadrupole level of approximation describes the behavior of the hierarchical system well. We consider two possibilities: In the first, one of the members of the inner orbit is a test particle (i.e., either m_1 or m_2 is zero). In the second, we allow for all three masses to be nonnegligible.

2.2.1. Axisymmetric potential and inner test particle, test particle quadrupole. Following Lithwick & Naoz (2011), we call this case the TPQ approximation. Without loss of generality, we take $m_2 \rightarrow 0$; the Hamiltonian of this system is very simple and can be written as

$$\mathcal{H} = \frac{3}{8} k^2 \frac{m_1 m_3}{a_2} \left(\frac{a_1}{a_2} \right)^2 \frac{1}{(1 - e_2^2)^{3/2}} F_{\text{quad}}, \quad (14)$$

where

$$F_{\text{quad}} = -\frac{e_1^2}{2} + \theta^2 + \frac{3}{2} e_1^2 \theta^2 + \frac{5}{2} e_1^2 (1 - \theta^2) \cos(2\omega_1), \quad (15)$$

where $\theta = \cos i_{\text{tot}}$ (e.g., Yokoyama et al. 2003, Lithwick & Naoz 2011); note that, unlike the Hamiltonian that is presented in the next section (Equation 22), this Hamiltonian only describes the test particle.

At this physical setting the octupole level of approximation is zero, and the inner orbit's angular momentum along the z axis is conserved ($H_1 \propto j_{z,1} = \sqrt{1 - e_1^2} \cos i_{\text{tot}} = \text{Const.}$, where $j_{z,1}$ is the specific z -component of the angular momentum). Because both H_1 and F_{quad} are conserved, a new constant of motion can be defined. It is convenient (for reasons that will be identified in Section 2.3.1) to define the following constant (Katz et al. 2011):

$$C_{\text{KL}} = \frac{F_{\text{quad}}}{2} - \frac{1}{2} j_{z,1}^2 = e^2 \left(1 - \frac{5}{2} \sin^2 i_{\text{tot}} \sin^2 \omega_1^2 \right), \quad (16)$$

which is a simple function of the initial conditions. The system is integrable and has well-defined maximum and minimum eccentricities and inclinations. To find the extreme points, we set $\dot{e}_1 = 0$ in the time-evolution equation (see Equation 77, quadrupole part, in **Supplemental Text 1: The Secular Equations**) and find that the values of the argument of periapsis that satisfy this condition are $\omega_1 = 0 + n\pi/2$, where $n = 0, 1, 2, \dots$. Thus, the resonant angle has two classes of trajectories, librating and circulating. On circulating trajectories, at $\omega_1 = 0$, the eccentricity is smallest and the inclination is largest, and vice versa for $\omega_1 = \pi/2$. In **Figure 2**, librating trajectories (or libration modes) are associated with bound oscillations of ω_1 , and circulating trajectories (or circulation modes) are not constrained to a specific regime. The separatrix is the trajectory that separates the two modes of behavior, as we elaborate below.

The conservation of $j_{z,1}$ implies

$$j_{z,1} = \sqrt{1 - e_{1,\text{max/min}}^2} \cos i_{1,\text{min/max}} = \sqrt{1 - e_{1,0}^2} \cos i_{1,0}, \quad (17)$$

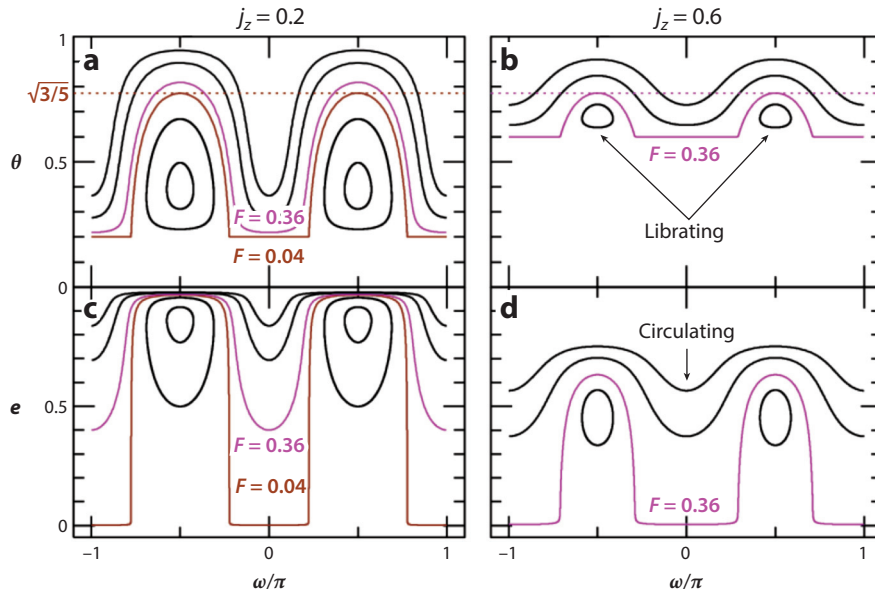


Figure 2

Cross section trajectory of the test particle quadrupole in the (a,b) $\theta - \omega_1$ and (c,d) $e_1 - \omega_1$ planes. We define $\theta = \cos i_{\text{tot}}$. The dashed horizontal lines in panels a and b show the critical inclination for which $\theta = \sqrt{3}/5$. The separatrix is associated with $e_1 = 0$ for $\omega_1 = 0$ and $\theta = \sqrt{3}/5$ for $\omega_1 = \pi/2$, as depicted in the figure. Panels a and c show the case for $j_z = 0.2$ and $F_{\text{quad}}^{\text{TP}} = -1.44$ and -0.64 (librating) and $F_{\text{quad}}^{\text{TP}} = 0.04, 0.36, 1$, and 1.44 (circulating). Panels b and d show the case for $j_z = 0.6$ and $F_{\text{quad}}^{\text{TP}} = 0.25$ (librating) and $F_{\text{quad}}^{\text{TP}} = 0.36, 0.64$ and 1 (circulating). Figure adapted from Lithwick & Naoz (2011) with permission.

where $e_{1,0}$ and $i_{1,0}$ are the initial values. Note that in this case (TPQ) $i_1 = i_{\text{tot}}$. Because the energy is also conserved, plugging in $\omega_1 = 0$ for the circulating mode, we find

$$E_0 = 2e_{1,\min}^2 - 2 + (1 - e_{1,\min}^2) \cos^2 i_{\max}^2, \quad (18)$$

and for $\omega_1 = \pm\pi/2$ in Equation 15, we find

$$E_0 = -3e_{1,\max}^2 + (1 - 4e_{1,\max}^2) \cos^2 i_{\min}^2, \quad (19)$$

where E_0 represents the initial conditions plugged into Equation 15. From Equations 17 and 18 one can easily find the minimum eccentricity and maximum inclination; likewise from Equations 17 and 19, the maximum eccentricity and the minimum inclination. A special and useful case is found by setting initially $e_{1,0} = 0$ and $\omega_{1,0} = 0$; for this case the maximum eccentricity is

$$e_{\max} = \sqrt{1 - \frac{5}{3} \cos^2 i_0}. \quad (20)$$

Solving the equations for $\cos i_{\min}$ instead, we can find

$$\cos i_{\min} = \pm \sqrt{\frac{3}{5}}, \quad (21)$$

which gives $i_{\min} = 39.2^\circ$ and $i_{\min} = 140.77^\circ$, known as Kozai angles. These angles represent the regime in which large eccentricity and inclination oscillations are expected to take place. The value $\cos i_{\min} = \pm\sqrt{3}/5$ marks the separatrix depicted in **Figure 2**.

2.2.2. Axisymmetric potential beyond the test particle approximation. In this case, we still keep the outer orbit circular; thus, the quadrupole level of approximation is still valid, but we relax the test particle approximation. The quadrupole-level Hamiltonian can be written as

$$\mathcal{H}_{\text{quad}} = C_2[(2 + 3e_1^2)(3 \cos^2 i_{\text{tot}} - 1) + 15e_1^2 \sin^2 i_{\text{tot}} \cos(2\omega_1)], \quad (22)$$

where

$$C_2 = \frac{k^4}{16} \frac{(m_1 + m_2)^7}{(m_1 + m_2 + m_3)^3} \frac{m_3^7}{(m_1 m_2)^3} \frac{L_1^4}{L_2^3 G_2^3}. \quad (23)$$

Note that in this form of Hamiltonian the nodes (Ω_1 and Ω_2) have been eliminated, allowing for a cleaner format; however, this does not mean that the z -component of the inner and outer angular momenta are constants of motion (as explained in Naoz et al. 2011, 2013a).

Relaxing the test particle approximation (i.e., none of the masses have insignificant mass) already allows for deviations from the nominal TPQ behavior. This is because now $j_{z,1}$ is no longer conserved and instead the total angular momentum is conserved. Note that the outer potential is axisymmetric and $G_2 = \text{Const}$. The system is still integrable and has well-defined maxima and minima for the eccentricity and inclination. The conservation of the total angular momentum, i.e., $\mathbf{G}_1 + \mathbf{G}_2 = \mathbf{G}_{\text{tot}}$, sets the relation between the maximum/minimum total inclinations and inner orbit eccentricities.

$$L_1^2 (1 - e_1^2) + 2L_1 L_2 \sqrt{1 - e_1^2} \sqrt{1 - e_2^2} \cos i_{\text{tot}} = G_{\text{tot}}^2 - G_2^2. \quad (24)$$

Note that in the quadrupole-level approximation G_2 , and thus e_2 , is constant. The right-hand side of the above equation is set by the initial conditions. In addition, L_1 and L_2 (see Equations 4 and 5) are also set by the initial conditions. Using conservation of energy, we can write, for the minimum eccentricity/maximum inclination case (i.e., setting $\omega_1 = 0$),

$$\frac{\mathcal{H}_{\text{quad}}}{2C_2} = 3 \cos^2 i_{\text{tot,max}} (1 - e_{1,\text{min}}^2) - 1 + 6e_{1,\text{min}}^2. \quad (25)$$

The left-hand side of this equation, and the remainder of the parameters in Equation 24, are determined by the initial conditions. Thus solving Equation 25 together with Equation 24 gives the minimum eccentricity/maximum inclination during the system evolution as a function of the initial conditions. We find a similar equation if we set $\omega_1 = \pi/2$ for the maximum eccentricity/minimum inclination:

$$\frac{\mathcal{H}_{\text{quad}}}{2C_2} = 3 \cos^2 i_{\text{tot,min}} (1 + 4e_{1,\text{max}}^2) - 1 - 9e_{1,\text{max}}^2. \quad (26)$$

Equations 24 and 26 give a simple relation between the total minimum inclination and the maximum inner eccentricity as a function of the initial conditions.

An interesting consequence of this physical picture is if the inner binary members are more massive than the third object. We adopt this example from Naoz et al. (2013a) and consider the triple system PSR B1620–26. The inner binary contains a millisecond radio pulsar of $m_1 = 1.4 M_\odot$ and a companion of $m_2 = 0.3 M_\odot$ (e.g., McKenna & Lyne 1988). We adopt parameters for the outer perturber of $m_3 = 0.01 M_\odot$ (Ford et al. 2000a) and set $e_2 = 0$ (see the caption of **Figure 3** for a full description of the initial conditions). Note that Ford et al. (2000a) found $e_2 = 0.45$, which means that the quadrupole level of approximation is insufficient to represent the behavior of the system. We choose, however, to set $e_2 = 0$ to emphasize the point that even an axisymmetric outer potential may result in a qualitatively different behavior if the TPQ approximation is assumed. For the same reason, we also adopt a higher initial value for the inner orbit eccentricity ($e_1 = 0.5$ compared to the measured one, $e_1 \sim 0.045$). The time evolution of the system is shown in **Figure 3**.

In this figure, we compare the z -component of the angular momentum H_1 with $L_1 \sqrt{1 - e_1^2} \cos i_{\text{tot}}$,

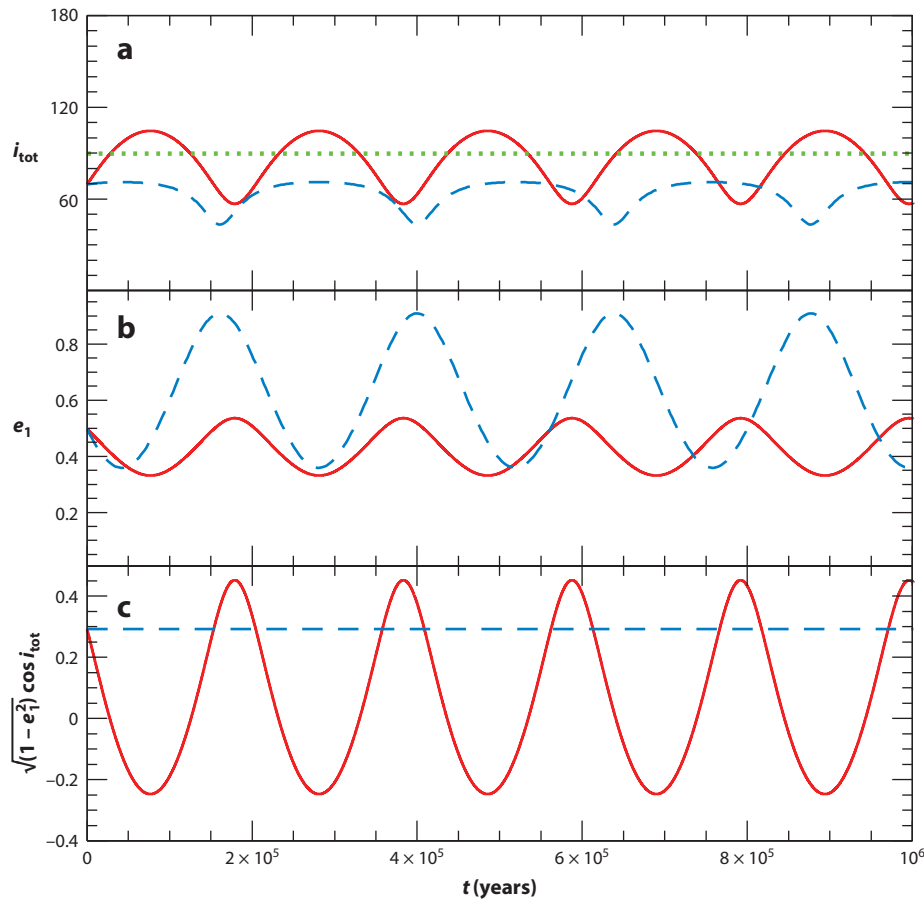


Figure 3

Comparison between the test particle quadrupole (TPQ) formalism (*dashed blue lines*) and the full quadrupole calculation (*solid red lines*). The system has an inner binary with $m_1 = 1.4 M_\odot$ and $m_2 = 0.3 M_\odot$, and the outer body has mass $m_3 = 0.01 M_\odot$. The orbit separations are $a_1 = 5$ AU and $a_2 = 50$ AU. The system was set initially with $e_1 = 0.5$ and $e_2 = 0$, $\omega_1 = 120^\circ$ and $\omega_2 = 0$, and relative inclination $i_{\text{tot}} = 70^\circ$. The panels show (a) the mutual inclination i_{tot} , (b) e_1 , and (c) $\sqrt{1 - e_1^2} \cos i_{\text{tot}}$, which in the TPQ formalism is constant (*blue dashed line*). The green dotted line in panel a represents the 90° line. Figure adapted from Naoz et al. (2013a) with permission (note that in the panel b y-axis, $1 - e_1$ is a correction over that which appeared in the original).

which is the angular momentum that would be inferred if the outer orbit were instantaneously in the invariable plane, as is found in the TPQ formalism.

Taking the outer body to be much smaller than the inner binary (i.e., $m_3 < m_1, m_2$), as done in **Figure 3**, yields yet another interesting consequence for relaxing the test particle approximation. In some cases large eccentricity excitations can take place for inclinations that largely deviate from the nominal range of the Kozai angles of 39.2° – 140.77° . The limiting mutual inclination that can result in large eccentricity excitations can be easily found when solving Equations 24 and 26, because they depend on mutual inclination, as noted by Martin & Triaud (2015b). This evolution is shown in **Figure 4**, where large eccentricity oscillation for the inner binary is achieved for an

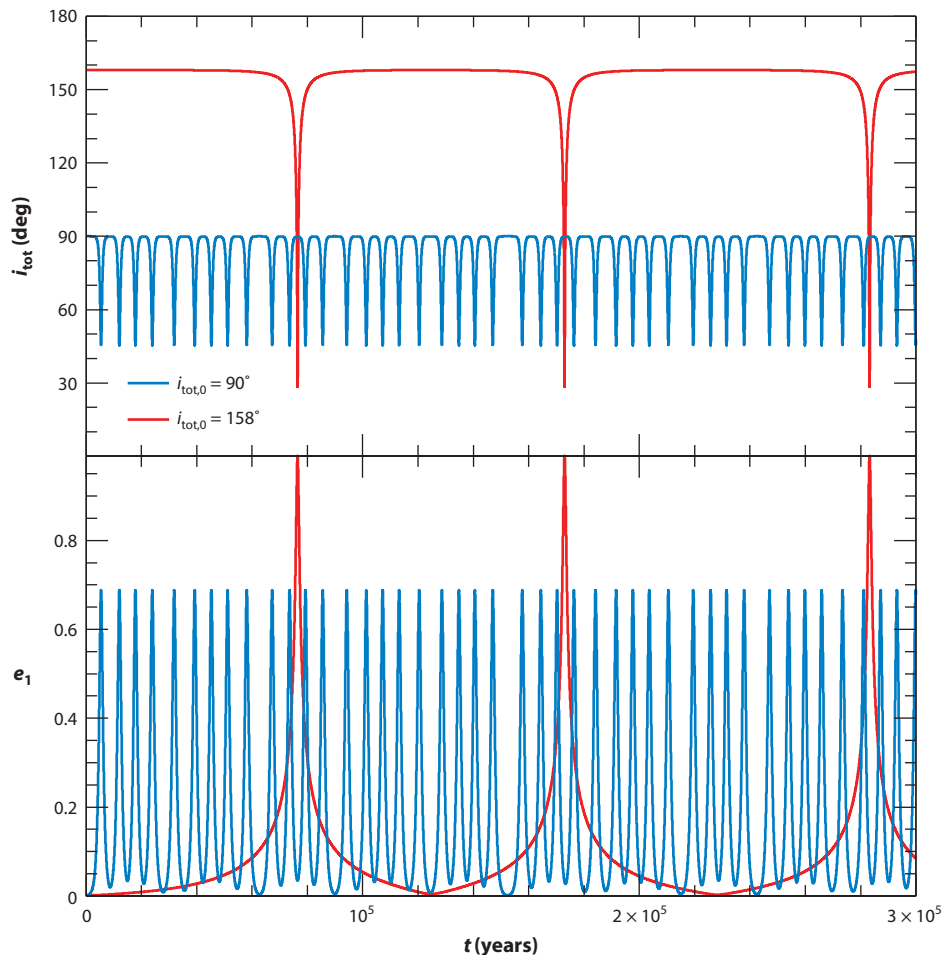


Figure 4

Small-mass outer perturber that induces large eccentricity excitation away from the nominal range of the Kozai angles of 39.2° – 140.77° . We consider $m_1 = 1 M_\odot$, $m_2 = 0.5 M_\odot$, $m_3 = 0.05 M_\odot$, $a_1 = 0.5$ AU, and $a_2 = 5$ AU. Both outer and inner eccentricities are set initially to zero, and also set initially are $\omega_1 = 90^\circ$ and $\omega_2 = 0^\circ$. We show two examples: The first shows the eccentricity excitations for as expected initial mutual inclination of $i_{\text{tot}} = 90^\circ$, where in this case $i_1 = 25.01^\circ$ and $i_2 = 64.99^\circ$. This produces eccentricity excitation with $e_{1,\text{max}} = 0.689$. We also consider an example for which the mutual inclination is set initially to be $i_{\text{tot}} = 158^\circ$. In this case $i_1 = 17.12^\circ$ and $i_2 = 140.88^\circ$. The latter parameters are adapted from Martin & Triaud (2015b), which leads to maximum inner eccentricity of $e_{1,\text{max}} = 0.99$. Note that in both examples i_2 is close to the nominal Kozai angles range.

initial mutual inclination of 158° . This behavior, as expected from the equations, is sensitive to the eccentricity of the outer orbit.

In the circular outer orbit case, the regular oscillations of the eccentricity and inclination yield a well-defined associated timescale. This can be easily achieved by considering the equation of motion of the argument of periastris ω_1 (see the part that is proportional to C_2 in Equation 73 in **Supplemental Text 1: The Secular Equations**). More precisely, $t_{\text{quad}} \sim G_1/C_2$, where C_2 is

given in Equation 23. Integrating between the well-defined maximum and minimum eccentricities, Antognini (2015) found a numerical factor 16/15, and got

$$\begin{aligned} t_{\text{quad}} &\sim \frac{16 a_2^3 (1 - e_2^2)^{3/2} \sqrt{m_1 + m_2}}{15 \frac{a_1^{3/2} m_3 k}} \\ &= \frac{16}{30\pi} \frac{m_1 + m_2 + m_3}{m_3} \frac{P_2^2}{P_1} (1 - e_2^2)^{3/2}. \end{aligned} \quad (27)$$

This timescale is in good agreement with the numerical evolution.

2.3. Eccentric Outer Orbit

Eccentric orbits are pervasive in nature. For example, the eccentricity distribution of binary stars in the field is observed to be uniform (e.g., Raghavan et al. 2010) and is estimated as thermal for young stellar clusters (e.g., Kroupa 1995). Furthermore, the eccentricity distribution of stars around the supermassive black hole in the galactic center is estimated even steeper than thermal (e.g., Gillessen et al. 2009). Thus, relaxing the circular orbit assumption will allow for wider possibility of applications.

2.3.1. Inner orbit's test particle approximation. In this approximation, we allow for an eccentric outer orbit but restrict ourselves to taking the mass of one of the inner members to zero, which yields $i_1 = i_{\text{tot}}$. In the test particle limit, the outer orbit is stationary and the system reduces to two degrees of freedom. The eccentric outer orbit yields the quadrupole level of approximation inadequate, and thus we consider the test particle octupole (TPO) level here. This approximation is extremely useful in gaining an overall understanding of the general hierarchical system and the EKL mechanism. The Hamiltonian H^{TP} of this system is very simple and can be written as (e.g., Lithwick & Naoz 2011),

$$\mathcal{H}^{\text{TP}} = \frac{3}{8} k^2 \frac{m_1 m_3}{a_2} \left(\frac{a_1}{a_2} \right)^2 \frac{1}{(1 - e_2^2)^{3/2}} (F_{\text{quad}} + \epsilon F_{\text{oct}}), \quad (28)$$

where

$$\epsilon = \frac{a_1}{a_2} \frac{e_2}{1 - e_2^2}. \quad (29)$$

F_{quad} is defined in Equation 15, and we reiterate it here for completeness,

$$F_{\text{quad}} = -\frac{e_1^2}{2} + \theta^2 + \frac{3}{2} e_1^2 \theta^2 + \frac{5}{2} e_1^2 (1 - \theta^2) \cos(2\omega_1), \quad (30)$$

and

$$\begin{aligned} F_{\text{oct}} &= \frac{5}{16} \left(e_1 + \frac{3e_1^3}{4} \right) [(1 - 11\theta - 5\theta^2 + 15\theta^3) \cos(\omega_1 - \Omega_1) + (1 + 11\theta - 5\theta^2 - 15\theta^3) \cos(\omega_1 + \Omega_1)] \\ &\quad - \frac{175}{64} e_1^3 [(1 - \theta - \theta^2 + \theta^3) \cos(3\omega_1 - \Omega_1) + (1 + \theta - \theta^2 - \theta^3) \cos(3\omega_1 + \Omega_1)]. \end{aligned} \quad (31)$$

In this case the z -component of the outer orbit is not conserved, and the system can flip from $i_{\text{tot}} < 90^\circ$ to $i_{\text{tot}} > 90^\circ$ (Naoz et al. 2011, 2013a). The flip is associated with an extremely high eccentricity transition (see, for example, **Figure 5**). The octupole level of approximation introduces higher-order resonances that overall render the system to be qualitatively different from a system at which the quadrupole level of approximation is applicable. We begin by reviewing the different effects in the systems that can be divided into two main initial inclination regimes.

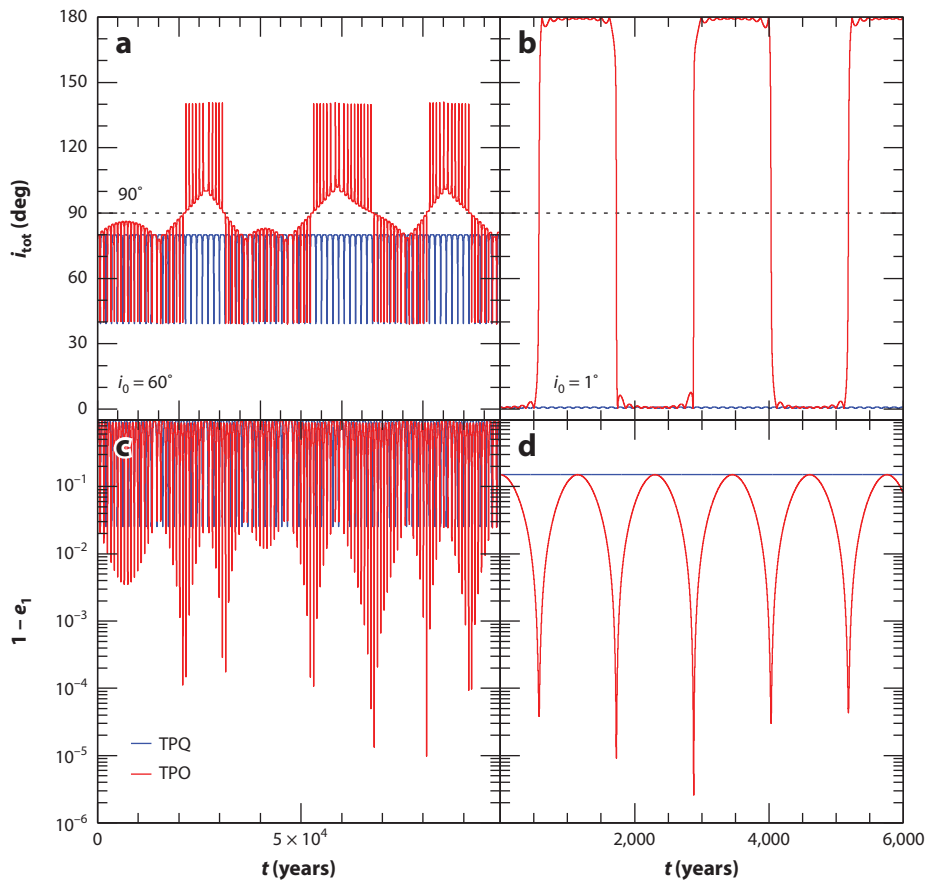


Figure 5

Time evolution example of the test particle octupole (TPO) approximation (red lines) and the test particle quadrupole (TPQ) approximation (blue lines). Panels *a* and *c* show high-inclination ($i > 39.2^\circ$) flip, whereas panels *b* and *d* show low-inclination ($i < 39.2^\circ$) flip (high inclination $i > 39.2^\circ$, low inclination $i < 39.2^\circ$). In this example, we consider the time evolution of a test particle at 135 AU around a $10^4 M_\odot$ intermediate black hole located 0.03 pc from the massive black hole in the center of our galaxy ($4 \times 10^6 M_\odot$). In panels *a* and *c* the system initially is set with $e_1 = 0.01$, $e_2 = 0.7$, $i = 60^\circ$, $\Omega_1 = 60^\circ$, and $\omega_1 = 0^\circ$. In panels *b* and *d* the system is initially set with $e_1 = 0.85$, $e_2 = 0.85$, $i = 1^\circ$, $\Omega_1 = 180^\circ$, and $\omega_1 = 0^\circ$. In panels *a* and *b*, we show the inclination, and in panels *c* and *d* the inner orbit eccentricity as $1 - e_1$.

2.3.1.1. High initial inclination regime and chaos. When the system begins in a high-inclination regime $39.2^\circ \leq i_{\text{tot}} \leq 140.7^\circ$, the resonance arising from the quadrupole level of approximation can cause large inclination and eccentricity amplitude modulations. Recall that this angle range is associated with the TPQ separatrix. The octupole level of approximation is associated with high-order resonances that result in extremely large eccentricity peaks and flips (see **Figure 5**) as well as chaotic behavior (as explained below). As can be seen from Equation 31, these resonances arise from higher-order harmonics of the octupole-level Hamiltonian: $\omega_1 \pm \Omega_1$ and $3\omega_1 \pm \Omega_1$. A useful tool to analyze this system is in the form of surface of section (see, for example, **Figure 6**). For a two-degrees-of-freedom system, the surface of section projects a four-dimensional trajectory on a two-dimensional surface. The resonant regions are associated with fixed points, and chaotic zones

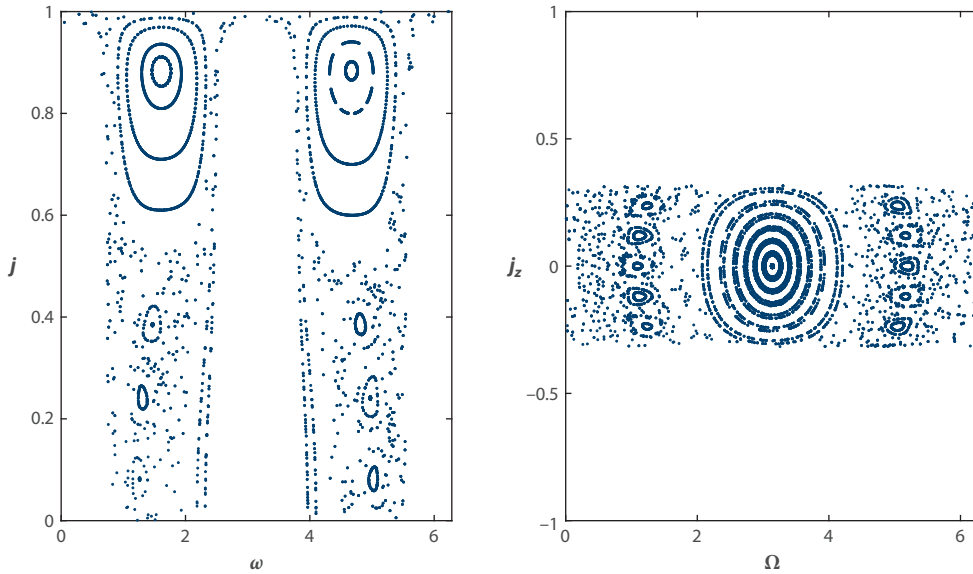


Figure 6

Surface of section for $F_{\text{quad}} + \epsilon F_{\text{oct}} = -0.1$ and $\epsilon = 0.1$. This initial configuration is associated with high initial inclination $i_{\text{tot},0} > 39.2^\circ$. The quadrupole-level resonances can clearly be seen (the big islands) as can the emergence of high-order resonances (the small islands). Adapted from Li et al. (2014a) with permission.

are a result of the overlap of the resonances between the quadrupole and the octupole resonances (Chirikov 1979, Murray & Holman 1997).

Figure 6 shows the surface of section for $\epsilon = 0.1$ and $F_{\text{quad}} + \epsilon F_{\text{oct}} = -0.1$, which is associated with high initial inclination, $i_{\text{tot},0} > 39.2^\circ$. In this figure, we can identify three distinct regions: resonant regions, circulation regions, and chaotic regions. The resonant regions are associated with trajectories of which the momenta (j and j_z) and the angles (ω_1 and Ω_1) undergo bound oscillations. The system is classified in a libration mode, and the trajectories are quasi-periodic. The libration zones in the TPQ approximation are shown in **Figure 2**, and for the TPO in **Figure 6**. The circulation regions describe trajectories for which the coordinates are not constrained to a specific interval and can take any value. Note that both resonant and circulatory trajectories map onto a one-dimensional manifold on the surface of section. On the contrary, chaotic trajectories map onto a two-dimensional manifold. In other words, though quasi-periodic trajectories form lines on the surface of section, chaotic trajectories are area-filling regimes. Embedded in the chaotic region, the small islands correspond to the higher, octupole order resonances, which are also quasi-periodic. The flip from $i_{\text{tot}} < 90^\circ$ to $i_{\text{tot}} > 90^\circ$ covers large parts of the parameter space as can be seen in **Figure 7c**.

In some cases an analytical condition for the flip can be achieved by averaging over a quadrupole cycle (Katz et al. 2011). This averaging process yields a constant of motion

$$\chi = f(C_{\text{KL}}) + \epsilon \frac{\cos i_{\text{tot}} \sin \Omega_1 \sin \omega_1 - \cos \omega_1 \cos \Omega_1}{\sqrt{1 - \sin^2 i_{\text{tot}} \sin^2 \omega_1}} = \text{Const.}, \quad (32)$$

where the function $f(C_{\text{KL}})$ is defined by

$$f(C_{\text{KL}}) = \frac{32\sqrt{3}}{\pi} \int_{x_{\text{min}}}^1 \frac{K(x) - 2E(x)}{(41x - 21)\sqrt{2x + 3}} dx \quad \text{and} \quad x_{\text{min}} = \frac{3 - 3C_{\text{KL}}}{3 + 2C_{\text{KL}}}, \quad (33)$$

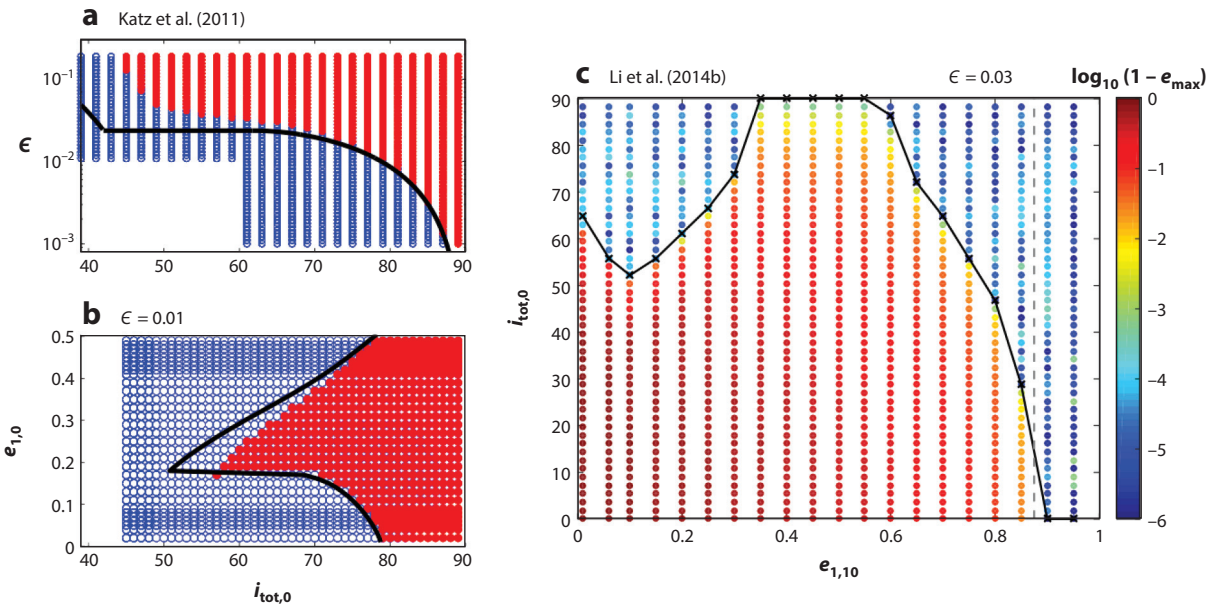


Figure 7

High-inclination flip parameter space. (*a,b*) The comparison with the analytical conditions derived by Katz et al. (2011). Open circles are the result of a numerical integration (*red* indicates systems that flipped and *blue* is for those that did not). Here the solid lines represent the flip conditions that for $e_{1,0} \sim 0$ and $i_{\text{tot},0} \gtrsim 61.7^\circ$ are reduced to Equation 33. Panel *b* shows the case of $\epsilon = 0.01$, and note that it shows only part of the parameter space. (*c*) The results of numerical integrated systems associated maximum eccentricity (color coded as $1 - e_1$) in the $i_{\text{tot},0} - e_{1,0}$ parameter space for $\epsilon = 0.03$, after $30t_{\text{quad}}$. Systems above the black line are flipped. Panels *a* and *b* are adapted from Katz et al. (2011) and panel *c* from Li et al. (2014b) with permission.

where $K(x)$ and $E(x)$ are the complete elliptic functions of the first and second kind, respectively. For high initial inclination a flipping critical value for the octupole prefactor ϵ_c is a function of the initial inclination and the approximations take a simple form:

$$\epsilon_c = \frac{1}{2} \max |\Delta f(y)|, \quad (34)$$

where $\Delta f(y) = f(y) - f(C_{\text{KL},0})$, C_{KL} was defined in Equation 16, and the subscript “0” marks the initial conditions. We note that C_{KL} in this TPO case is no longer constant (unlike the TPQ case). The parameter y has the range $C_{\text{KL},0} < y < C_{\text{KL},0} + (1 - e_{1,0}^2) \cos i_{\text{tot},0}/2$. For cases where $e_{1,0} \ll 1$, i.e., $C_{\text{KL}} \ll 1$ and $i_{\text{tot},0} \gtrsim 61.7^\circ$, Equation 34 takes a simple form:

$$\epsilon_c = \frac{1}{2} f \left(\frac{1}{2} \cos^2 i_{\text{tot},0} \right). \quad (35)$$

This approximation is valid for $\epsilon \lesssim 0.025$. The validity of this approximation for different initial values of e_1 and i_{tot} is shown in **Figure 7a,b**.

A timescale for the high-inclination oscillation or flip is difficult to quantify because the evolution is chaotic. Furthermore, numerically it seems that the timescale for the first flip depends on the inclination (as can be seen in **Figure 8**). However, an approximate analytical condition, for the regular (nonchaotic) mode was achieved recently by Antognini (2015), following the Katz

et al. (2011) formalism. This timescale has the following functional form:

$$t_{\text{flip}} = \frac{256\sqrt{10}}{15\pi\epsilon} \int_{C_{\text{KL},\text{min}}}^{C_{\text{KL},\text{max}}} \frac{dC_{\text{KL}} K(x)}{\sqrt{2(4\phi_{\text{quad}}/3 + 1/6 + C_{\text{KL}})(4 - 11C_{\text{KL}})\sqrt{6 + 4C_{\text{KL}}}}} \times \left\{ 1 - \frac{[\chi - f(C_{\text{KL}})]^2}{\epsilon^2} \right\}^{-1/2}, \quad (36)$$

where

$$\phi_{\text{quad}} = \frac{1}{8} (3F_{\text{quad}} - 1), \quad (37)$$

and note that ϕ_q defined by Antognini (2015) is simply $\phi_q = C_{\text{KL}} + j_{z,1}^2/2 = 4\phi_{\text{quad}}/3 - j_{z,1}^2/2 + 1/6$ in the notation used here. The upper limit of the integral in Equation 36 is easy to find, because for $i_{\text{tot}} \rightarrow 90^\circ$ the z -component of the angular momentum is zero; thus,

$$C_{\text{KL},\text{max}} = \frac{4}{3}\phi_{\text{quad}} + \frac{1}{6}, \quad (38)$$

and the minimum limit of the integral is found from solving $f(C_{\text{KL},\text{min}}) = \chi \pm \epsilon$. This timescale takes a simple form, for setting initially $e_1 \rightarrow 0$, $\omega_1 \rightarrow 0$, and $i_{\text{tot}} \rightarrow 90^\circ$:

$$t_{\text{flip}} \sim \frac{128}{15\pi} \frac{a_2^3}{a_1^{3/2}} \frac{\sqrt{m_1}}{km_3} \sqrt{\frac{10}{\epsilon}} (1 - e_2)^{3/2} \quad \text{for } e_{1,0} \sim 0 \quad \text{and } i_{\text{tot}} \sim 90^\circ. \quad (39)$$

In the TPO level of approximation the short (quadrupole) timescales differ from the associated timescale at the TPQ level. In other words following the evolution of the same system, once by using the TPO and once using the TPQ, yields different timescales, as depicted in the inset of **Figure 8**. This is because the Hamiltonian (i.e., the energy) is slightly different as the TPO includes the octupole term. Thus, the two calculations sample somewhat different values of the system energy. The difference is within a factor of a few as it represents the range of the phase space away from the separatrix (see **Figure 2** for the different oscillations' amplitudes for the given initial different energies).

2.3.1.2. Low initial inclination regime. The octupole level of approximation yields an interesting behavior even beyond the Kozai angles. This is a result of the octupole-level harmonics, i.e., $\omega \pm \Omega$ and $3\omega \pm \Omega$. Because the low-order resonances are missing, the coplaner flip is not associated with chaotic behavior. **Figure 9** shows the surface of section for two low-inclination examples, specifically $F_{\text{quad}} + \epsilon F_{\text{oct}} = -2$ and $F_{\text{quad}} + \epsilon F_{\text{oct}} = -1$ for $\epsilon = 0.1$.

As can be seen from **Figure 5** (as well as **Figures 6** and **9**) the two inclination regimes exhibit qualitative differences. The high-inclination flip is driven by the quadrupole-level resonance, and the actual flip arises by accumulating effects from the high-order resonances. Furthermore, this flip, most times, is associated with a chaotic behavior (Lithwick & Naoz 2011, Li et al. 2014a). However, the low-inclination flip is due to a regular trajectory. In addition, this flip takes place on a much shorter timescale than the high-inclination flip.

Similar to the analytical approximation for the high-inclination flip conditions, Li et al. (2014b) achieved an analytical condition for the low-inclination flip after averaging over the flip timescale

$$\epsilon_c > \frac{8}{5} \frac{1 - e_1^2}{7 - e_1(4 + 3e_1^2) \cos(\omega_1 + \Omega_1)}. \quad (40)$$

Comparing this condition with the high-inclination condition of Equation 34 also emphasizes the qualitative difference between these two regimes.

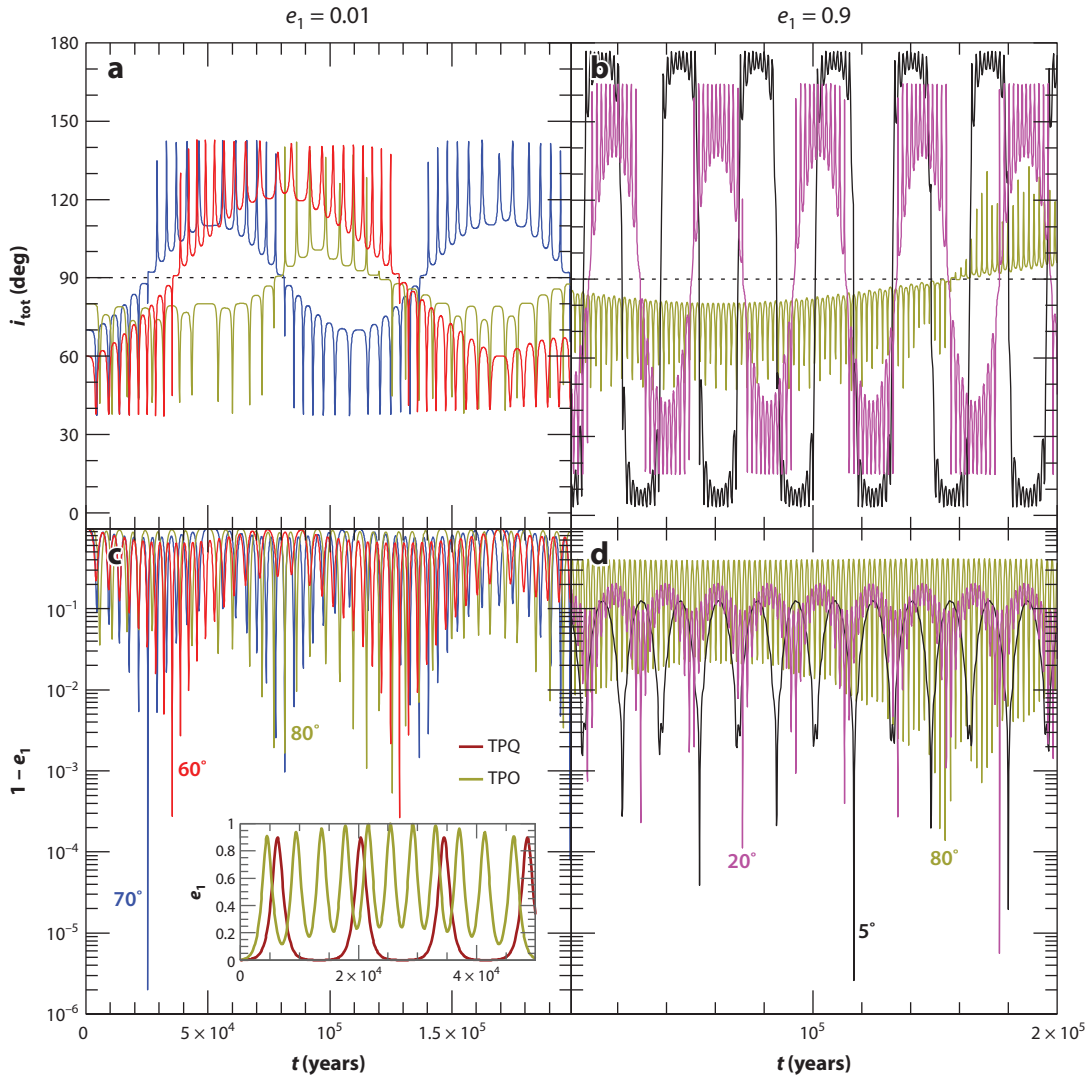


Figure 8

Flip timescales. We consider the following supermassive black hole binary system $m_1 = 10^7 M_\odot$ with $m_3 = 10^9 M_\odot$ (note that in this case $m_2 \rightarrow 0$). The other parameters of this system include the following: $a_1 = 0.05$ pc, $a_2 = 1$ pc, and $e_2 = 0.7$. The system is set initially with $\omega_1 = 51^\circ$, $\Omega_1 = 165.58^\circ$, and $e_1 = 0.01$ for panels *a* and *c* and $e_1 = 0.9$ for panels *b* and *d*. The initial inclinations considered are colored in the figure. Note the difference in flip timescale as a function of initial inclinations. In the inset in panel *c*, we show the inner orbit eccentricity e_1 as a function of time for the test particle quadrupole (TPQ; *maroon line*) and the test particle octupole (TPO; *chartreuse line*) for the initial setting of $e_1 = 0.01$ and $i_{\text{tot}} = 80^\circ$ case, which emphasizes the different short (quadrupole) timescales between the TPQ and TPO levels of approximation.

The low-inclination regime yields a flip timescale that can be easily found by setting $i_{\text{tot}} \rightarrow 0$. Li et al. (2014b) found an expression for the flip timescale:

$$t_{\text{flip}} = \left(\int_{e_{1,0}}^{e_{\text{min}}} + \int_{e_{\text{min}}}^{e_{\text{max}}} \right) \frac{-8}{5(4 + 3e_1^2)} \left\{ \epsilon (1 - e_1^2) \left[1 - \frac{(F_{\text{quad}}^0 + \epsilon F_{\text{oct}}^0 - 8e_1^2)^2}{25e_1^2(4 + 3e_1^2)^2 \epsilon^2} \right]^{-1/2} \right\}, \quad (41)$$

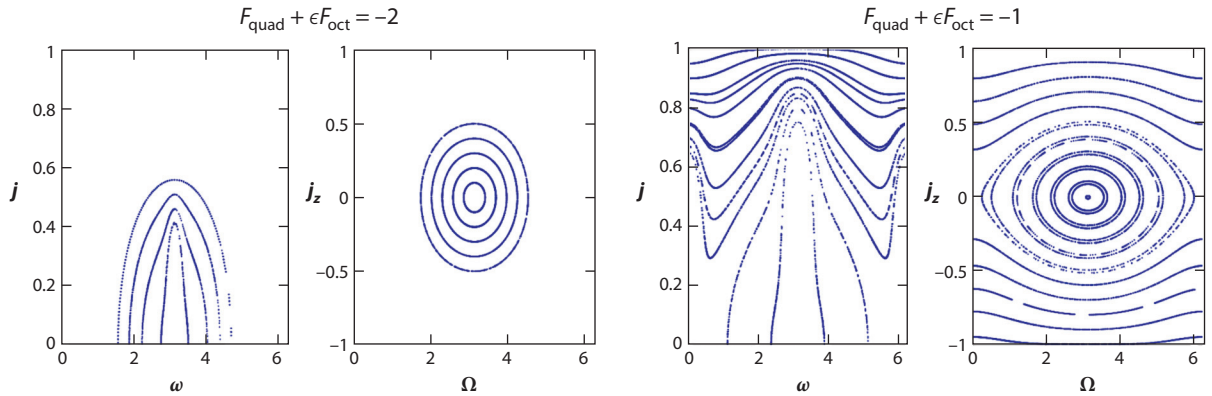


Figure 9

Surface of section for $F_{\text{quad}} + \epsilon F_{\text{oct}} = -2$ and $F_{\text{quad}} + \epsilon F_{\text{oct}} = -1$ for $\epsilon = 0.1$; this is associated with low initial inclination $i_{\text{tot},0} < 39.2^\circ$. Adapted from Li et al. (2014a) with permission. See similar plots by Petrovich (2015b), reproducing this analysis.

where $e_{1,0}$ is the initial inner orbit eccentricity and $F_{\text{quad}}^0 + \epsilon F_{\text{oct}}^0$ is the energy that corresponds to $i_{\text{tot}} = 0$ and the rest of the initial conditions (see **Figure 10**). The reason for the two integrals is because if initially $\sin(\omega_1 + \Omega_1) > 1$, then the inner orbit eccentricity, e_1 , decreases before it increases; otherwise if $\sin(\omega_1 + \Omega_1) < 1$, then $e_{\text{min}} = e_{1,0}$.

2.3.2. Beyond the test particle approximation. Relaxing the test particle approximation leads to some qualitative differences. The first is that now one of the inner bodies can torque the outer body and thus suppress the flip. This also causes a shift in the parameter space of the flip condition and the extreme eccentricity achieved compared to the TPQ case (see **Figure 11**). Although the value of the maximum of e_1 is similar to that in the TPQ case, large eccentricity excitations may take place in different parts of the parameter space (compare **Figure 11** with **Figure 7**). In particular, in the high-inclination regime, the flips and the large eccentricity excitations of the TPQ case are concentrated around $i_{\text{tot}} = 90^\circ$, but in the full case they can shift to lower mutual inclinations and tap into a larger range of inclinations (**Figure 11**). This is mainly because the outer orbit is being torqued by the inner orbit. Teysandier et al. (2013) studied the effect of a companion with similar mass and showed that if the outer body mass is reduced to below twice the smallest mass of the inner orbit, the flip and large eccentricity excitations are suppressed for large parts of the parameter space.

The system's Hamiltonian is (here again, the nodes were eliminated for simplicity, but the z -component of the angular momenta are not conserved)

$$\mathcal{H} = \mathcal{H}_{\text{quad}} + \mathcal{H}_{\text{oct}}, \quad (42)$$

where $\mathcal{H}_{\text{quad}}$ is defined in Equation 22, and we copy it here for completeness:

$$\mathcal{H}_{\text{quad}} = C_2 [(2 + 3e_1^2) (3 \cos^2 i_{\text{tot}} - 1) + 15e_1^2 \sin^2 i_{\text{tot}} \cos(2\omega_1)]; \quad (43)$$

the octupole-level approximation is

$$\mathcal{H}_{\text{oct}} = C_3 e_1 e_2 [A \cos \phi + 10 \cos i_{\text{tot}} \sin^2 i_{\text{tot}} (1 - e_1^2) \sin \omega_1 \sin \omega_2],$$

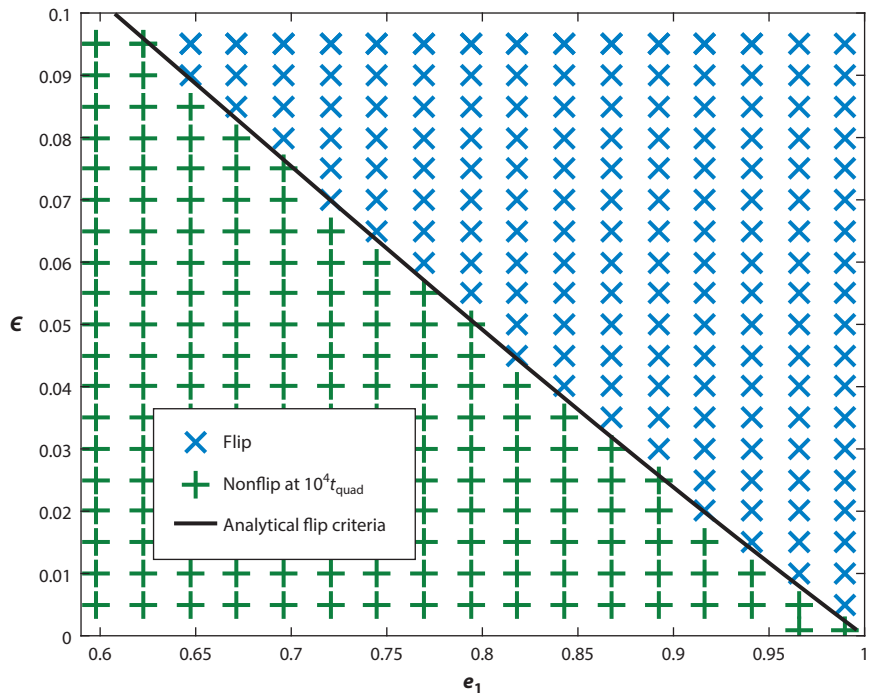


Figure 10

Low-inclination flip criterion. Comparison between the analytical expression Equation 41 (*solid line*) and numerical integration (*green crosses* mark no flip after $10^4 t_{\text{quad}}$, and *blue crosses* systems that flipped). The system's parameters are: $m_1 = 1 M_{\odot}$, $m_2 \rightarrow 0$, $m_3 = 0.1 M_{\odot}$, $a_1 = 1 \text{ AU}$, and $a_2 = 45.7 \text{ AU}$. The outer orbit eccentricity e_2 was changed to match the ϵ values indicated on the vertical axis. The system was initially set with $i_{\text{tot}} = 5^\circ$, $\omega_1 = 0^\circ$, $\Omega_1 = 180^\circ$ and e_1 as indicated in the figure. Figure adapted from Li et al. (2014b).

where

$$C_3 = -\frac{15}{16} \frac{k^4}{4} \frac{(m_1 + m_2)^9}{(m_1 + m_2 + m_3)^4} \frac{m_3^9 (m_1 - m_2)}{(m_1 m_2)^5} \frac{L_1^6}{L_2^3 G_2^5} \\ = -C_2 \frac{15}{4} \frac{\epsilon_M}{e_2}, \quad (44)$$

$$\epsilon_M = \frac{m_1 - m_2}{m_1 + m_2} \frac{a_1}{a_2} \frac{e_2}{1 - e_2^2}, \quad (45)$$

and

$$A = 4 + 3e_1^2 - \frac{5}{2} B \sin^2 i_{\text{tot}}, \quad (46)$$

where

$$B = 2 + 5e_1^2 - 7e_1^2 \cos(2\omega_1), \quad (47)$$

and

$$\cos \phi = -\cos \omega_1 \cos \omega_2 - \cos i_{\text{tot}} \sin \omega_1 \sin \omega_2. \quad (48)$$

The latter equation emphasizes one of the main differences that arises from relaxing the test particle approximation. In cases for which $m_1 \sim m_2$ the contribution from the octupole level of

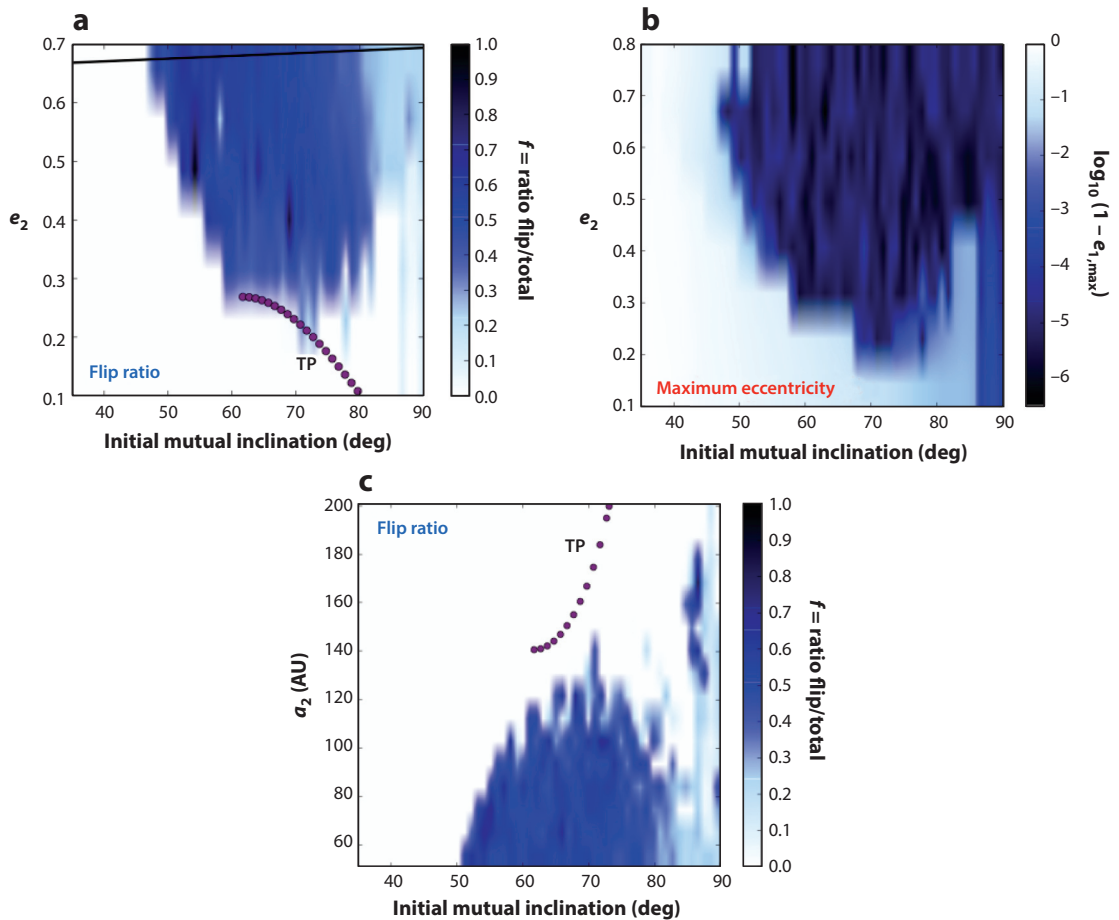


Figure 11

Flip and maximum eccentricity parameter space in a two-hierarchical-planets configuration. The color describes (b) the maximum eccentricity reached over an integration time of $\sim 5,000t_{\text{quad}}$ and (a,c) the flip ratio, defined as the time the total inclination spends over 90° from the entire integration time. Panel b shows the phase space corresponding to e_{max} and panel a shows the flip ratio as a function of the initial outer orbit eccentricity (e_2) and the initial mutual inclination. Note that both exhibit interesting behavior at similar parts in the parameter space. However, for initial high inclination of 80° – 90° , the flip is suppressed. The system considered here has the following parameters: $m_1 = 1 M_\odot$, $m_2 = 1 M_J$, $m_3 = 6 M_J$, $a_1 = 5$ AU, and $a_2 = 61$ AU. Panel c shows the flip ratio in the initial a_2 – i_{tot} phase space. The system considered in this panel has the same parameters as panels a and b, but with $e_2 = 0.5$ and varying a_2 . The flip condition for the test particle quadrupole (TPQ), following the condition in Equation 35, is shown in purple dots. The TPQ analysis for panel a (c) suggests that all systems above (below) the “TP” dotted line are expected to flip. The solid black line represents the stability condition; see Equation 51. Adapted from Teyssandier et al. (2013) with permission.

approximation can be negligible. This can be seen in the example in **Figure 12** for a system in which the only difference between the left and right panels is setting $m_2 = 0$ in the left panels and $m_2 = 8 M_\odot$ in the right panels ($m_1 = 10 M_\odot$). In the pure Newtonian regime, the EKL behavior is suppressed (no flips or eccentricity peaks). The complete set of the equations of motion can be found in **Supplemental Text 1: The Secular Equations**.

 **Supplemental Material**

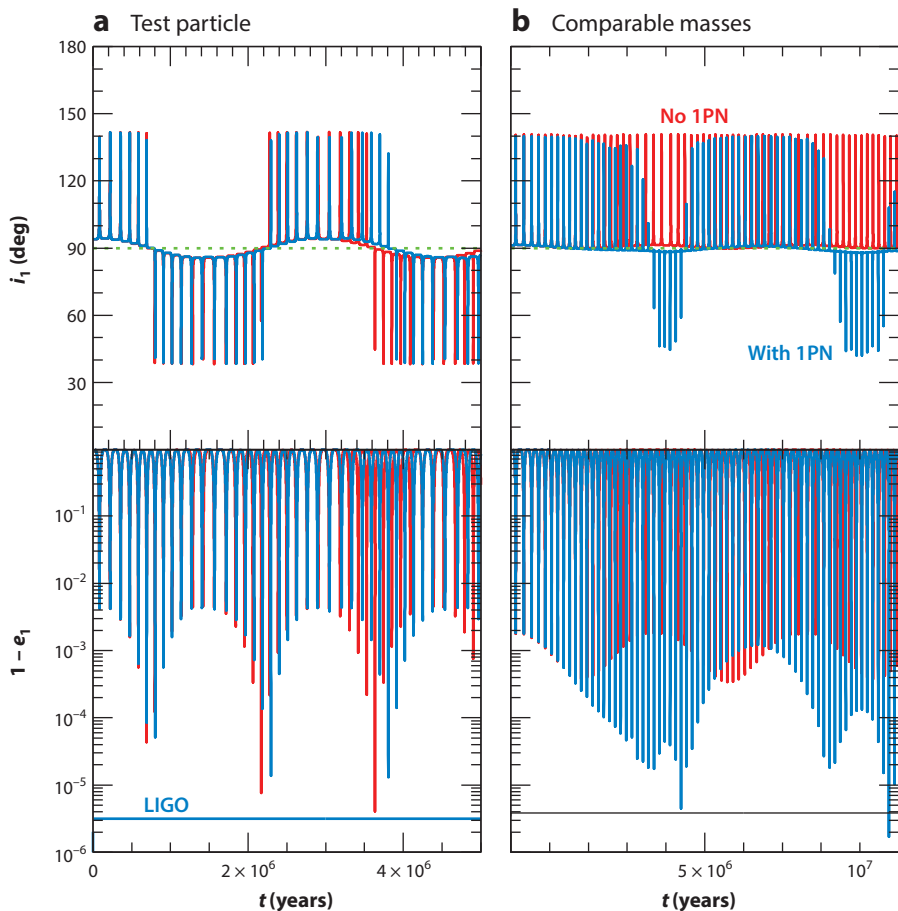


Figure 12

Comparison between the test particle approximation and a comparable-mass system in the presence of general relativity. The systems in the right and left panels have the same parameters and initial conditions apart from m_2 , which is set to zero in panel *a* and $m_2 = 8 M_\odot$ in panel *b*. The other parameters are: $m_1 = 10 M_\odot$, $m_3 = 30 M_\odot$, $a_1 = 10 \text{ AU}$, $a_2 = 502 \text{ AU}$, $e_1 = 0.001$, $e_2 = 0.7$, $\omega_1 = \omega_2 = 240^\circ$, and $i_{\text{tot}} = 94^\circ$. Red lines correspond to pure Newtonian evolution, and blue lines include general relativity (GR) effects [first post-Newtonian expansion (1PN), to the inner and outer orbits]. The horizontal lines are the minimum eccentricity corresponding to the detectable LIGO frequency range (*horizontal lines in the bottom panels*). GR corrections help to further increase the eccentricity and lead to orbital flips for the inner binary for comparable masses. Adapted from Naoz et al. (2013b) with permission.

3. THE VALIDITY OF THE APPROXIMATION AND THE STABILITY OF THE SYSTEM

The secular approximation described here utilizes averaging over the short orbital timescales, and thus any modulations over these times are washed out. Katz & Dong (2012), Antognini et al. (2014), Antonini et al. (2014), and Bode & Wegg (2014) showed that the inner orbit undergoes rapid eccentricity oscillations near the secular value on the timescale of the outer orbital period (see, for example, **Figure 13**). Ivanov et al. (2005) found the change in angular momentum (for

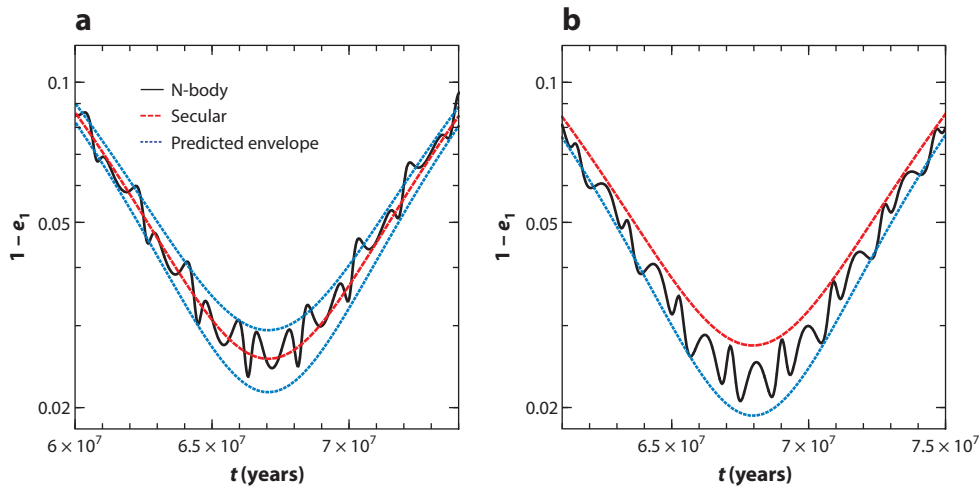


Figure 13

Comparison of the eccentricity excitations. The figure considers the results from the secular approximation (red lines) and N-body (black lines) and the predicted change from Equation 49. The system considered has the following parameters: $m_1 = 10^7 M_\odot$, $m_2 = 10^5 M_\odot$, $m_3 = 10^7 M_\odot$, $a_1 = 1$ pc, $a_2 = 20$ pc, $e_1 = 0.1$, $e_2 = 0.2$, and $i_{\text{tot}} = 80^\circ$. Panel *a* was initialized with $\omega_1 = \omega_2 = 0^\circ$ and panel *b* was initialized with $\omega_1 - \omega_2 = 90^\circ$. Adapted from Antognini et al. (2014) with permission.

$m_1 \gg m_3, m_2$) during an oscillation is

$$\frac{\Delta G_1}{\mu_1} = \frac{15}{4} \frac{m_3}{m_1 + m_2} \cos i_{\min} \left(\frac{a_1}{a_2} \right)^2 k \sqrt{m_1 a_2}, \quad (49)$$

where μ_1 is the reduced mass of the inner binary, and i_{\min} is the minimum inclination reached during the oscillation. These rapid eccentricity oscillations happen because the value of the inner orbit angular momentum goes to zero (i.e., extreme inner orbit eccentricity) on shorter timescales than the outer orbital period. Furthermore, the arguments of periapsis of the inner and outer orbits determine the direction of the oscillation. In that case the averaging is not sufficient, and the secular approximation underestimates the maximum eccentricity that the system can reach.

Another condition takes place when there is a significant change in the angular momentum during one inner orbital period. Assuming a fixed outer perturber and adopting an instantaneous quadrupole torque, Antonini et al. (2014) took the limit of $e_1 \rightarrow 1$ and found a simple form for the condition for which the averaging is valid:

$$\sqrt{1 - e_1} \gtrsim 5\pi \frac{m_3}{m_1 + m_2} \left[\frac{a_1}{a_2(1 - e_2)} \right]^3 \quad (50)$$

[using slightly different settings, Katz & Dong (2012) and Bode & Wegg (2014) found a similar condition]. Thus, if during the evolution the specific angular momentum becomes smaller than the right-hand side of Equation 50, the angular momentum goes to zero on shorter timescales than the inner orbital timescale. The immediate consequence of this is that the inner binary maximum eccentricity will be larger than the value the secular approximation predicts.

Recently, Luo et al. (2016) showed that these rapid, short-timescale oscillations can accumulate over long timescales and lead to deviations from the flip conditions discussed in Section 2.3.1, as described in Equation 34. They found that the double-averaging procedure fails when the mass of the tertiary m_3 is large compared to the mass of the inner binary.

Another consequence of large eccentricities is the stability of the system. A long-term stability condition that is often used in the literature is the one given by [Mardling & Aarseth \(2001\)](#), which has the following form:

$$\frac{a_2}{a_1} > 2.8 \left(1 + \frac{m_3}{m_1 + m_2}\right)^{2/5} \frac{(1 + e_2)^{2/5}}{(1 - e_2)^{6/5}} \left(1 - \frac{0.3i_{\text{tot}}}{180^\circ}\right). \quad (51)$$

Although this criterion was generated for similar-mass binaries and the inclination was added ad hoc, it is often used for a large range of masses. A criterion takes into account both having the outer orbit be wider than the inner one and the validity of secular approximation:

$$\epsilon = \frac{a_1}{a_2} \frac{e_2}{1 - e_2^2} < 0.1. \quad (52)$$

This is numerically similar to the [Mardling & Aarseth \(2001\)](#) stability criterion (Equation 51) for systems over a large range of masses (as shown in [Naoz et al. 2013b](#)).

The stability of a two-planet system with low mutual inclination was studied by [Petrovich \(2015c\)](#), using N -body integration. Assuming that m_1 is a stellar-mass object and m_2 and m_3 are planetary-mass objects, he found a stability criterion of the following form:

$$\frac{a_2(1 - e_2)}{a_1(1 + e_1)} > 2.4 \left[\max\left(\frac{m_2}{m_1}, \frac{m_3}{m_1}\right) \right]^{1/3} \sqrt{\frac{a_2}{a_1}} + 1.15. \quad (53)$$

Systems that do not satisfy this condition (by a margin factor of ~ 0.5) may become unstable. Specifically, [Petrovich \(2015c\)](#) found that systems for which $m_2/m_1 > m_3/m_1$ will most likely result in planetary ejections, whereas systems for which $m_2/m_1 < m_3/m_1$ may slightly favor collisions with the host star.

The eccentricity excitations, both in the secular approximation and in its deviations, are extremely large (see [Figures 7](#) and [11](#)). This implies that in some cases the inner orbit can reach such a small pericenter distance R_{Lobe} such that one of the objects may cross its Roche limit (e.g., in the case where $m_2 < m_1$):

$$R_{\text{Lobe}} = \eta R_2 \left(\frac{m_2}{m_1 + m_2}\right)^{-1/3}, \quad (54)$$

where η is a numerical factor of order unity.

Considering the definition of the Roche limit, we can also ask when the eccentricity of the inner orbit becomes so large such that the tertiary captures a test particle that is orbiting around the primary ($m_1, m_3 \gg m_2$), which can be written as

$$a_1(1 + e_1) = \tilde{\eta} a_2(1 - e_2) \left(\frac{m_1}{m_3}\right)^{1/3}, \quad (55)$$

where $\tilde{\eta}$ is of order unity and is of different value from η in Equation 54. A test particle initially around m_1 with larger separations feels a larger gravitational force from m_3 . Using the definition of ϵ , [Naoz & Silk \(2014\)](#) found the mass ratio that will result in a stable configuration as a function of the binary-mass ratio, i.e.,

$$\frac{m_3}{m_1} = \left[\tilde{\eta} \frac{e_2}{\epsilon(1 + e_1)(1 + e_2)} \right]^3. \quad (56)$$

Thus for mass ratios that are larger than the right-hand side of Equation 56, the approximation breaks down and the test particle may be captured by m_3 (some consequences are discussed in [Li et al. 2015](#)).

4. SHORT-RANGE FORCES AND OTHER ASTROPHYSICAL EFFECTS

The Newtonian evolution of the secular hierarchical three-body system has proven to be very useful in modeling and analyzing many astrophysical systems. In realistic systems there are several short-range forces and astrophysical effects that can significantly alter the evolution of the system. For example, some short-range forces, such as tides and GR, induce precession of the periape, which strongly depends on the orbital eccentricity. If the orbit precesses, owing to the short-range force, to the opposite direction than that induced by the Kozai-Lidov mechanism, then further excitations of the eccentricity can be suppressed. In the limiting case, the precession is so fast compared to quadrupole-level precession that the inner orbit initial eccentricity remains constant. In fact, as is discussed below, in some cases the eccentricity excitation in the presence of short-range force can be estimated analytically. Because in the Kozai-Lidov mechanism eccentricity is being traded for inclination, once the eccentricity cannot be excited, the oscillations in the inclination are limited in a similar way.

4.1. General Relativity

The fast precession of the perihelion of the inner orbit due to GR effects takes place on the opposite direction of the quadrupole precession. Therefore, as mentioned before, the inner orbit extremely high eccentricity excitations are suppressed, and thus so are the inclination flips as well. For example, in the current location of most hot Jupiters, further eccentricity excitations are suppressed owing to fast GR precession (and tides) in comparison with the quadrupole precession. Thus, hot Jupiters have decoupled from their potential perturbers and do not flip anymore. However, the t_{quad} timescale is much shorter compared to the GR precession in asteroid and Kuiper belt binaries.

The precession of the inner orbit due to GR has a simple form:

$$\left. \frac{d\omega_1}{dt} \right|_{\text{1PN,inner}} = \frac{3k^3(m_1 + m_2)^{3/2}}{a_1^{5/2}c^2(1 - e_1^2)}, \quad (57)$$

where the subscript 1PN,inner indicates that precession is due to first post-Newtonian (PN) expansion for the inner orbit [see Misner et al. (1973) for a general derivation]. A similar expression can be written for outer orbit GR precession, although this, typically, has little effect. Expanding the first PN three-body Hamiltonian in semimajor axes ratio up to the octupole level of approximation reveals another term that describes the GR interaction between the inner and outer orbits (Naoz et al. 2013b). In many cases in which the leading Newtonian terms are important, this interaction term can be neglected. The inner orbit GR precession timescale can be estimated simply as (Naoz et al. 2013b)

$$t_{\text{1PN,inner}} \sim 2\pi \frac{a_1^{5/2}c^2(1 - e_1^2)}{3k^3(m_1 + m_2)^{3/2}}. \quad (58)$$

If this timescale is shorter than the quadrupole timescale (Equation 27), eccentricity excitations are suppressed (this has been noted in many studies, e.g., Ford et al. 2000b, Fabrycky & Tremaine 2007, Naoz et al. 2013b). For example, **Figure 14** depicts the relevant timescales for a Jupiter-mass planet around a $1-M_{\odot}$ star. Different perturbers induce quadrupole precessions, which are compared with the GR precession (Equation 58). For example, a planetary companion at 30 AU cannot excite the eccentricity of a Jupiter-mass planet that formed at 0.5 AU (a closer companion can); however, a companion can excite the eccentricity of a 1-AU Jupiter-mass planet, which may result in the formation of a hot Jupiter (see below).

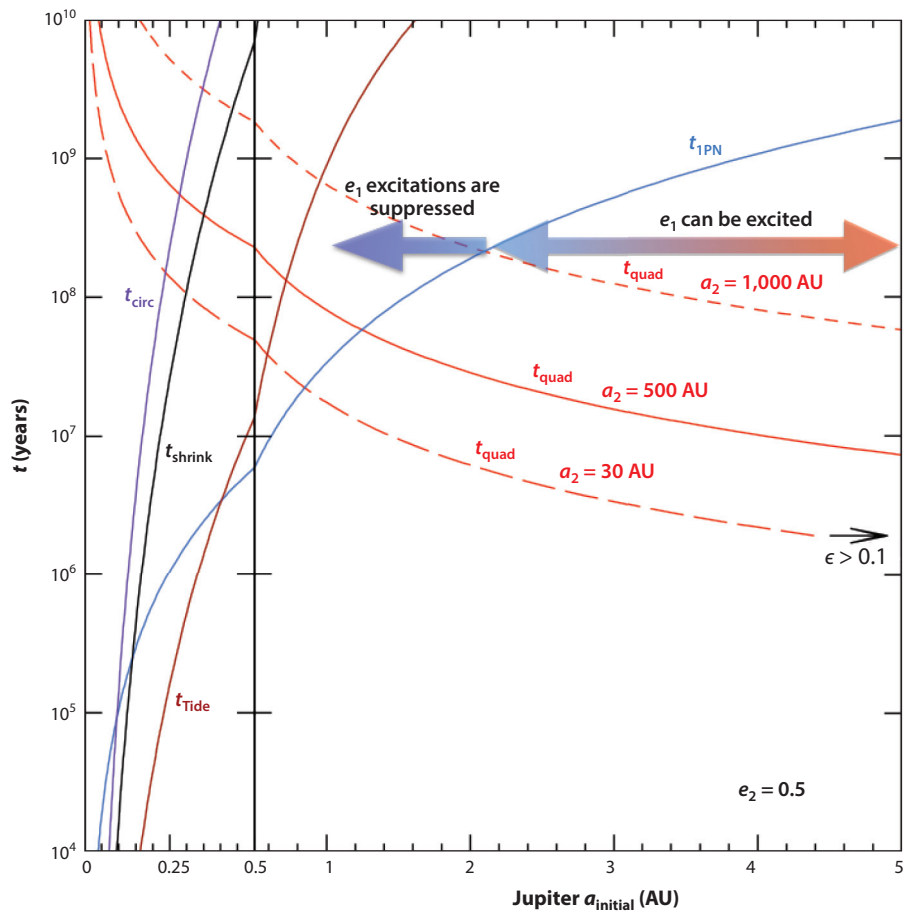


Figure 14

Relevant timescales for a Jupiter system. The system considered here is a Jupiter-mass planet at different initial separations a_{initial} from a $1-M_{\odot}$ star. We consider the quadrupole timescale (Equation 27) for a stellar perturber ($m_3 = 1 M_{\odot}$) at $a_2 = 1,000$ AU and $a_2 = 500$ AU (*short-dashed* and *solid red lines*, respectively), as well as the case of a Jupiter perturber at 30 AU (*long-dashed red line*). $e_2 = 0.5$ in all these cases. We also consider the precession of the inner orbit due to GR, according to Equation 58 (*blue line*). The crossing point between the blue and red lines roughly separates between the different behaviors, as depicted by the arrows. We also consider the precession due to oblate objects from static tides (Equation 61; *brown line*) and the typical timescales to circularize and shrink the orbit (*purple* and *black lines*, respectively) according to the equations in **Supplemental Text 2: Static Tides Equations** while adopting $T_{V,1} = 50$ years and $T_{V,2} = 1.5$ years.

 Supplemental Material

The relation between the timescales can be estimated by (e.g., Naoz et al. 2013b)

$$\frac{t_{1\text{PN,inner}}}{t_{\text{quad}}} = \frac{a_1^4}{3a_2^3} \frac{(1 - e_1^2) m_3 c^2}{(1 - e_2^2)^{3/2} (m_1 + m_2)^2 k^2} = \varepsilon_{\text{GR}}^{-1} (1 - e_1^2). \quad (59)$$

Here, we also introduce the parameter $\varepsilon_{\text{GR}}^{-1}$ defined by Liu et al. (2015). When the two timescales are similar to one another, a resonant-like behavior emerges (Ford et al. 2000b, Naoz et al. 2013b). An example for this behavior is shown in **Figure 15a** for different initial mutual inclinations and setting initially $e_1 \rightarrow 0$. The value of this eccentricity can be estimated analytically; then we have

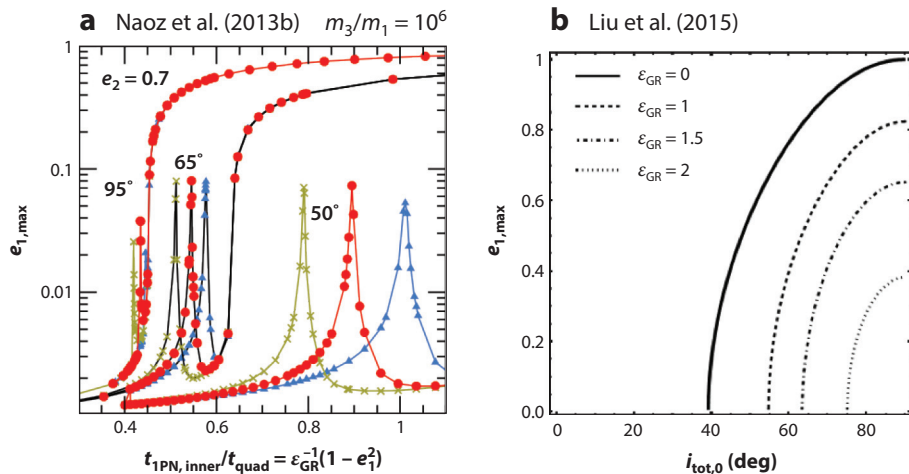


Figure 15

General relativity first post-Newtonian (1PN) expansion effects on the hierarchical three-body system. (a) The emergence of resonant-like eccentricity excitations in the $e_{1,\max} - \epsilon_{\text{GR}}^{-1}$ plane for different initial inclinations. We consider the secular Newtonian evolution and the post-Newtonian evolution including terms only up to $\mathcal{O}(a_1^{-2})$ (inner orbit precession, *blue triangles*), $\mathcal{O}(a_2^{-2})$ (outer orbit precession, *green crosses*), and the interaction term (*red squares*). The location of the resonance will shift when including additional three-body 1PN terms. The system is initialized with $e_1 = 0.001$, $\omega_2 = 0^\circ$, and $\omega_1 = 240^\circ$ and with mutual inclination corresponding to (from left to right) 95° , 65° , and 50° , respectively. The other parameters are $m_3/m_1 = 10^6$, $m_2 \rightarrow 0$, and $e_2 = 0.7$. Adapted from Naoz et al. (2013b) with permission. (b) The analytical solution for the maximum eccentricity in the $e_{1,\max} - i_0$ plane for different values of ϵ_{GR} (note that $\epsilon_{\text{GR}} \rightarrow 0$ means no post-Newtonian contribution). This calculation considers only the inner orbit precession for small ϵ_{GR} and high-inclination test particle orbit. Adapted from Liu et al. (2015) with permission.

a simplified equation for large eccentricity excitations (Liu et al. 2015):

$$\left(\frac{\epsilon_{\text{GR}}}{\sqrt{1 - e_1^2}} \right)_{e_1=e_{1,\max}} \approx \frac{9}{8} e_{1,\max}^2 \frac{j_{1,\min}^2 - 5 \cos^2 i_0/3}{j_{1,\min}^2}; \quad (60)$$

here, we remind the reader that $j_{1,\min} = \sqrt{1 - e_{1,\max}^2} \ll 1$. This behavior is shown in **Figure 15a** (see also Fabrycky & Tremaine 2007). The general expression of Equation 60, which is valid for all values of $e_{1,\max}$, can be found in Liu et al. [2015, their equation 50; however, note that their equation has a typo—the 3/5 in that equation should be 5/3 (B. Liu, D.J. Muñoz, and D. Lai, private communication)]. As shown in this latter study, given an extra short-range force, such as ϵ_{GR} , the maximum eccentricity can be predicted for the octupole level of approximation by considering the perpendicular case of the quadrupole level of approximation.

Interestingly, even if the GR precession timescale is longer than the quadrupole timescale, $t_{\text{1PN,inner}} > t_{\text{quad}}$, GR can have significant implications on the dynamical evolution. Specifically, if $t_{\text{quad}} < t_{\text{1PN,inner}} \lesssim t_{\text{oct}}$, GR precession can retrigger the EKL behavior for similar-mass inner binaries. This can be seen in the example shown in **Figure 12b**, where we compare the pure Newtonian case and the case which includes GR precession for the inner orbit. As depicted, including GR effects retriggers the EKL behavior.

In the secular approximation GR effects are typically taken into account by only including the inner body precession (Equation 57). Sometimes the outer orbit precession is also taken

into account (simply replace 1 with 2 in Equation 57)—this mainly affects the position of the $t_{\text{quad}} \sim t_{1\text{PN,inner}}$ resonance (e.g., Naoz et al. 2013b, and see **Figure 15a**).

In some astrophysical settings higher PN orders of the inner orbit are important (e.g., Blaes et al. 2002, Miller & Hamilton 2002, Wen 2003, Seto 2013, Antognini et al. 2014). In some cases the GR (first PN) term that describes the interactions between the inner and outer orbits may have some effects (Naoz et al. 2013b). However, as shown by Will (2014a,b), when GR effects between the two orbits become more important, the gravitational weak-field approximation is no longer valid, which results in deviations of the dynamics compared with the double-averaging process.

4.2. Tides and Rotation

Similar to the suppression of eccentricity excitations due to GR precession, precession of the nodes due to oblate objects form static tides, or rotating objects, can cause a similar affect. Mazeh & Shaham (1979) first included tidal effects to the hierarchical triple-dynamical evolution (in the TPQ case and assuming small mutual inclinations). This was then generalized in a series of papers by Kiseleva et al. (1998), Eggleton et al. (1998), and Eggleton & Kiseleva-Eggleton (2001), based on Hut (1980) equilibrium and static tides formalisms. The strength of the equilibrium tide recipe presented here is that it is self-consistent with the secular approach. Furthermore, assuming polytropic stars, this recipe has only one dissipation parameter for each member of the binary. In other words, tides can be considered for both members of the inner orbit. Using this description one is able to follow the precession, due to oblateness and tidal torques, of the spin of the star and the planet. We provide the set of equations in **Supplemental Text 2: Static Tides Equations**. Different choices of the tidal model can result in quantitatively different results, such as the relevant separations at which eccentricity excitations are suppressed and the time evolution of the circularization and orbital shrinking process.

During the system evolution, the EKL mechanism can cause large eccentricity excitations for the inner orbit (for example, see **Figures 7** and **11**). Thus, on one hand, the nearly radial motion of the binary drives the two inner binary members to merge, whereas on the other hand, the tidal forces tend to shrink and circularize the orbit (see **Figure 16**, panels *b,d* and *a,c*, respectively). If during the evolution the tidal precession timescale (or the GR timescale) is similar to that of the quadrupole timescale (which is the shortest secular timescale; Equation 27), further eccentricity excitations are suppressed. In this case tides can shrink the binary semimajor axis and form a tight binary decoupled from the tertiary companion. In other words, the precession timescale associated with the gravitational perturbations from the tertiary is slower than the short-range precession timescales. The final separation may remain on a stable orbit (note that tides always tend to shrink the binary separation, but this happens on much longer timescales). An example of this behavior is shown in **Figure 16a,c**. However, if the eccentricity is excited on a much shorter timescale than the typical tidal (or GR) precession timescale (but, of course, still long enough so the secular approximation is valid), the orbit becomes almost radial, and tidal precession does not have enough time to affect the evolution. In this case the pericenter distance may be shorter than the Roche limit of at least one of the binary members (see Equation 54). An example of this behavior is shown in **Figure 16b,d**.

The typical timescales associated with these precessions are (see Equations 86–90 in **Supplemental Text 2: Static Tides Equations** for the sources of these timescales)

$$t_{\text{Tide}} \sim \frac{a_1^{13/2} m_2 (1 - e_1^2)^5}{\sqrt{k} k_{L,2} f_T(e) m_1 (m_1 + m_2) R_2^5} \quad (61)$$

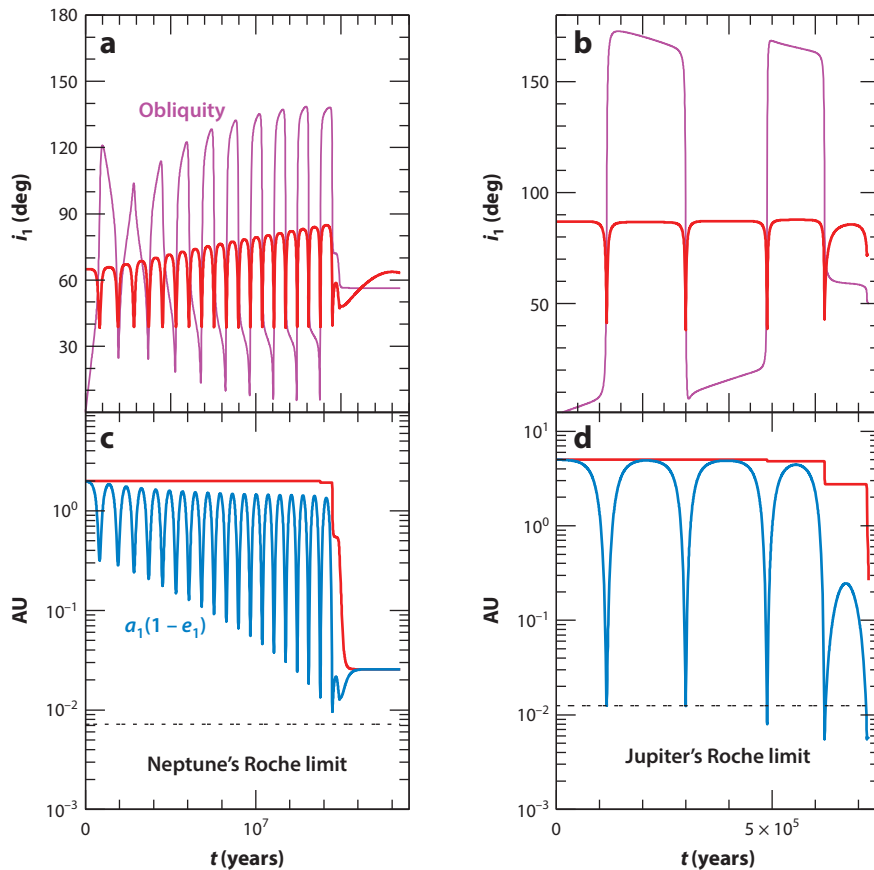


Figure 16

(*a,c*) Circularization and shrinking of the orbits due to tides and (*b,d*) tidal disruption. Panels *a* and *b* show the systems' mutual inclination (red lines) and obliquity (magenta lines). Panels *c* and *d* show the semimajor axes (red lines) and pericenter distances (blue lines) in astronomical units. Also shown in dashed lines are the pericenters at which tidal disruption takes place according to Equation 54, adopting $\eta = 2.7$ (e.g., Guillochon et al. 2011, Liu et al. 2013). Panels *a* and *c* consider a Neptune-sized planet around a 0.32- M_\odot M-dwarf star, initially set at $a_1 = 2$ AU and $e_1 = 0.01$. The third object is a brown dwarf with $m_3 = 10 M_J$ at 50 AU, with $e_2 = 0.52$. The orbits have initially $\omega_1 = \omega_2 = 0^\circ$ and a mutual inclination of 65° . The spin periods of the star and planet were assumed to be 4.6 days and 1 day, respectively. Panels *b* and *d* consider a Jupiter-mass planet at a 5-AU separation from a 1- M_\odot star with a 1- M_\odot stellar companion at 200 AU. The system initially sets with $e_1 = 0.001$, $e_2 = 0.75$, $\omega_1 = \omega_2 = 0^\circ$, and $i = 87^\circ$. The spin periods of the star and planet were assumed to be 24 days and 10 days, respectively. Both systems start initially aligned (i.e., zero obliquity for both the planet and the star) and $T_{V,1} = 50$ years and $T_{V,2} = 1.5$ years.

and

$$t_{\text{Rot}} \sim \frac{\sqrt{k} a_1^{7/2} m_2 (1 - e_1^2)^2}{k_{q,2} \Omega_{s,2}^2 \sqrt{1 + m_2} R_2^5} \quad (62)$$

for tidal and rotational precessions, respectively. We define

$$f_T(e_1) = 1 + \frac{3}{2} e_1^2 + \frac{1}{8} e_1^4, \quad (63)$$

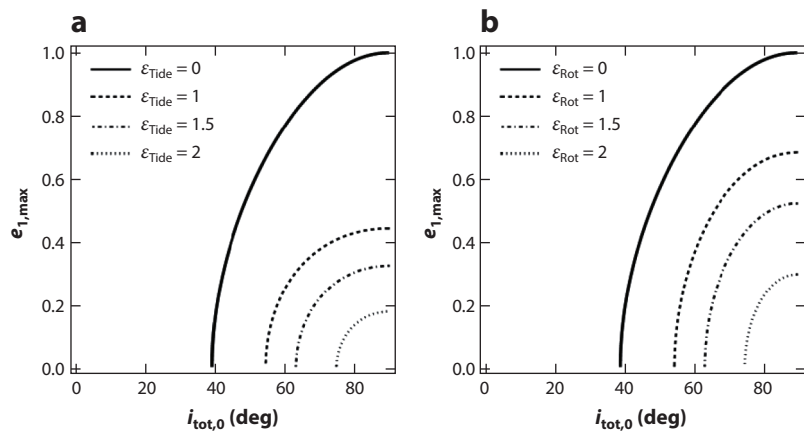


Figure 17

Maximum eccentricity in the presence of (a) tides and (b) rotation. Adapted from Liu et al. (2015) with permission.

and R_1 and $\Omega_{s,2}$ are the radius and spin rate, respectively, of m_2 . Furthermore, $k_{L,2}$ is its Love parameter, and $k_{q,2}$ is the apsidal motion constant. Similar to the GR case, Liu et al. (2015) defined $\varepsilon_{\text{Rot}} = t_{\text{quad}}/t_{\text{Rot}}(1 - e_1^2)^2$ and $\varepsilon_{\text{Tide}} = t_{\text{quad}}(1 - e_1^2)^5/[t_{\text{Tide}}f_T(e_1)]$. With these definitions, Equation 60 can be generalized (Liu et al. 2015):

$$\left[\frac{\varepsilon_{\text{GR}}}{\sqrt{1 - e_1^2}} + \frac{1}{15} \frac{\varepsilon_{\text{Tide}}}{(1 - e_1^2)^{9/2}} \tilde{f}(e_1) + \frac{1}{3} \frac{\varepsilon_{\text{Rot}}}{(1 - e_1^2)^{3/2}} \right]_{e_1=e_{1,\text{max}}} \approx \frac{9}{8} e_{1,\text{max}}^2 \frac{j_{1,\text{min}}^2 - 5 \cos^2 i_0/3}{j_{1,\text{min}}^2}, \quad (64)$$

where

$$\tilde{f}(e_1) = 1 + 3e_1^2 + \frac{3}{8}e_1^4. \quad (65)$$

Note that here we used the ε notation introduced by Liu et al. (2015) to avoid confusion with their definition of $\dot{\omega}$, which is different from that used in this review. In **Figure 14**, we show the tidal precession timescale compared with the other relevant timescales for a Jupiter-mass planet around a Sun-like star. The maximum eccentricity that can be achieved as a function of inclination for a test particle approximation and $e_{1,0} \sim 0$ is shown in **Figure 17**.

5. APPLICATIONS

There are a few main general commonalities between all applications, which we discuss below. The first is the possible outcome due to eccentricity excitation of the inner orbit. As shown in **Figure 16**, these high eccentricities can result in tidal evolution that will lead to tight inner binaries, or they will result in Roche limit crossing. For a different astrophysical setting this can result in mergers, collisions, tidal disruption events, supernova, etc. Another general outcome is that an initial isotropic distribution of inclination of triple systems is not conserved. In the following, we review a few of the examples of these applications to different astrophysical systems.

5.1. Solar System

Kozai (1962) studied the secular dynamical evolution of an asteroid, at 2 AU, due to Jupiter's gravitational perturbations in the framework of the TPQ approximation. He showed that the

asteroid undergoes large eccentricity and inclination oscillations. Considering the hierarchical nature of the approximation, we note that the system is in fact not valid to be addressed by secular approximation. The semimajor axes ratio between the asteroid (2 AU) and Jupiter (5 AU) yields a rather large value ($a_1/a_2 = 0.6$), which suggests that the hierarchical approximation is not valid. Furthermore, Kozai (1962) assumed that Jupiter's eccentricity is strictly zero. Taking into account Jupiter's eccentricity of ~ 0.05 leads to a nonnegligible contribution from the octupole level of approximation $\epsilon = 0.03$; this suggests that the EKL mechanism may significantly alter the evolution of the asteroid. This is shown in **Figure 18**, which considers the TPQ approximation but also considers the EKL evolution. **Figure 18** shows that the TPQ approximation is rather inadequate to address this problem. Furthermore, as mentioned, Jupiter is not far enough away to utilize the hierarchical approximation for this problem, which can be seen from the N -body simulation result obtained using the Mercury software package (Chambers & Migliorini 1997). We used both Bulirsch–Stoer and symplectic integrators (Wisdom & Holman 1991). This calculation shows that indeed the asteroid may impact the Sun and that the actual evolution of the system is closer in behavior to the EKL (TPO in this case) than the TPQ approximation.

As mentioned above, the TPQ approximation can successfully describe the evolution of a variety of test particle systems in the Solar System. For example, it was used to explain the inclinations of gas giant satellites and Jovian irregular satellites (e.g., Kinoshita & Nakai 1991, Vashkov'yak 1999, Carruba et al. 2002, Nesvorný et al. 2003, Čuk & Burns 2004, Kinoshita & Nakai 2007). Furthermore, the importance of secular interactions for the dynamics of comets and other test particles in the Solar System was noted in several studies (e.g., Kozai 1979, Quinn et al. 1990, Bailey et al. 1992, Thomas & Morbidelli 1996, Duncan & Levison 1997, Gronchi & Milani 1999, Gomes et al. 2005, Tamayo et al. 2013). Another interesting example of the application of three-body dynamics relates to binary minor planets. Observations suggest that near-Earth asteroid (NEA) binaries are common [about 15% $r_{\text{NEA}} > 300$ m (Pravec et al. 2006, Margot et al. 2015) and perhaps as high as 63% for a larger range of sizes (Polishook & Brosch 2006)]. Furthermore, about 15% of asteroids and high multiples reside in binaries (Pravec et al. 2006), and Nesvorný et al. (2011) suggested that the binary fraction in the Kuiper belt can be as high as 40%. In all of these cases a natural third body is simply the Sun, which gravitationally perturbs the binary orbit. Perets & Naoz (2009) and Naoz et al. (2010) have studied the evolution of binary minor planets, in the frame work of TPQ, and showed that the dynamical evolution largely affects the observed orbital distribution of these objects. Specifically, they showed that in the inclination–separation phase space there is a regime associated with high mutual inclination that is devoid of eccentric wide binaries. Eccentricity excitations in this regime, due to the Sun's gravitational perturbation, can lead to shrinking and circularizing of the binary's orbit or even lead to binary coalescences. Furthermore, Kinoshita & Nakai (1991, 2007), Vashkov'yak (1999), Carruba et al. (2002), Nesvorný et al. (2003), and Čuk & Burns (2004) suggested that secular interactions and Kozai oscillations may explain the significant inclinations of gas giant satellites and Jovian irregular satellites. Binaries that are closer to the Sun, such as binary asteroids and near-Earth binaries, will be sensitive to a wider range of physical effects, and specifically the induced precession of the binary due to an oblate object may suppress eccentricity excitations (Fang & Margot 2012). Another potentially important mechanism is the YORP (Yarkovsky-O'Keefe-Radzievskii-Paddack) effect, which can significantly alter the spin of asteroids and near-Earth objects (e.g., Polishook & Brosch 2009). This in turn can result in even larger effects on the precession due to rotation.

5.2. Planetary Systems

Recent ground- and space-based observations have transformed our understanding of the properties of exoplanetary systems. The detection of several thousand planets and planet candidates

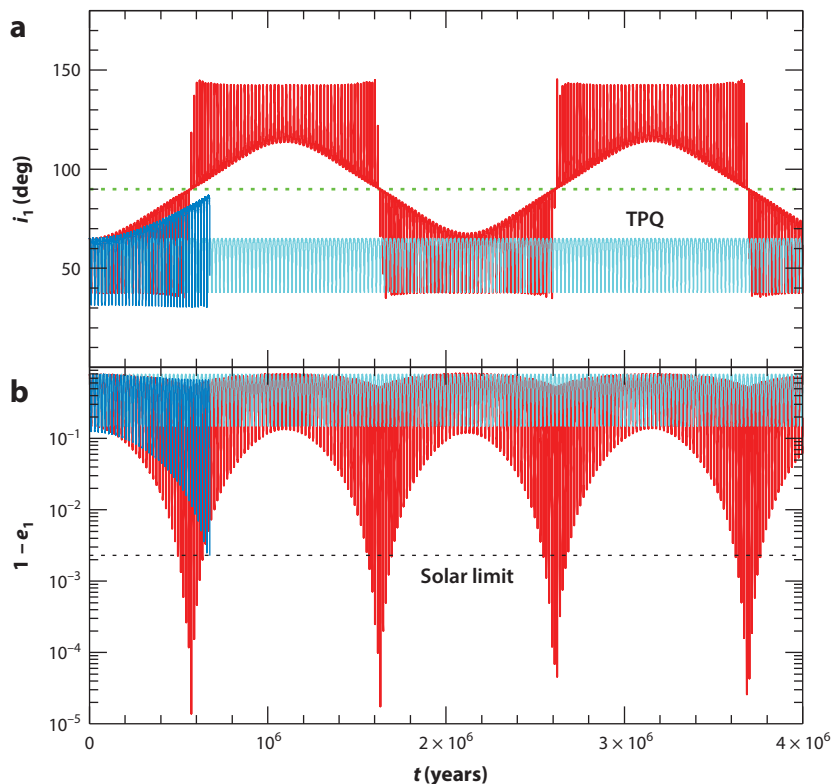


Figure 18

Kozai's (1962) study of secular evolution of an asteroid due to Jupiter's gravitational perturbations. The system is set with $m_1 = 1 M_\odot$, $m_2 \rightarrow 0$, and $m_3 = 1 M_J$, with $a_1 = 2$ AU and $a_2 = 5$ AU. We initialize the system with $e_1 = 0.2$, $e_2 = 0.05$, $\omega_1 = \omega_2 = 0^\circ$, and $i_{\text{tot}} = 65^\circ$. We consider the test particle quadrupole (TPQ) evolution (cyan lines) and the EKL evolution (red lines). The dashed green line in panel *a* marks the 90° boundary. The result of an N -body simulation (blue lines) is also shown. The thin horizontal dotted line in panel *b* marks the eccentricity corresponding to a collision with the solar surface, $1 - e_1 = R_\odot/a_1$. At this instance, we have stopped the numerical integration. Adapted from Naoz et al. (2013a) with permission.

have revealed many puzzles that challenge traditional planet-formation theories and have generated many new ideas. One of the greatest mysteries in the past two decades lays in a class of giant planets called hot Jupiters. These are Jupiter-sized planets that are found in extremely short-period orbits around their host stars (i.e., periods of a few days or less). Most theories posit that these planets still form on larger (greater than astronomical units) scales, like in the Solar System, but move inward to short orbital periods. Thus, a migration mechanism is needed to reduce the angular momentum of these planets by two orders of magnitude (from a few astronomical units to about a few percent of an astronomical unit). Broadly speaking, there are two main channels considered in the literature to achieve this. In the first channel, planets form in the disk, and in some cases, angular momentum exchange between the planets and the protoplanetary disk can produce inward migration (e.g., Lin & Papaloizou 1986, Masset & Papaloizou 2003). In the second channel, planets also form in the disk, but dynamical interactions between multiple planets or a stellar companion greatly affect the final orbital configuration of the system through a variety of mechanisms such as planet-planet scattering (e.g., Rasio & Ford 1996), EKL (see below), or

secular chaos (Lithwick & Wu 2012, Hansen & Zink 2015). The role of planet or stellar dynamical interactions is motivated by the presence of substantial eccentricities among the more distant Jovian population, and the discovery of high obliquities (misalignments between planetary orbital and host-star spin directions; e.g., Albrecht et al. 2012b). Both of these features would tend to be damped by the dissipative interactions with a protoplanetary disk and have spawned an interest in processes that can lead to migration through predominantly dynamical interactions.

The first application of three-body secular interaction to a planetary system began with the detection of 16 Cyg B (Cochran et al. 1996), where Holman et al. (1997) and Mazeh et al. (1997) attributed its high eccentricity ($e \sim 0.63$) to the Kozai-Lidov mechanism (in the framework of the TPQ approximation). They also showed that the planet spends about $\sim 35\%$ of its lifetime in a high eccentric orbit, $e > 0.6$. In subsequent nominal studies by Wu & Murray (2003), Wu et al. (2007), and Fabrycky & Tremaine (2007) the consequences of the TPQ approximation in forming hot Jupiters in stellar binaries was investigated in greater detail and included GR and tides. As the orbit evolves dynamically owing to gravitational perturbation from the outer orbit, the planet's orbit becomes eccentric and the planet spends long times around the host star. At these intervals, tides on the planet and on the star affect the orbit, which tends to circularize and shrink it. This scenario was suggested as a possible formation channel for hot Jupiters without the need for disk migration (Lin & Papaloizou 1986).

As an aftermath of using the TPQ approximation these studies found that in order to form hot Jupiters the initial mutual inclination needs to be rather close to perpendicular ($90^\circ \pm 3^\circ$; e.g., Fabrycky & Tremaine 2007). An important outcome from these calculations was the prediction of retrograde hot Jupiters (i.e., obliquities larger than 90° ; Fabrycky & Tremaine 2007, Wu et al. 2007). The recent detections of retrograde hot Jupiters (e.g., Triaud et al. 2010, Winn et al. 2010, Albrecht et al. 2012b) resulted in new interest in the possibilities that secular three-body interactions present for this field.

The formation of hot Jupiters via the EKL mechanism, including GR and tides for two-planet systems, was studied by Naoz et al. (2011); see **Figure 19**. A simplified Monte Carlo simulation for initially an aligned Jupiter in a two-planet system resulted in a nearly uniform obliquity distribution, as well as a nearly uniform mutual inclination distribution. Similar results for the inclination and obliquity distributions were achieved for the formation of hot Jupiters in stellar binary systems (effectively repeating the analysis by Fabrycky & Tremaine 2007, but for the EKL mechanism and exploring a larger range of orbital parameters). The obliquity distribution is shown in **Figure 20a**. Projecting the resulted obliquity angles on the sky (see **Figure 20b**) allows for direct comparison with observations (e.g., Morton & Johnson 2011). Naoz et al. (2012) performed a Bayesian analysis that treats the complete obliquity distribution as a sum of contributions from an aligned component, an EKL component, and a planet–planet scattering component (adopting Nagasawa & Ida 2011). They found that the EKL most likely accounts for $\sim 30\%$ of the observed systems, and planet–planet scattering contributes $\sim 10\text{--}20\%$ independent of the formation rate. That analysis also showed that EKL produces between 60% and 80% of large obliquity angles. These values are consistent with complementary analyses that showed that hot Jupiters are likely to have a faraway companion (e.g., Knutson et al. 2014, Ngo et al. 2015, Wang et al. 2015).

It was later shown, in the framework of a hierarchical triple system, that the behavior of the obliquity angle is chaotic in nature (Storch et al. 2014, Storch & Lai 2015). The planetary orbital angular momentum vector precesses around the total angular momentum at a rate that is inversely proportional to the quadrupole timescale $\sim t_{\text{quad}}^{-1}$. Due to the rotation-induced stellar quadrupole, the planet induces precession in the stellar spin axis, which is proportional to the stellar spin's angular momentum. As shown by Storch et al. (2014), when the latter precession spin is larger than the orbital precession rate, the stellar spin axis follows \mathbf{G}_1 adiabatically while maintaining an

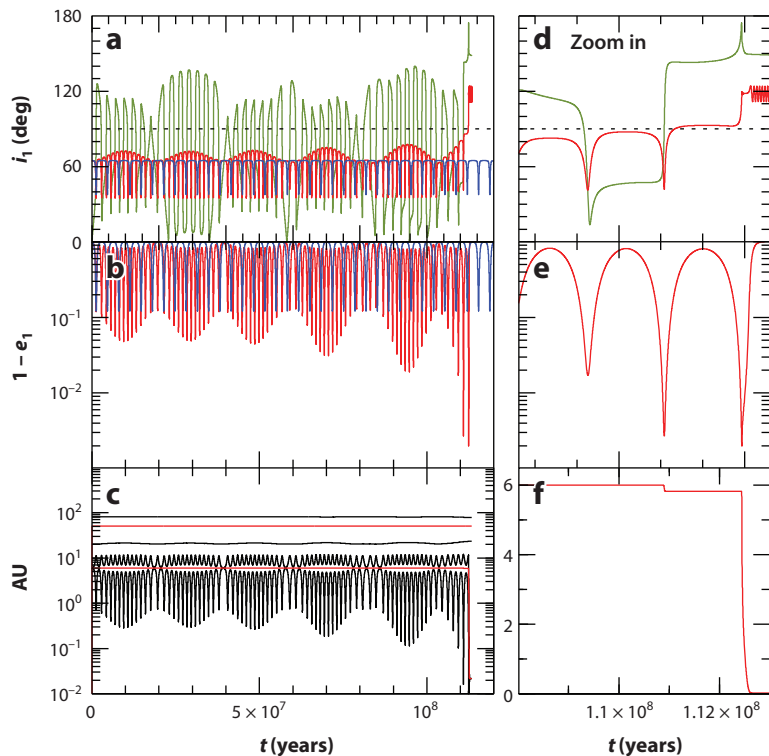


Figure 19

Hot Jupiter formation in a two-planet system. Panels show (*a,b,c*) the full evolution and (*d,e,f*) zoom ins on the final three quadrupole cycles, with the evolution of the obliquity. We consider the full, octupole-level evolution, which includes general relativity (GR) and tides evolution (*red lines*), and the quadrupole level, which includes GR and tides (*blue lines*). Panels *a* and *d* show the inclination of the system of the full, up-to-the-octupole-level evolution, which includes GR and tides (*red line*), and the inclination for the quadrupole level, including GR and tides (*blue lines*). Green shows the obliquity. Panels *b* and *e* show the eccentricity as $1 - e_1$ (again, *red lines* are for the octupole and *blue lines* are for the quadrupole). Panels *c* and *f* show the semimajor axes for the outer (top) and inner (bottom) binaries (*red lines*) and their apocenters and pericenters (*gray lines*). Note that panel *c* is log scaled, whereas panel *f* is linear scaled. The system parameters are: $m_1 = 1 M_{\odot}$, $m_2 = 1 M_J$, $m_3 = 3 M_J$, $a_1 = 6$ AU, $a_2 = 61$ AU, $e_1 = 0.001$, $e_2 = 0.6$, $\omega_1 = 45^\circ$, $\omega_2 = 0^\circ$, and $i_{\text{tot}} = 71.5^\circ$. The system started with zero obliquity, and the spin periods of the star and the planet are 25 days and 10 days, respectively. The viscous times here are $t_{V,1} = 5$ years and $t_{V,2} = 1.5$ years; the spin period of the star was assumed to be 25 days. Adapted from Naoz et al. (2011) with permission.

approximately constant obliquity. In the other extreme case, when the maximal spin precession rate is always smaller than the orbital precession rate, the spin axis effectively precesses around the total angular momentum (about which \mathbf{G}_1 is precessing). In the intermediate regime, Storch et al. (2014) showed that a secular resonance occurs, which leads to complex and chaotic spin evolution. Short-range forces can further complicate the obliquity evolution and affect the formation of hot Jupiters (Storch et al. 2014, Storch & Lai 2015).

The large eccentricity excitations induced via the EKL mechanism can result in a nearly radial motion and drive the planet into the star (as illustrated in **Figure 16*b,d***). Thus, the formation fraction of hot Jupiters is highly sensitive to the disruption distance (as shown in **Figure 21**; vertical lines are based on Equation 54). For lower-mass planets, such as rocky planets, tides (or

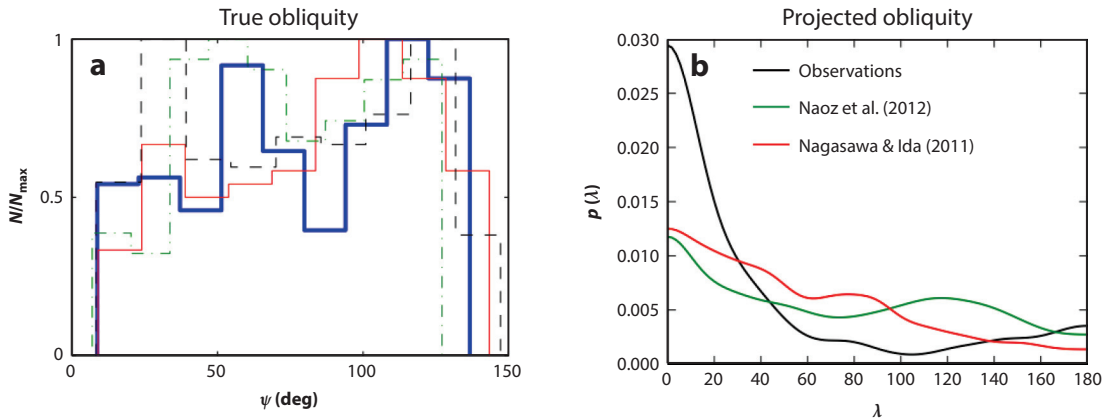


Figure 20

Hot Jupiter obliquity distribution in stellar binaries. (a) The true obliquity (ψ) distribution, as a result of fiducial Monte Carlo simulations by Naoz et al. (2012) (blue line), for a wide range of companion initial separations, setting planetary viscous tides to be $t_{V,2} = 1.5$ years. This distribution has a characteristic cutoff near 140° . This limit arises from the Kozai angles (the separatrix $\sim 140^\circ$) for which the large oscillations take place. Also shown are the results from the Monte Carlo simulations with different settings. In particular, the dashed black line represents a companion at $a_2 = 1,000$ AU, and the thin solid red line represents a companion with $a_2 = 500$ AU. In both cases the planetary viscous tides are set to be $t_{V,2} = 1.5$ years. Also overplotted is a Monte Carlo simulation for a companion separation of $a_2 = 500$ AU with $t_{V,2} = 0.015$ years (dot-dashed green line). (b) The projected obliquity from Monte Carlo simulations by Naoz et al. (2012), as well as the observations (as for 2012) exoplanets.org, and the projected obliquity of Nagasawa & Ida (2011). The stellar spin-period assumed for these figures was 25 days. Different Roche-limit estimates do not change this result (e.g., Petrovich 2015a); however, different stellar spin-periods or evolution of the spin period may result in a deviation from this distribution (Storch et al. 2014). Adapted from Naoz et al. (2012) with permission.

GR, or quadrupole moments from fast rotating stars) are largely ineffective at stopping the EKL's nearly radial motion, resulting in a high probability of tidal disruption (e.g., Lanza & Shkolnik 2014, Rice 2015). Apart from tidally disrupting the planet, binary companions can also lead to large instabilities, which may result in swapping planets between the stars (e.g., Kratter & Perets 2012, Moeckel & Veras 2012). In addition, as the stars evolve beyond the main sequence, the existence of a companion (a star, brown dwarf, or a planet) can lead to ejection of planets (e.g., Veras & Tout 2012; Veras et al. 2013, 2014) or engulfment of the innermost planet (e.g., Li et al. 2014c, Frewen & Hansen 2016).

The observational studies that showed that hot Jupiters are likely to have a faraway companion (e.g., Knutson et al. 2014, Ngo et al. 2015, Wang et al. 2015) promoted further investigations of two-planet systems. As shown in **Figure 11**, a similar-mass perturber yields large eccentricity excitations with suppression of large eccentricities for large mutual inclinations (Teysandier et al. 2013). Therefore an inclined planetary perturber can lead to short-period oblique planets (Naoz et al. 2011, Li et al. 2014c). If large eccentricities are generated, according to the stability criterion in Equation 53 the inner planet can either be ejected from the system or collide with the host star. In some cases, when the forced eccentricity from the perturber causes the orbit to shrink, the orbit reaches a semimajor axis for which tidal precession is comparable with the quadrupole timescale (as noted in Section 4.2). This suppresses further circularization and shrinking of the orbit, which may lead to the formation of eccentric warm Jupiters (Dawson & Chiang 2014; Dong et al. 2014, 2015).

Recently, the *Kepler* mission detected several circumbinary planetary systems (Doyle et al. 2011; Orosz et al. 2012a,b; Welsh et al. 2012, 2015; Kostov et al. 2013, 2014; Schwamb et al. 2013). These systems are composed of a stellar binary on an orbit with a typical period of 7.5 to 41 days orbited

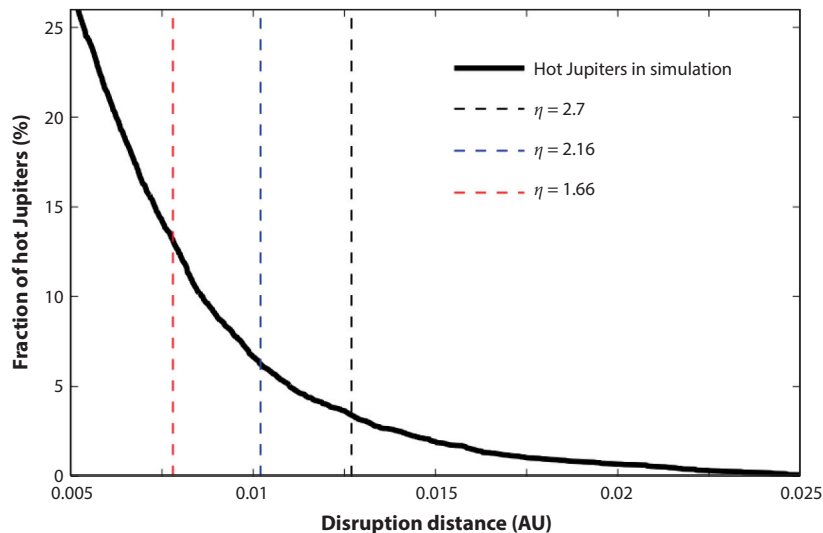


Figure 21

The fraction of hot Jupiters formed in the fiducial Monte Carlo simulation by Petrovich (2015a) as a function of the disruption distance. The vertical lines indicate different disruption distances parameterized by η in Equation 54. The different values ($\eta = 1.66, 2.16,$ and 2.7) correspond to the values adopted in Naoz et al. (2012), Wu et al. (2007), and Petrovich (2015a), respectively. Adapted from Petrovich (2015a) with permission.

by a planetary companion on a much longer period (~ 50 – 250 days). Interestingly, no transiting planets have been found around more compact stellar binaries ($\lesssim 7$ -day period), although these binaries are abundant in nature and in *Kepler* eclipsing binary data (Raghavan et al. 2006, 2010; Tokovinin 2014b). Two main questions about circumbinary planets were addressed recently in the literature. One considered the apparent absence of circumbinary planets around compact stellar binaries, and the other was about the configuration of the planetary orbit. Starting with the former, the formation of compact stellar binaries is often associated with dynamical evolution, which involves a tertiary (e.g., Naoz & Fabrycky 2014, and see below). In the context of this channel, it was suggested that the outer perturber that drives the two stars into a tight orbit may also impact the planetary companion around the inner two stars and may result in a large eccentricity planetary orbit leading to ejection or collision with the inner stars. However, circumbinary planets around compact binaries may still exist, but they probably will end up misaligned with the inner stellar orbit (e.g., Hamers et al. 2016, Martin et al. 2015, Muñoz & Lai 2015). In fact the misalignment can be generated simply from eccentricity and inclination oscillations on the inner orbit, from a test particle as shown in **Figure 4** (e.g., Martin & Triaud 2015b). Therefore, because many of the *Kepler* binary detections are eclipsing binaries, if misaligned systems around stellar systems exist, they are presently hidden from the current *Kepler* detection methods. This may imply that circumbinary planets are rather abundant, perhaps even more than planets around single stars (e.g., Armstrong et al. 2014; Martin et al. 2015; Martin & Triaud 2015a,b; but see Deacon et al. 2016).

5.3. Stellar Systems

Most massive stars reside in a binary configuration ($\gtrsim 70\%$ for massive stars; see Raghavan et al. 2010). It seems that stellar binaries are responsible for diverse astrophysical phenomena, from

Type Ia supernovae to X-ray binaries. However, observational campaigns have suggested that probably many of these binaries are in fact triples (e.g., Tokovinin 1997, 2008; Eggleton et al. 2007). Tokovinin (1997) showed that 40% of binary stars with periods of <10 days in which the primary is a dwarf ($0.5\text{--}1.5 M_{\odot}$) have at least one additional companion. He found that the fraction of triples and higher multiples among binaries with periods of $10\text{--}100$ days is $\sim 10\%$. Moreover, Pribulla & Rucinski (2006) surveyed a sample of contact binaries and noted that among 151 contact binaries brighter than 10 mag, $42 \pm 5\%$ are at least triples. Furthermore, a recent analysis of eclipse time variation curves of *Kepler* binaries showed that indeed a substantial fraction of these binaries have a third body (Borkovits et al. 2016). Thus, it seems that triple stars are abundant in our Galaxy. From dynamical stability arguments these must be hierarchical triples, in which the (inner) binary is orbited by a third body on a much wider orbit.

Application of the secular hierarchical triple-body system to triple-stellar system was first considered by Harrington (1968, 1969). His work was motivated by Heintz (1967), who observed triple-stellar systems with possible perturbations from the outer orbit. In this early work he already recognize the importance of the octupole level of approximation and expanded the Hamiltonian up to the octupole level of approximation. From the equations of motion he estimated a distribution for the inner orbit specific angular momentum $\sqrt{1 - e_1^2}$ to match the observed distribution of triples. Later, Mazeh & Shaham (1979) showed that tidal effects during eccentricity excitations of the Kozai-Lidov cycle can circularize and shrink the orbit.

During system evolution, the star can cause large eccentricity excitations for the inner orbit. Therefore, the nearly radial motion of the binary drives the two stars to merge; however, tidal forces tend to shrink and circularize the orbit. If during the evolution the quadrupole level of approximation precession timescale is longer than the precession timescale associated with short-range forces (such as tides, e.g., Equation 61, or GR, e.g., Equation 58), further eccentricity excitations are suppressed. In this channel, tidal forces can shrink and circularize the inner orbit, forming a tight inner stellar binary decoupled from the tertiary. This process was studied at great length in the literature as a promising channel to explain triples and close binaries observations (e.g., Söderhjelm 1975, 1982, 1984; Eggleton et al. 1998; Kiseleva et al. 1998; Ford et al. 2000a; Eggleton & Kiseleva-Eggleton 2001; Fabrycky & Tremaine 2007; Perets & Fabrycky 2009; Thompson 2011; Shappee & Thompson 2013; Naoz & Fabrycky 2014). We show here the updated inner orbit specific angular momentum simulated distribution compared to observations in **Figure 22c**, reproducing Harrington's (1968) figure 3. Observations are taken from Raghavan et al. (2010) and Monte Carlo simulations are adopted from Naoz & Fabrycky's (2014) EKL triple-star simulations.

Naoz & Fabrycky (2014) ran a large Monte Carlo simulation—including the EKL mechanism, tides (as described in **Supplemental Text 2: Static Tides Equations**), and GR—for 10 Gyr of evolution, producing the distribution for semimajor axis, eccentricity, inclination, and obliquity. The observed bimodal distribution of the inner orbit reported by the Tokovinin (2008) public catalog (see **Figure 22a**) is reproduced by Naoz & Fabrycky's (2014) simulations. Their Kolmogorov-Smirnov test does not reject the null hypothesis that the observed inner orbit period's distribution and the simulated one are from the same continuous distribution. Furthermore, they found that the simulated outer orbit distribution of the close binaries is consistent with that from the Tokovinin (2008) catalog of observed triples (e.g., **Figure 23**). Thus, they concluded that secular evolution in triples plays an important role in shaping the distribution of these systems.

Tokovinin & Smekhov (2002) reported that wide binaries are more likely to have nonnegligible eccentricity (see also Tokovinin & Kiyaveva 2015). For wide binaries in triple systems this seems to be in agreement with the dynamical eccentricity excitation from an outer perturber where tidal shrinking and circularization are less efficient (as can be seen in **Figure 22c**). The systems



Inner binaries – Naoz & Fabrycky

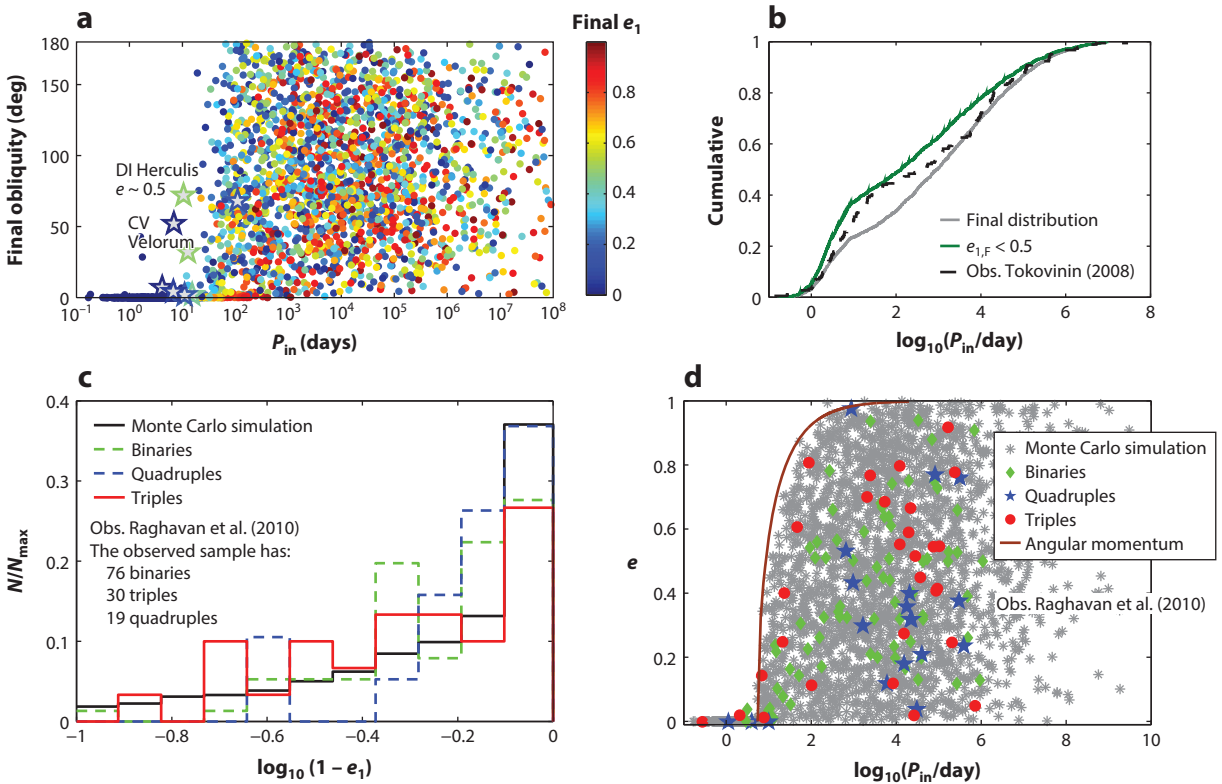


Figure 22

Simulated inner binary orbital configuration compared with observations. (a) Final distribution of the spin orbit angle (i.e., the obliquity) of the primary versus the final period of the inner orbit, the color code is the final eccentricity of the inner binary. We also plot the observations (Albrecht et al. 2009, 2011, 2013, 2014; Harding et al. 2013; Triaud et al. 2013; Zhou & Huang 2013). (b) The cumulative distribution of the observations distribution taken from the Tokovinin (2008) public catalog (*dashed black line*) compared with the final distribution (*solid gray line*). Because the public catalog has typical inner orbital eccentricity of 0.5, the final distribution is also shown for the system with $e_{1,F} < 0.5$ (*solid green line*). (c) The inner orbit final eccentricity as a function of the final period. Overplotted are observations adopted from the Raghavan et al. (2010) public catalog. The solid line represents a constant angular momentum curve with a final binary period of 5.5 days. (d) Reproduction of the inner orbit specific angular momentum distribution considered first by Harrington (1968) and compared to observations by Raghavan et al. (2010). Panels a, b, and c and the Monte Carlo simulations are adapted from Naoz & Fabrycky (2014) with permission.

near the constant angular momentum line may represent a population of migrating binaries due to tidal dissipation (as also seen in the *Kepler* binary stellar population; e.g., Dong et al. 2013). Furthermore, the formation channel of close stellar binaries via EKL and tides was suggested to somewhat suppress the likelihood of finding aligned circumbinary planets around tight stellar binaries (e.g., Hamers et al. 2016, Martin et al. 2015, Muñoz & Lai 2015).

An interesting and promising observable for triple-stellar dynamics may be the obliquity angle. As more binary stars' obliquities are being observed [e.g., by the BANANA survey (Albrecht et al. 2012a), and by other individual endeavors], the obliquity distribution may provide a key observable. During the tidal evolution the obliquity of the tight binaries most likely decays to zero faster than the eccentricity. This causes systems that are close to the angular momentum line to have typically

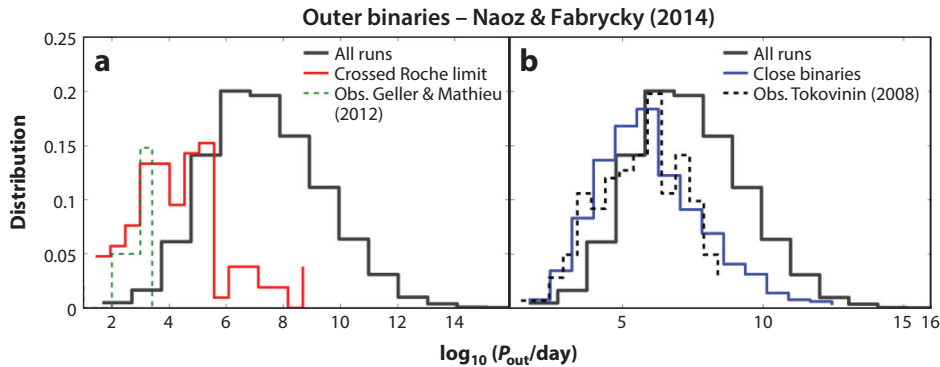


Figure 23

Simulated outer binary period compared with observations. (a) The period of companions for the merged stellar population (red line) and the observed blue stragglers binary distribution of NGC 188 (Geller & Mathieu 2012), also scaled to match the theory lines. (b) The period distribution of the companion of the close binaries (blue line); the latter is defined to have periods shorter than ~ 16 days. Overplotted is the observed distribution, scaled to match the theory lines, adopted from the Tokovinin (2008) public catalog. In both panels, gray lines represent the period distribution at the final stage of all of the outer companions in the Monte Carlo runs. Adapted from Naoz & Fabrycky (2014) with permission.

low obliquities (Naoz & Fabrycky 2014). This behavior is depicted in **Figure 22a**, which shows that the final obliquity distribution of close binaries with moderate eccentricities have moderate obliquities. Close circular inner binaries with nonnegligible obliquities (> 10 deg) are found to have smaller spin periods (see also Fabrycky et al. 2007, Levrard et al. 2007). The simulated stellar obliquities shown in **Figure 22** are consistent with the current available observations.

Strong gravitational perturbations can lead to mergers of the inner members, if the tidal forces cannot react fast enough to stabilize the system (see, for example, **Figure 16b,d**). In the previous section, we discussed tidal disruptions of hot Jupiters due to large eccentricity excitations. In the context of triple-stellar systems, extreme values of the eccentricity that take place on shorter timescales than that of the short-range forces (such as GR and tides), but still long enough to allow the system to remain secular, may lead to the merger of stellar binaries. If sufficient time has passed from the merger time (perhaps on the order of a Kelvin-Helmholtz timescale), this merger product may be identified as a blue straggler. Perets & Fabrycky (2009) envisioned a two-step process for which triple-body interactions can form blue stragglers. In their study, three-body dynamics plus tidal dissipation created a close binary, and that binary subsequently merged by magnetic breaking or had unstable or efficient mass transfer. Naoz & Fabrycky (2014) suggested that large eccentricity excitation during the EKL evolution can lead to mergers. They found that their simulated outer orbital period distribution is consistent with observations for the companion of the merged population, adopted from Geller & Mathieu (2012), as depicted in **Figure 23**. This further emphasizes the notion that three-body secular interactions may be the main channel for merged systems like blue stragglers.

Another example of interesting evidence for a merged system via perturbations from a distant perturber was recently found in the Galactic Center. Specifically, it seems that the object known as G2 (Gillessen et al. 2012) is a binary star in disguise (Witzel et al. 2014). Therefore, a similar mechanism to that of the formation of blue stragglers may operate in the Galactic Center, where the massive black hole in the center of the Galaxy causes large eccentricity excitations on a stellar

binary in its vicinity (e.g., Antonini & Perets 2012, Prodan et al. 2015; also Stephan et al., in preparation).

The secular approximation allows for long integration times in which stellar evolution may play an important role (e.g., Perets & Kratter 2012, Shappee & Thompson 2013). In particular, in systems that have inner binary members with close mass values (i.e., $m_1 \approx m_2$), the octupole level is suppressed [recall the definition of ϵ_M (Equation 45) and **Figure 12**]. However, stellar mass loss during post-main-sequence evolution can dramatically change the mass balance and retrigger the EKL behavior (Shappee & Thompson 2013). This is because the semimajor axis changes in proportion to the mass-loss ratio, i.e., $a_f/a_i = m_f/m_i$, where the subscripts f and i refer to the final and initial values. Note that adiabatic mass loss conserves the value of the orbital eccentricity. Thus, the ϵ_M due to mass loss can change in comparison to the initial value (e.g., Shappee & Thompson 2013, Michaely & Perets 2014, Naoz et al. 2016):

$$\frac{\epsilon_{M,f}}{\epsilon_{M,i}} = \frac{m_{1,f} + m_2 + m_3}{m_{1,i} + m_2 + m_3} \left(\frac{m_{1,f} - m_2}{m_{1,i} - m_2} \right) \left(\frac{m_{1,i} + m_2}{m_{1,f} + m_2} \right)^2. \quad (66)$$

For simplicity for this equation, we assumed that only one mass will undergo mass loss ($m_{1,i} \rightarrow m_{1,f}$). Overall the absolute value of ϵ_M via this process increases. An example of this evolution is shown in **Figure 24**. The system is set initially with an inner binary composed of two stars of similar mass. As the more massive star loses mass the new ϵ_M increases, according to Equation 66, allowing for larger eccentricity excitations. When the stars inflate in radius as they leave the main sequence, the disruption distance associated with their Roche limit increases as well (e.g., Equation 54). The eccentricity excitations were too small to affect the orbit before the first NS was born. However, during the large eccentricities excitation after ϵ_M increased; the inflation in radius of the less-massive star resulted in this star crossing its Roche limit. This may form a high-mass X-ray binary (HMXB) that may be associated with a supernova impostor (as suggested for a binary interaction for supernova 2010d; e.g., Binder et al. 2011). Another possible outcome for this system is a Thorne-Żytkow object (e.g., Thorne & Zytlow 1975), which has distinct observational signatures (e.g., Levesque et al. 2014). Recently, Naoz et al. (2016) showed that triple dynamics can offer a possible formation channel to low-mass X-ray binaries (LMXBs) while skipping the common envelope phase and, by that, overcoming the challenges that arise with the standard formation scenario (for more details about the challenges in the standard formation see Podsiadlowski et al. 2003).

Shappee & Thompson (2013) suggested that retriggering the EKL behavior via mass loss may facilitate the formation of close NS–WD binaries (or other combinations such as NS–NS, or WD–WD) without an initial common envelope phase. If compact objects such as double WDs in triples find themselves in the right part of the parameter space, the above process may trigger large eccentricities that can lead to grazing interactions or even collisions (recall that the approximation may break, yielding even larger eccentricities), which may promote Type Ia supernovae (e.g., Thompson 2011, Katz & Dong 2012, Hamers et al. 2013, Kushnir et al. 2013, Prodan et al. 2013, Dong et al. 2015).

5.4. Compact Objects

Within the hierarchical galaxy-formation paradigm and the strong observational evidence that a high abundance of the local galaxies host supermassive black holes, one expects that major galaxy mergers should inevitably result in the formation of supermassive black hole binaries or multiples (e.g., Valtonen 1996, Di Matteo et al. 2005, Hoffman & Loeb 2007, Callegari et al. 2009, Dotti et al. 2012, Khan et al. 2012, Kulkarni & Loeb 2012). The evolution of these binaries highly

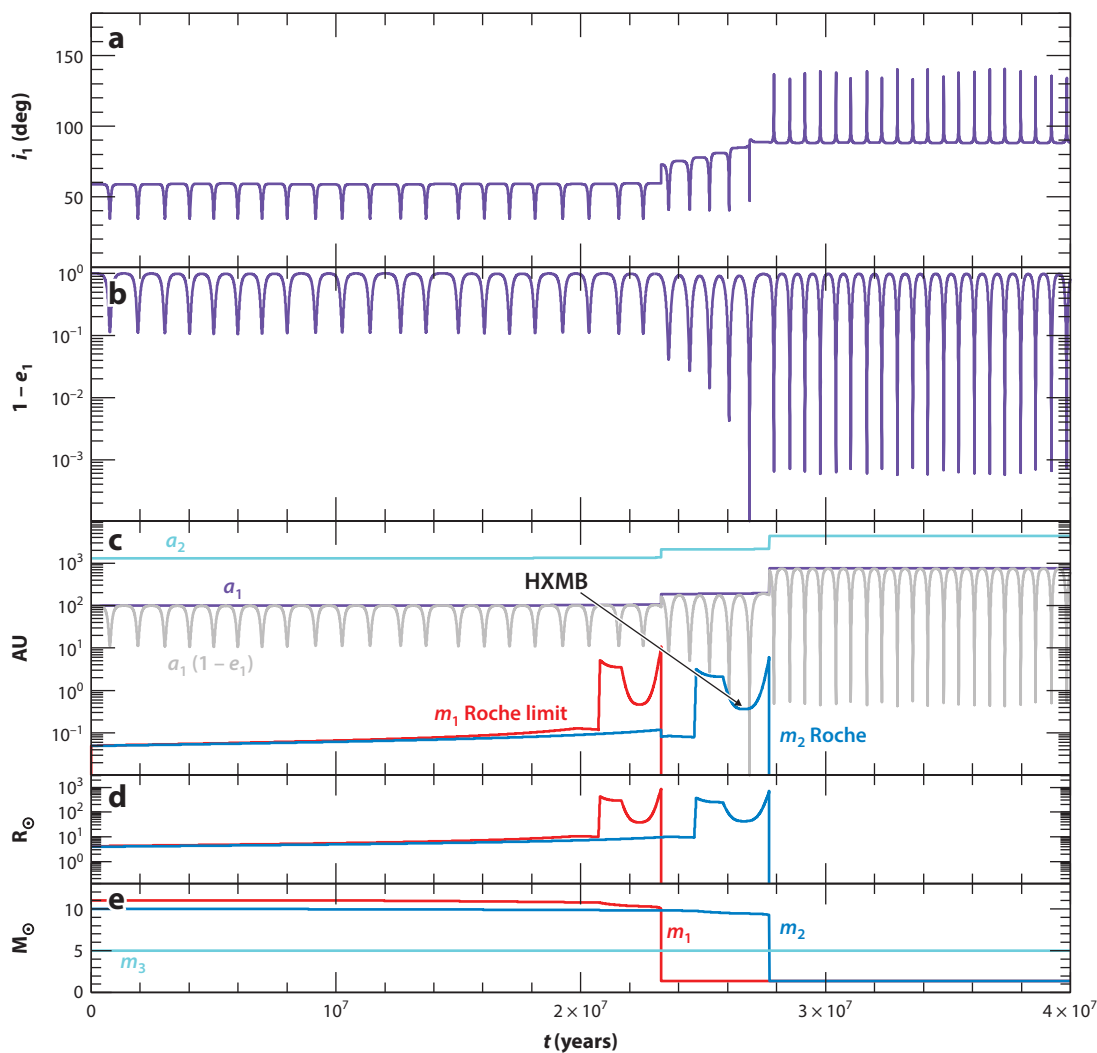


Figure 24

Retriggering EKL by mass loss. This example produces a high-mass X-ray binary (HMXB) or a supernova impostor. We show (a) the inner orbit inclination i_1 , (b) the inner orbit eccentricity (depicted as $1 - e_1$), (c) the semimajor axis of the inner (purple) and outer (cyan) orbit as well as the inner orbit pericenter and the two masses' disruption distances (see Equation 54 for a popular definition), (d) the stellar radii, and finally (e) the masses of all three stars. This calculation includes solving the equations of the octupole level of approximation, GR for both the inner and outer orbits, and stellar evolution according to single-star evolution (Hurley et al. 2000), which includes mass loss and stellar inflation. For simplicity the supernova was modeled here as simple mass loss and assumed no kicks. Tidal evolutions were turned off for illustration purposes. A consequence of the first mass-loss episode and the formation of an NS is that the initially small ϵ_M increased. This yields eccentricity excitations leading to Roche limit crossing as the m_2 star's radius inflates. This may result in an HMXB or even a supernova impostor. The system parameters are set initially as follows: $m_1 = 11 M_\odot$, $m_2 = 10 M_\odot$, $m_3 = 5 M_\odot$, $a_1 = 100$ AU, $a_2 = 1,300$ AU, $e_1 = 0.001$, $e_2 = 0.6$, $\omega_1 = \omega_2 = 0$, and $i_{\text{tot}} = 79^\circ$. These parameters yield initial $\epsilon_M = 0.0034$. Naoz et al. (2016) discussed the formation scenario of low-mass X-ray binaries via triple-body evolution similar to the example illustrated here.

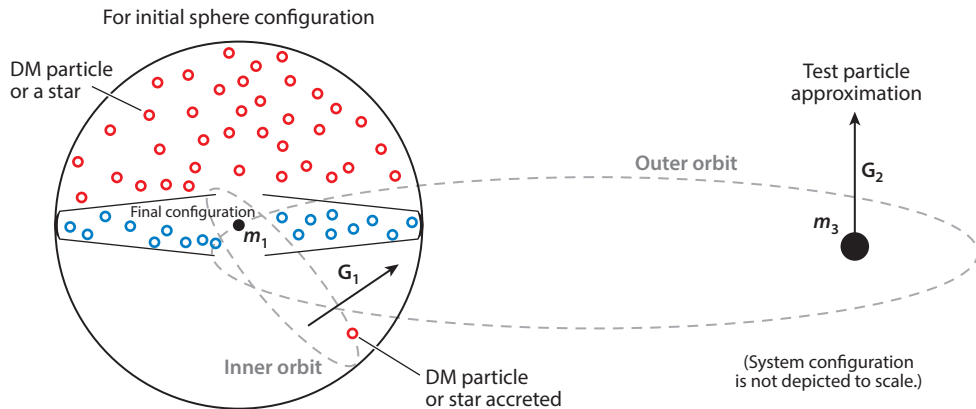


Figure 25

Diagram of the resulting torus-like configuration from EKL in supermassive black hole binaries. The particles in a near-polar orbit, with respect to the black hole binary orbit, will undergo large eccentricity and inclination oscillations. This leads to large eccentricities that will result in either tidal disruption events for stars (Li et al. 2015) or accretion of dark matter (DM) particles that may orbit the black hole (Naoz & Silk 2014).

depends on the conditions of the host galaxy. Numerical studies of spheroidal gas-poor galaxies suggest that these binaries can reach about a parsec separation and may stall there (e.g., Begelman et al. 1980, Milosavljević & Merritt 2001, Yu 2002). The effect of gravitational perturbations of supermassive black hole binaries on an ambient star cluster has been discussed in length in the literature (e.g., Blaes et al. 2002; Miller & Hamilton 2002; Wen 2003; Ivanov et al. 2005; Chen et al. 2009, 2011; Gualandris & Merritt 2009; Freire et al. 2011; Iwasawa et al. 2011; Sesana et al. 2011; Gualandris & Merritt 2012; Madigan & Levin 2012; Meiron & Laor 2013; Antonini & Merritt 2012; Bode & Wegg 2014; Naoz & Silk 2014; Ransom et al. 2014; Tauris & van den Heuvel 2014; Wang et al. 2014; Li et al. 2015). In particular, it was suggested that three-body interactions may play an important role in the growth of black holes at the centers of dense star clusters by increasing the tidal directions event rate of stars. It was also shown that interactions with the surrounding stars can either increase or decrease the eccentricity of the supermassive black hole binaries depending on the fraction of counter-rotating-to-coproating stars. Furthermore, the presence of supermassive black holes may increase the stellar tidal disruption event rate and even lead to a torus-like configuration of stars (or dark matter particles) around one of the black holes (see **Figure 25**). The supermassive black hole binary can also lead to an eccentric or ejected population of stars from the cluster.

For a supermassive black hole binary embedded in a dense stellar environment, such as the one in the Galactic Center, other physical processes may affect the precession of a star around the primary black hole. Similar to the short-range forces discussed in Section 4, if the extra precession takes place in an opposite direction to that induced by the EKL mechanism and it takes place on a shorter timescale, then t_{quad} eccentricity excitations may be suppressed. These physical processes may include (but are not limited to) precession caused by the stellar potential, scalar resonant relaxation or reorientation of the orbital plane due to vector resonant relaxation (Kocsis & Tremaine 2011, 2015), or Lense-Thirring precession (Merritt et al. 2010, Merritt & Vasiliev 2012). For the EKL mechanism of supermassive black hole binaries embedded in a dense stellar environment, Li et al. (2015) found that precession caused by the stellar potential and GR may have large effects on the dynamics, whereas the other processes (such as tidal

effects, scalar and vector resonant relaxation, and Lense-Thirring precession) are typically less important.

A dissipation mechanism that may play an important role when black holes (or other compact objects) are involved is GW emission. In this scenario, black hole binary high orbital eccentricity induced by the outer perturber can lead to a more efficient merger rate, due to GW emission (e.g., Blaes et al. 2002). GW emission can also lead to the formation of extreme-mass-ratio binaries, such as supermassive black holes and stellar-mass black holes, or any other test particle, on a tight orbit (e.g., Bode & Wegg 2014). Considering the dynamical evolution of compact objects in the presence of an outer perturber, large eccentricities induced by the perturber can lead to a close approach between the two compact objects such that GW emission decays their orbital separation (e.g., Miller & Hamilton 2002, Wen 2003, Antonini & Perets 2012, Seto 2013). This perhaps can lead to a detectable signal using LIGO5 and VIRGO6 (e.g., Wen 2003 and Naoz et al. 2013b, but see Mandel et al. 2008 and O’Leary et al. 2006). Because GW emission associated with eccentric orbits is stronger and has a very different spectrum relative to its circular counterparts, it was suggested that, using the GW information emitted by the close binary, it might be possible to constrain the mass or distance of the third body (e.g., Galaviz & Brügmann 2011, Yunes et al. 2011).

Recently it was also suggested that black hole–low-mass X-ray binaries (BH-LMXBs) may form via the EKL mechanism (Naoz et al. 2016). During the dynamical evolution of the triple system, the EKL mechanism can cause large eccentricity excitations on the LMXB progenitor, resulting in a BH-LMXB candidate, while skipping the common envelope phase. Interestingly, a substantial number of close binaries with an accreting compact object, e.g., LMXBs and their descendants (e.g., millisecond radio pulsars), are known or suspected triples (Grindlay et al. 1988, Thorsett et al. 1999, Chou & Grindlay 2001, Rasio 2001, Sigurdsson et al. 2003, Zdziarski et al. 2007, Prodan & Murray 2012, Prodan et al. 2015).

6. BEYOND THE THREE-BODY SECULAR APPROXIMATION

There are different channels to consider when going beyond the secular approximation. The first is to consider the validity of the approximation discussed in Section 3, in other words allowing for more compact systems (e.g., $\epsilon > 0.1$, Equation 52), which means considering the implications of having changes in the angular momentum on short timescales compared to the orbital timescale (e.g., Equation 49). The second is to allow for higher multiples.

In considering compact systems, a popular application of the three-body interaction is the merger of two WDs to prompt the so-called double degenerate type Ia supernova. Double-degenerate type Ia supernovae may represent a substantial fraction (if not all) of the type Ia supernovae. Observational evidence for this may lie in the distribution of times between star formation and the type Ia supernova explosion, usually called the delay-time distribution, that seems to favor the double-degenerate scenario (e.g., Maoz et al. 2014) or in the lack of hydrogen lines that are expected in the single-degenerate (WD with a stellar companion) scenario (e.g., Shappee et al. 2013). There are different theoretical models that address the double-degenerate type Ia supernova formation. In the context of triple-body interactions, the large eccentricities associated with the EKL mechanism can lead to double-degenerate type Ia supernovae (e.g., Thompson 2011, Hamers et al. 2013, Prodan et al. 2013). Considering more compact systems, the inner orbit specific angular momentum is likely to reach almost zero (i.e., an almost radial motion) on timescales on the order of the inner orbit period (see Section 3), causing the collision of two WDs and resulting in a type Ia supernova (e.g., Katz & Dong 2012, Kushnir et al. 2013, Dong et al. 2015).

Another interesting astrophysical application for the insight gained in the study of triples is considering higher multiples. There are, of course, many ways to address high multiples interactions.

The first is to consider a scattering, short-timescale event, which has been discussed at length in the literature (e.g., Hut & Bahcall 1983, Rasio & Ford 1996, Chatterjee et al. 2008, Nagasawa et al. 2008, Antognini & Thompson 2016). In a stable system, which does not undergo a scattering event, the additional fourth (or more) companion can have large effects on the eccentricity and inclination evolution. In particular it can help in tapping into large parts of the parameter space (e.g., Takeda et al. 2008, Touma et al. 2009, Pejcha et al. 2013, Boué & Fabrycky 2014a, Hamers et al. 2015) and affect the spin orbit evolution (e.g., Boué & Fabrycky 2014b, Li et al. 2014c). A consequence of the latter effect is that circumbinary planets may be misaligned (e.g., Hamers et al. 2016, Martin et al. 2015, Muñoz & Lai 2015). In the context of the secular approximation, the Gauss averaging method can be utilized for N number of stable orbits (e.g., Touma et al. 2009). This method is a phase-averaged calculation for which the gravitational interactions between nonresonant orbits are equivalent in treating the orbits as massive wires interacting with each other, where the line density is inversely proportional to the orbital velocity. As explained above, a consequence of the secular approximation is that the semimajor axes of the wires are constants of motion (e.g., Murray & Dermott 1999). In general this method can be used to explore different many-body secular effects, for example, the evolution of a particle disk in the presence of a perturber (Batygin 2012).

7. SUMMARY

The high abundance of hierarchical triple systems in nature motivates the investigation of their dynamics. Furthermore, this approximation seems to be very useful in addressing a variety of puzzles and systems that are observed, such as retrograde hot Jupiters, blue stragglers, LMXBs and HMXBs, compact object binaries, double-degenerate type Ia supernovae, etc. Building on the physical understanding gained in recent years in this subject motivates us to go beyond the approximation for an even wider range of applications.

The recent theoretical developments can be summarized by the following:

- The z -component of the angular momentum of the inner and outer orbits (i.e., the nominal $\sqrt{1 - e_{1,2}^2} \cos i_{1,2}$) is only conserved if one of the binary members is a test particle and the outer orbit is axisymmetric ($e_2 = 0$).
- Relaxing any of these assumptions may lead to high-order resonances characterized by large eccentricity excitations and flips of the orbital orientation as well as chaotic behavior.
- These high-order resonances allow the system to tap into larger parts of the initial parameter space for which the EKL mechanism is triggered.
- Short-range forces and other physical processes (such as GR and stellar mass loss) can also retrigger the EKL mechanism for systems that did not exhibit these dynamics in the point-mass approximation.

The field continues to develop and to go beyond three-body systems and the secular or hierarchical approximations. These improvements allow for application to, and understanding of, a larger variety of systems. The intuition and insight that the eccentric Kozai-Lidov mechanism has provided are utilized for these approaches.

DISCLOSURE STATEMENT

The author is not aware of any affiliations, memberships, funding, or financial holdings that might be perceived as affecting the objectivity of this review.

ACKNOWLEDGMENTS

I greatly thank Fred Rasio, Brad Hansen, Gongjie Li, Diego Muñoz, Boaz Katz, Subo Dong, Fabio Antonini, John Forbes, and Thomas Tauris for useful comments. I also thank the referee, Ruth Murray-Clay, for reading the review thoroughly and providing useful suggestions. Furthermore, I deeply thank Alexander Stephan for reading the draft in great detail. I thank J. Antognini, B. Katz, G. Li, B. Liu, C. Petrovich, and J. Teysandier for sharing figures. I acknowledge partial support from the Sloan Foundation Research Fellowships as well as the Annie Jump Cannon Award.

LITERATURE CITED

- Albrecht S, Reffert S, Snellen IAG, Winn JN. 2009. *Nature* 461:373–76
- Albrecht S, Setiawan J, Torres G, Fabrycky DC, Winn JN. 2013. *Ap. J.* 767:32
- Albrecht S, Winn JN, Carter JA, Snellen IAG, de Mooij EJW. 2011. *Ap. J.* 726:68
- Albrecht S, Winn JN, Fabrycky DC, Torres G, Setiawan J. 2012a. In *From Interacting Binaries to Exoplanets: Essential Modeling Tools, Proc. IAU Symp.* 282, ed. MT Richards, I Hubeny, pp. 397–98. Cambridge, UK: Cambridge Univ. Press
- Albrecht S, Winn JN, Johnson JA, et al. 2012b. *Ap. J.* 757:18
- Albrecht S, Winn JN, Torres G, et al. 2014. *Ap. J.* 785:83
- Antognini JM, Shappee BJ, Thompson TA, Amaro-Seoane P. 2014. *MNRAS* 439:1079–91
- Antognini JMO. 2015. *MNRAS* 452:3610
- Antognini JMO, Thompson TA. 2016. *MNRAS* 456:4219
- Antonini F, Murray N, Mikkola S. 2014. *Ap. J.* 781:45
- Antonini F, Merritt D. 2012. *Ap. J.* 745:24
- Antonini F, Perets HB. 2012. *Ap. J.* 757:27
- Armstrong DJ, Osborn HP, Brown DJA, et al. 2014. *MNRAS* 444:1873–83
- Bailey ME, Chambers JE, Hahn G. 1992. *Astron. Astrophys.* 257:315–22
- Baron F, Monnier JD, Pedretti E, et al. 2012. *Ap. J.* 752:20
- Batygin K. 2012. *Nature* 491:418–20
- Batygin K, Morbidelli A, Tsiganis K. 2011. *Astron. Astrophys.* 533:A7
- Begelman MC, Blandford RD, Rees MJ. 1980. *Nature* 287:307–9
- Binder B, Williams BF, Kong AKH, et al. 2011. *Ap. J. Lett.* 739:L51
- Blaes O, Lee MH, Socrates A. 2002. *Ap. J.* 578:775–86
- Bode JN, Wegg C. 2014. *MNRAS* 438:573–89
- Borkovits T, Hajdu T, Sztakovics J, et al. 2016. *MNRAS* 455:4136–65
- Boué G, Fabrycky DC. 2014a. *Ap. J.* 789:110
- Boué G, Fabrycky DC. 2014b. *Ap. J.* 789:111
- Brouwer D. 1959. *Astron. J.* 64:378
- Callegari S, Mayer L, Kazantzidis S, et al. 2009. *Ap. J. Lett.* 696:L89–92
- Carruba V, Burns JA, Nicholson PD, Gladman BJ. 2002. *Icarus* 158:434–49
- Chambers JE, Migliorini F. 1997. *Bull. Am. Astron. Soc.* 29:1024
- Chatterjee S, Ford EB, Matsumura S, Rasio FA. 2008. *Ap. J.* 686:580–602
- Chen X, Madau P, Sesana A, Liu FK. 2009. *Ap. J. Lett.* 697:L149–52
- Chen X, Sesana A, Madau P, Liu FK. 2011. *Ap. J.* 729:13
- Chirikov BV. 1979. *Phys. Rep.* 52:263–379
- Chou Y, Grindlay JE. 2001. *Ap. J.* 563(2):934–40
- Cochran WD, Hatzes AP, Butler RP, Marcy GW. 1996. *Bull. Am. Astron. Soc.* 28:1111
- Correia ACM, Laskar J, Farago F, Boué G. 2011. *Celest. Mech. Dyn. Astron.* 111:105
- Čuk M, Burns JA. 2004. *Astron. J.* 128:2518–41
- Dawson RI, Chiang E. 2014. *Science* 346:212–16
- Deacon NR, Kraus AL, Mann AW, et al. 2016. *MNRAS* 455:4212
- Di Matteo T, Springel V, Hernquist L. 2005. *Nature* 433:604–7

- Dong S, Katz B, Kushnir D, Prieto JL. 2015. *MNRAS* 454:61
- Dong S, Katz B, Socrates A. 2013. *Ap. J. Lett.* 763:L2
- Dong S, Katz B, Socrates A. 2014. *Ap. J. Lett.* 781:L5
- Dotti M, Sesana A, Decarli R. 2012. *Adv. Astron.* 2012:3
- Doyle LR, Carter JA, Fabrycky DC, et al. 2011. *Science* 333:1602
- Duncan MJ, Levison HF. 1997. *Science* 276:1670–72
- Eggleton PP, Kiseleva LG, Hut P. 1998. *Ap. J.* 499:853
- Eggleton PP, Kiseleva-Eggleton L. 2001. *Ap. J.* 562:1012–30
- Eggleton PP, Kiseleva-Eggleton L, Dearborn X. 2007. In *Binary Stars as Critical Tools & Tests in Contemporary Astrophysics*, Proc. IAU Symp. 240, ed. WI Hartkopf, EF Guinan, P Harmanec, pp. 347–55. Cambridge, UK: Cambridge Univ. Press
- Fabrycky D, Tremaine S. 2007. *Ap. J.* 669:1298–315
- Fabrycky DC, Johnson ET, Goodman J. 2007. *Ap. J.* 665:754–66
- Fang J, Margot J-L. 2012. *Astron. J.* 143:59
- Ford EB, Joshi KJ, Rasio FA, Zbarsky B. 2000a. *Ap. J.* 528:336–50
- Ford EB, Kozinsky B, Rasio FA. 2000b. *Ap. J.* 535:385–401
- Freire PCC, Bassa CG, Wex N, et al. 2011. *MNRAS* 412:2763–80
- Frewen S, Hansen BMS. 2016. *MNRAS* 455:1538
- Galaviz P, Brügmann B. 2011. *Phys. Rev. D* 83(8):084013
- Geller AM, Mathieu RD. 2012. *Astron. J.* 144:54
- Gillessen S, Eisenhauer F, Trippe S, et al. 2009. *Ap. J.* 692:1075
- Gillessen S, Genzel R, Fritz TK, et al. 2012. *Nature* 481:51–54
- Goldstein H. 1950. *Classical Mechanics*. Reading, Mass.: Addison-Wesley. 1st ed.
- Gomes RS, Gallardo T, Fernández JA, Brunini A. 2005. *Celest. Mech. Dyn. Astron.* 91:109–29
- Grindlay JE, Bailyn CD, Cohn H, et al. 1988. *Ap. J. Lett.* 334:L25–29
- Gronchi GF, Milani A. 1999. *Astron. Astrophys.* 341:928–35
- Gualandris A, Merritt D. 2009. *Ap. J.* 705:361–71
- Gualandris A, Merritt D. 2012. *Ap. J.* 744:74
- Guillochon J, Ramirez-Ruiz E, Lin D. 2011. *Ap. J.* 732:74
- Hamers AS, Perets HB, Antonini F, et al. 2015. *MNRAS* 449:4221–45
- Hamers AS, Perets HB, Portegies Zwart SF. 2016. *MNRAS* 455:3180
- Hamers AS, Pols OR, Claeys JSW, Nelemans G. 2013. *MNRAS* 430:2262–80
- Hansen BMS. 2010. *Ap. J.* 723:285–99
- Hansen BMS, Zink J. 2015. *MNRAS* 450:4505–20
- Harding LK, Hallinan G, Konopacky QM, et al. 2013. *Astron. Astrophys.* 554:A113
- Harrington RS. 1968. *Astron. J.* 73:190–94
- Harrington RS. 1969. *Celest. Mech.* 1:200–9
- Heintz WD. 1967. *Astron. Nachr.* 289:269
- Hoffman L, Loeb A. 2007. *MNRAS* 377:957–76
- Holman M, Touma J, Tremaine S. 1997. *Nature* 386:254–56
- Hurley JR, Pols OR, Tout CA. 2000. *MNRAS* 315:543–69
- Hut P. 1980. *Astron. Astrophys.* 92:167–70
- Hut P, Bahcall JN. 1983. *Ap. J.* 268:319–41
- Innanen KA, Zheng JQ, Mikkola S, Valtonen MJ. 1997. *Astron. J.* 113:1915
- Ivanov PB, Polnarev AG, Saha P. 2005. *MNRAS* 358:1361–78
- Iwasawa M, An S, Matsubayashi T, Funato Y, Makino J. 2011. *Ap. J. Lett.* 731:L9
- Jefferys WH, Moser J. 1966. *Astron. J.* 71:568–78
- Katz B, Dong S. 2012. The rate of WD-WD head-on collisions may be as high as the SNe Ia rate.
arXiv:1211.4584
- Katz B, Dong S, Malhotra R. 2011. *Phys. Rev. Lett.* 107:1101
- Khan FM, Berentzen I, Berczik P, et al. 2012. *Ap. J.* 756:30
- Kinoshita H, Nakai H. 1991. *Celest. Mech. Dyn. Astron.* 52:293–303
- Kinoshita H, Nakai H. 1999. *Celest. Mech. Dyn. Astron.* 75:125–47

- Kinoshita H, Nakai H. 2007. *Celest. Mech. Dyn. Astron.* 98:67–74
- Kiseleva LG, Eggleton PP, Mikkola S. 1998. *MNRAS* 300:292–302
- Knutson HA, Fulton BJ, Montet BT, et al. 2014. *Ap. J.* 785:126
- Kocsis B, Tremaine S. 2011. *MNRAS* 412:187–207
- Kocsis B, Tremaine S. 2015. *MNRAS* 448:3265–96
- Kostov VB, McCullough PR, Carter JA, et al. 2014. *Ap. J.* 784:14
- Kostov VB, McCullough PR, Hinse TC, et al. 2013. *Ap. J.* 770:52
- Kozai Y. 1962. *Astron. J.* 67:591
- Kozai Y. 1979. In *Dynamics of the Solar System, Proc. IAU Symp.* 81, ed. RL Duncombe, pp. 231–36. Cambridge, UK: Cambridge Univ. Press
- Kratter KM, Perets HB. 2012. *Ap. J.* 753:91
- Kroupa P. 1995. *MNRAS* 277:1507
- Kulkarni G, Loeb A. 2012. *MNRAS* 422:1306–23
- Kushnir D, Katz B, Dong S, Livne E, Fernández R. 2013. *Ap. J. Lett.* 778:L37
- Lanza AF, Shkolnik EL. 2014. *MNRAS* 443:1451–62
- Levesque EM, Massey P, Żytkow AN, Morrell N. 2014. *MNRAS* 443:L94–98
- Levrard B, Correia ACM, Chabrier G, et al. 2007. *Astron. Astrophys.* 462:L5–8
- Li G, Naoz S, Holman M, Loeb A. 2014a. *Ap. J.* 791:86. Erratum. 2015. *Ap. J.* 802:71
- Li G, Naoz S, Kocsis B, Loeb A. 2014b. *Ap. J.* 785:116
- Li G, Naoz S, Kocsis B, Loeb A. 2015. *MNRAS* 451:1341–49
- Li G, Naoz S, Valsecchi F, Johnson JA, Rasio FA. 2014c. *Ap. J.* 794:131
- Lidov ML. 1962. *Planet. Space Sci.* 9:719–59
- Lidov ML, Ziglin SL. 1974. *Celest. Mech.* 9:151–73
- Lidov ML, Ziglin SL. 1976. *Celest. Mech.* 13:471–89
- Lin DNC, Papaloizou J. 1986. *Ap. J.* 309:846–57
- Lithwick Y, Naoz S. 2011. *Ap. J.* 742:94
- Lithwick Y, Wu Y. 2012. *Ap. J. Lett.* 756:L11
- Liu B, Muñoz DJ, Lai D. 2015. *MNRAS* 447:747–64
- Liu S-F, Guillochon J, Lin DNC, Ramirez-Ruiz E. 2013. *Ap. J.* 762:37
- Luo L, Katz B, Dong S. 2016. *MNRAS* 458:3060
- Madigan A-M, Levin Y. 2012. *Ap. J.* 754:42
- Mandel I, Brown DA, Gair JR, Miller MC. 2008. *Ap. J.* 681:1431–47
- Maoz D, Mannucci F, Nelemans G. 2014. *Annu. Rev. Astron. Astrophys.* 52:107–70
- Marchal C. 1990. *The Three-Body Problem*. Amsterdam: Elsevier
- Mardling RA, Aarseth SJ. 2001. *MNRAS* 321:398–420
- Margot J-L, Pravec P, Taylor P, Carry B, Jacobson S. 2015. In *Asteroids IV*, ed. P Michel, FE DeMeo, WF Bottke, pp. 355–74. Tucson, AZ: Univ. Ariz. Press
- Martin DV, Mazeh T, Fabrycky DC. 2015. *MNRAS* 453:3554–67
- Martin DV, Triaid AHMJ. 2015a. *MNRAS* 449:781–93
- Martin DV, Triaid AHMJ. 2015b. *MNRAS* 455(1):L46–50
- Masset FS, Papaloizou JCB. 2003. *Ap. J.* 588:494–508
- Mazeh T, Krymowski Y, Rosenfeld G. 1997. *Ap. J. Lett.* 477:L103–6
- Mazeh T, Shaham J. 1979. *Astron. Astrophys.* 77:145–51
- McKenna J, Lyne AG. 1988. *Nature* 336:226
- Meiron Y, Laor A. 2013. *MNRAS* 433:2502–10
- Merritt D, Alexander T, Mikkola S, Will CM. 2010. *Phys. Rev. D* 81(6):062002
- Merritt D, Vasiliev E. 2012. *Phys. Rev. D* 86(10):102002
- Michaely E, Perets HB. 2014. *Ap. J.* 794:122
- Miller MC, Hamilton DP. 2002. *Ap. J.* 576:894–98
- Milosavljević M, Merritt D. 2001. *Ap. J.* 563:34–62
- Misner CW, Thorne KS, Wheeler JA. 1973. *Gravitation*. San Francisco: W.H. Freeman
- Moeckel N, Veras D. 2012. *MNRAS* 422:831–40
- Morbidelli A. 2002. *Modern Celestial Mechanics: Aspects of Solar System Dynamics*. London: Taylor & Francis

- Morton TD, Johnson JA. 2011. *Ap. J.* 729:138
- Muñoz DJ, Lai D. 2015. *PNAS* 112:9264–69
- Murray CD, Dermott SF. 1999. *Solar System Dynamics*. Cambridge, UK: Cambridge Univ. Press
- Murray N, Holman M. 1997. *Astron. J.* 114:1246–59
- Nagasawa M, Ida S. 2011. *Ap. J.* 742:72
- Nagasawa M, Ida S, Bessho T. 2008. *Ap. J.* 678:498–508
- Naoz S, Fabrycky DC. 2014. *Ap. J.* 793:137
- Naoz S, Farr WM, Lithwick Y, Rasio FA, Teysandier J. 2011. *Nature* 473:187–89
- Naoz S, Farr WM, Lithwick Y, Rasio FA, Teysandier J. 2013a. *MNRAS* 431:2155–71
- Naoz S, Farr WM, Rasio FA. 2012. *Ap. J. Lett.* 754:L36
- Naoz S, Fragos T, Geller A, Stephan SP, Rasio FA. 2016. *Ap. J. Lett.* 822:L24
- Naoz S, Kocsis B, Loeb A, Yunes N. 2013b. *Ap. J.* 773:187
- Naoz S, Perets HB, Ragozzine D. 2010. *Ap. J.* 719:1775–83
- Naoz S, Silk J. 2014. *Ap. J.* 795:102
- Nesvorný D, Alvarillos JLA, Dones L, Levison HF. 2003. *Astron. J.* 126:398–429
- Nesvorný D, Vokrouhlický D, Bottke WF, Noll K, Levison HF. 2011. *Astron. J.* 141:159
- Ngo H, Knutson HA, Hinkley S, et al. 2015. *Ap. J.* 800:138
- O’Leary RM, Rasio FA, Fregeau JM, Ivanova N, O’Shaughnessy R. 2006. *Ap. J.* 637:937–51
- Orosz JA, Welsh WF, Carter JA, et al. 2012a. *Ap. J.* 758:87
- Orosz JA, Welsh WF, Carter JA, et al. 2012b. *Science* 337:1511
- Pejcha O, Antognini JM, Shappee BJ, Thompson TA. 2013. *MNRAS* 435:943–51
- Perets HB, Fabrycky DC. 2009. *Ap. J.* 697:1048–56
- Perets HB, Kratter KM. 2012. *Ap. J.* 760:99
- Perets HB, Naoz S. 2009. *Ap. J. Lett.* 699:L17–21
- Petrovich C. 2015a. *Ap. J.* 799:27
- Petrovich C. 2015b. *Ap. J.* 805:75
- Petrovich C. 2015c. *Ap. J.* 808:120
- Podsiadlowski P, Rappaport S, Han Z. 2003. *MNRAS* 341:385–404
- Polishook D, Brosch N. 2006. Presented at NASA’s “Near-Earth Object Detect., Charact., and Threat Mitig.” workshop, June 2006, Colorado. arXiv:0607128
- Polishook D, Brosch N. 2009. *Icarus* 199:319–32
- Pravec P, Scheirich P, Kusnirák P, et al. 2006. *Icarus* 181:63–93
- Pribulla T, Rucinski SM. 2006. *Astron. J.* 131:2986–3007
- Prodan S, Antonini F, Perets HB. 2015. *Ap. J.* 799:118
- Prodan S, Murray N. 2012. *Ap. J.* 747(1):4
- Prodan S, Murray N, Thompson TA. 2013. arXiv:1305.2191
- Quinn T, Tremaine S, Duncan M. 1990. *Ap. J.* 355:667–79
- Raghavan D, Henry TJ, Mason BD, et al. 2006. *Ap. J.* 646:523–42
- Raghavan D, McAlister HA, Henry TJ, et al. 2010. *Ap. J. Suppl.* 190:1–42
- Ransom SM, Stairs IH, Archibald AM, et al. 2014. *Nature* 505(7484):520–24
- Rasio FA. 2001. In *Evolution of Binary and Multiple Star Systems; A Meeting in Celebration of Peter Eggleton’s 60th Birthday*, ed. P Podsiadlowski, S Rappaport, AR King, F D’Antona, L Burderi. *ASP Conf. Ser.* 229:117. San Francisco: ASP
- Rasio FA, Ford EB. 1996. *Science* 274:954–56
- Rice K. 2015. *MNRAS* 448:1729–37
- Schwamb ME, Orosz JA, Carter JA, et al. 2013. *Ap. J.* 768:127
- Sesana A, Gualandris A, Dotti M. 2011. *MNRAS* 415:L35–39
- Seto N. 2013. *Phys. Rev. Lett.* 111(6):061106
- Shappee BJ, Stanek KZ, Pogge RW, Garnavich PM. 2013. *Ap. J. Lett.* 762:L5
- Shappee BJ, Thompson TA. 2013. *Ap. J.* 766:64
- Sigurdsson S, Richer HB, Hansen BM, Stairs IH, Thorsett SE. 2003. *Science* 301(5):193–96
- Söderhjelm S. 1975. *Astron. Astrophys.* 42:229–36
- Soderhjelm S. 1982. *Astron. Astrophys.* 107:54–60

- Söderhjelm S. 1984. *Astron. Astrophys.* 141:232–40
- Stephan AP, Naoz S, Ghez AM, et al. 2016. *MNRAS* 460(4):3494–504
- Storch NI, Anderson KR, Lai D. 2014. *Science* 345:1317–21
- Storch NI, Lai D. 2015. *MNRAS* 448:1821–34
- Takeda G, Kita R, Rasio FA. 2008. *Ap. J.* 683:1063–75
- Tamayo D, Burns JA, Hamilton DP. 2013. *Icarus* 226:655–62
- Tauris TM, van den Heuvel EPJ. 2014. *Ap. J. Lett.* 781(1):L13
- Teyssandier J, Naoz S, Lizarraga I, Rasio FA. 2013. *Ap. J.* 779:166
- Thomas F, Morbidelli A. 1996. *Celest. Mech. Dyn. Astron.* 64:209–29
- Thompson TA. 2011. *Ap. J.* 741:82
- Thorne KS, Zytlow AN. 1975. *Ap. J. Lett.* 199:L19–24
- Thorsett SE, Arzoumanian Z, Camilo F, Lyne AG. 1999. *Ap. J.* 523(2):763–70
- Tokovinin A. 2008. *MNRAS* 389:925–38
- Tokovinin A. 2014a. *Astron. J.* 147:86
- Tokovinin A. 2014b. *Astron. J.* 147:87
- Tokovinin AA. 1997. *Astron. Lett.* 23:727–30
- Tokovinin AA, Smekhov MG. 2002. *Astron. Astrophys.* 382:118–23
- Touma JR, Tremaine S, Kazandjian MV. 2009. *MNRAS* 394:1085–108
- TriAUD AHMJ, Collier Cameron A, Queloz D, et al. 2010. *Astron. Astrophys.* 524:A25
- TriAUD AHMJ, Hebb L, Anderson DR, et al. 2013. *Astron. Astrophys.* 549:A18
- Valtonen M, Karttunen H. 2006. *The Three-Body Problem*. Cambridge, UK: Cambridge Univ. Press
- Valtonen MJ. 1996. *MNRAS* 278:186–90
- Vashkov'yak MA. 1999. *Astron. Lett.* 25:476–81
- Veras D, Evans NW, Wyatt MC, Tout CA. 2014. *MNRAS* 437:1127–40
- Veras D, Ford EB. 2010. *Ap. J.* 715:803–22
- Veras D, Mustill AJ, Bonsor A, Wyatt MC. 2013. *MNRAS* 431:1686–708
- Veras D, Tout CA. 2012. *MNRAS* 422:1648–64
- Wang J, Fischer DA, Horch EP, Xie J-W. 2015. *Ap. J.* 806:248
- Wang L, Berczik P, Spurzem R, Kouwenhoven MBN. 2014. *Ap. J.* 780:164
- Welsh WF, Orosz JA, Carter JA, et al. 2012. *Nature* 481:475–79
- Welsh WF, Orosz JA, Short DR, et al. 2015. *Ap. J.* 809:26
- Wen L. 2003. *Ap. J.* 598:419–30
- Will CM. 2014a. *Class. Quantum Gravity* 31(24):244001
- Will CM. 2014b. *Phys. Rev. D* 89(4):044043
- Winn JN, Fabrycky D, Albrecht S, Johnson JA. 2010. *Ap. J. Lett.* 718:L145–49
- Wisdom J, Holman M. 1991. *Astron. J.* 102:1528–38
- Witzel G, Ghez AM, Morris MR, et al. 2014. *Ap. J. Lett.* 796:L8
- Wu Y, Murray N. 2003. *Ap. J.* 589:605–14
- Wu Y, Murray NW, Ramsahai JM. 2007. *Ap. J.* 670:820–25
- Yokoyama T, Santos MT, Cardin G, Winter OC. 2003. *Astron. Astrophys.* 401:763–72
- Yu Q. 2002. *MNRAS* 331:935–58
- Yunes N, Miller MC, Thornburg J. 2011. *Phys. Rev. D* 83(4):044030
- Zdziarski AA, Wen L, Gierliński M. 2007. *MNRAS* 377(3):1006–16
- Zhou G, Huang CX. 2013. *Ap. J. Lett.* 776:L35



Contents

A Fortunate Half-Century <i>Jeremiah P. Ostriker</i>	1
The Remnant of Supernova 1987A <i>Richard McCray and Claes Fransson</i>	19
Astrophysics with Extraterrestrial Materials <i>Larry R. Nittler and Fred Ciesla</i>	53
Red Clump Stars <i>Léo Girardi</i>	95
Accretion onto Pre-Main-Sequence Stars <i>Lee Hartmann, Gregory Herczeg, and Nuria Calvet</i>	135
Interstellar Hydrides <i>Maryvonne Gerin, David A. Neufeld, and Javier R. Goicoechea</i>	181
The Quest for B Modes from Inflationary Gravitational Waves <i>Marc Kamionkowski and Ely D. Kovetz</i>	227
Gravitational Instabilities in Circumstellar Disks <i>Kaitlin Kratter and Giuseppe Lodato</i>	271
The Evolution of the Intergalactic Medium <i>Matthew McQuinn</i>	313
The Magellanic Stream: Circumnavigating the Galaxy <i>Elena D'Onghia and Andrew J. Fox</i>	363
Masses, Radii, and the Equation of State of Neutron Stars <i>Feryal Özel and Paulo Freire</i>	401
The Eccentric Kozai-Lidov Effect and Its Applications <i>Smadar Naoz</i>	441
Protostellar Outflows <i>John Bally</i>	491

The Galaxy in Context: Structural, Kinematic, and Integrated Properties <i>Joss Bland-Hawthorn and Ortwin Gerhard</i>	529
Structure and Kinematics of Early-Type Galaxies from Integral Field Spectroscopy <i>Michele Cappellari</i>	597
Six Decades of Spiral Density Wave Theory <i>Frank H. Shu</i>	667
Gamma-Ray Observations of Active Galactic Nuclei <i>Grzegorz (Greg) Madejski and Marek Sikora</i>	725
Galaxies in the First Billion Years After the Big Bang <i>Daniel P. Stark</i>	761

Indexes

Cumulative Index of Contributing Authors, Volumes 43–54	805
Cumulative Index of Article Titles, Volumes 43–54	808

Errata

An online log of corrections to *Annual Review of Astronomy and Astrophysics* articles may be found at <http://www.annualreviews.org/errata/astro>

SUPPLEMENTAL TEXT 1: THE SECULAR EQUATIONS

The full octupole-order equations of motion for the most general case (i.e., relaxing the test particle and axisymmetric potential approximations) presented in Naoz et al. (2013a) are reiterated here for completeness. We begin with reminding the reader of the definitions of a few useful parameters:

$$\begin{aligned} C_3 &= -\frac{15}{16} \frac{k^4}{4} \frac{(m_1 + m_2)^9}{(m_1 + m_2 + m_3)^4} \frac{m_3^9 (m_1 - m_2)}{(m_1 m_2)^5} \frac{L_1^6}{L_2^3 G_2^5} \\ &= -C_2 \frac{15}{4} \frac{\epsilon_M}{e_2} \end{aligned} \quad (67)$$

where

$$\epsilon_M = \frac{m_1 - m_2}{m_1 + m_2} \frac{a_1}{a_2} \frac{e_2}{1 - e_2^2} \quad (68)$$

and

$$A = 4 + 3e_1^2 - \frac{5}{2} B \sin^2 i_{\text{tot}}, \quad (69)$$

where

$$B = 2 + 5e_1^2 - 7e_1^2 \cos(2\omega_1), \quad (70)$$

and

$$\cos \phi = -\cos \omega_1 \cos \omega_2 - \cos i_{\text{tot}} \sin \omega_1 \sin \omega_2. \quad (71)$$

As shown in Naoz et al. (2013a) elimination of the nodes (i.e., setting $\Omega_1 - \Omega_2 = \pi$) can be done as long as one does not conclude that the conjugate z -component of the angular momenta (H_1 and H_2) are constant of motion. The partial derivatives with respect to the other coordinates and momenta are not affected by the substitution $\Omega_1 - \Omega_2 = \pi$. In that case, the time evolution of H_1 and H_2 (and thus i_1 and i_2) can be derived from the total angular momentum conservation. The doubly averaged Hamiltonian after eliminating the nodes:

$$\begin{aligned} \mathcal{H}(\Delta h \rightarrow \pi) &= C_2 \{ (2 + 3e_1^2) (3 \cos^2 i_{\text{tot}} - 1) \\ &\quad + 15e_1^2 \sin^2 i_{\text{tot}} \cos(2\omega_1) \} \\ &\quad + C_3 e_1 e_2 \{ A \cos \phi \\ &\quad + 10 \cos i_{\text{tot}} \sin^2 i_{\text{tot}} (1 - e_1^2) \sin \omega_1 \sin \omega_2 \}. \end{aligned} \quad (72)$$

The time evolution of the argument of periaapse for the inner and outer orbits are given by:

$$\begin{aligned} \dot{\omega}_1 &= 6C_2 \left\{ \frac{1}{G_1} [4 \cos^2 i_{\text{tot}} + (5 \cos(2\omega_1) - 1) \right. \\ &\quad \times (1 - e_1^2 - \cos^2 i_{\text{tot}})] + \frac{\cos i_{\text{tot}}}{G_2} [2 + e_1^2 (3 - 5 \cos(2\omega_1))] \left. \right\} \\ &\quad - C_3 e_2 \left\{ e_1 \left(\frac{1}{G_2} + \frac{\cos i_{\text{tot}}}{G_1} \right) \right. \\ &\quad \times [\sin \omega_1 \sin \omega_2 (10(3 \cos^2 i_{\text{tot}} - 1)(1 - e_1^2) + A) \\ &\quad \left. - 5B \cos i_{\text{tot}} \cos \phi] - \frac{1 - e_1^2}{e_1 G_1} \times [\sin \omega_1 \sin \omega_2 \right. \end{aligned} \quad (73)$$

$$\left. \begin{aligned} & \times 10 \cos i_{\text{tot}} \sin i_{\text{tot}}^2 (1 - 3e_1^2) \\ & + \cos \phi (3A - 10 \cos i_{\text{tot}}^2 + 2) \end{aligned} \right\},$$

and

$$\begin{aligned} \dot{\omega}_2 = & 3C_2 \left\{ \frac{2 \cos i_{\text{tot}}}{G_1} [2 + e_1^2 (3 - 5 \cos(2\omega_1))] \right. \\ & + \frac{1}{G_2} [4 + 6e_1^2 + (5 \cos^2 i_{\text{tot}} - 3)(2 + e_1^2 [3 - 5 \cos(2\omega_1)])] \left. \right\} \\ & + C_3 e_1 \left\{ \sin \omega_1 \sin \omega_2 \left(\frac{4e_2^2 + 1}{e_2 G_2} 10 \cos i_{\text{tot}} \sin^2 i_{\text{tot}} (1 - e_1^2) \right. \right. \\ & - e_2 \left(\frac{1}{G_1} + \frac{\cos i_{\text{tot}}}{G_2} \right) [A + 10(3 \cos^2 i_{\text{tot}} - 1)(1 - e_1^2)] \left. \right. \\ & \left. + \cos \phi \left[5B \cos i_{\text{tot}} e_2 \left(\frac{1}{G_1} + \frac{\cos i_{\text{tot}}}{G_2} \right) + \frac{4e_2^2 + 1}{e_2 G_2} A \right] \right\} \end{aligned} \quad (74)$$

The time evolution of the longitude of ascending nodes is given by:

$$\begin{aligned} \dot{\Omega}_1 = & -\frac{3C_2}{G_1 \sin i_1} (2 + 3e_1^2 - 5e_1^2 \cos(2\omega_1)) \sin(2i_{\text{tot}}) \\ & - C_3 e_1 e_2 [5B \cos i_{\text{tot}} \cos \phi \\ & - A \sin \omega_1 \sin \omega_2 + 10(1 - 3 \cos^2 i_{\text{tot}}) \\ & \times (1 - e_1^2) \sin \omega_1 \sin \omega_2] \frac{\sin i_{\text{tot}}}{G_1 \sin i_1}, \end{aligned} \quad (75)$$

where in the last part we have used again the law of sines for which $\sin i_1 = G_2 \sin i_{\text{tot}} / G_{\text{tot}}$. The evolution of the longitude of ascending nodes for the outer orbit can be easily obtained using:

$$\dot{\Omega}_2 = \dot{\Omega}_1. \quad (76)$$

The evolution of the inner and outer eccentricities is:

$$\begin{aligned} \dot{e}_1 = & C_2 \frac{1 - e_1^2}{G_1} [30e_1 \sin^2 i_{\text{tot}} \sin(2\omega_1)] \\ & + C_3 e_2 \frac{1 - e_1^2}{G_1} [35 \cos \phi \sin^2 i_{\text{tot}} e_1^2 \sin(2\omega_1) \\ & - 10 \cos i_{\text{tot}} \sin^2 i_{\text{tot}} \cos \omega_1 \sin \omega_2 (1 - e_1^2) \\ & - A(\sin \omega_1 \cos \omega_2 - \cos i_{\text{tot}} \cos \omega_1 \sin \omega_2)], \end{aligned} \quad (77)$$

and

$$\begin{aligned} \dot{e}_2 = & -C_3 e_1 \frac{1 - e_2^2}{G_2} [10 \cos(i_{\text{tot}}) \sin^2(i_{\text{tot}}) (1 - e_1^2) \sin \omega_1 \cos \omega_2 \\ & + A(\cos \omega_1 \sin \omega_2 - \cos(i_{\text{tot}}) \sin \omega_1 \cos \omega_2)]. \end{aligned} \quad (78)$$

The angular momenta derivatives of the inner and outer orbits as a function of time can be easily calculated, where for the inner orbit we write:

$$\dot{G}_1 = -C_2 30e_1^2 \sin(2\omega_1) \sin^2(i_{\text{tot}}) + C_3 e_1 e_2 (\quad (79)$$

$$\begin{aligned}
& - 35e_1^2 \sin^2(i_{\text{tot}}) \sin(2\omega_1) \cos \phi + A[\sin \omega_1 \cos \omega_2 \\
& - \cos(i_{\text{tot}}) \cos \omega_1 \sin \omega_2] \\
& + 10 \cos(i_{\text{tot}}) \sin^2(i_{\text{tot}})[1 - e_1^2] \cos \omega_1 \sin \omega_2 ,
\end{aligned}$$

and for the outer orbit (where the quadrupole term is zero)

$$\begin{aligned}
\dot{G}_2 &= C_3 e_1 e_2 [A\{\cos \omega_1 \sin \omega_2 - \cos(i_{\text{tot}}) \sin \omega_1 \cos \omega_2\} \\
& + 10 \cos(i_{\text{tot}}) \sin^2(i_{\text{tot}})[1 - e_1^2] \sin \omega_1 \cos \omega_2].
\end{aligned} \tag{80}$$

Also the z -component of the inner orbit angular momentum is

$$\dot{H}_1 = \frac{G_1}{G_{\text{tot}}} \dot{G}_1 - \frac{G_2}{G_{\text{tot}}} \dot{G}_2, \tag{81}$$

where using the law of sines we write:

$$\dot{H}_1 = \frac{\sin i_2}{\sin i_{\text{tot}}} \dot{G}_1 - \frac{\sin i_1}{\sin i_{\text{tot}}} \dot{G}_2. \tag{82}$$

Because the total angular momentum is conserved $G_{\text{tot}} = \text{Const.} = H_1 + H_2$ the outer orbit z -component time evolution is simply $\dot{H}_2 = -\dot{H}_1$. The inclinations equation of motion is

$$(\dot{\cos i_1}) = \frac{\dot{H}_1}{G_1} - \frac{\dot{G}_1}{G_1} \cos i_1, \tag{83}$$

and

$$(\dot{\cos i_2}) = \frac{\dot{H}_2}{G_2} - \frac{\dot{G}_2}{G_2} \cos i_2. \tag{84}$$

SUPPLEMENTAL TEXT 2: STATIC TIDES EQUATIONS

Tidal interaction considered in this review are limited to the inner orbit members equilibrium and static tides formalism (e.g., Hut 1980, Eggleton et al. 1998, Kiseleva et al. 1998, Eggleton & Kiseleva-Eggleton 2001). A compact representation of the tidal interactions equation can be found when using the Laplace- Runge-Lenz vector system. In this system the three vector base is composed from the inner orbit eccentricity vector \mathbf{e}_1 the specific angular momentum vector

$$\mathbf{J}_1 = \sqrt{k^2(m_1 + m_2)a_1(1 - e_1^2)}\hat{\mathbf{J}}_1 = \mathbf{G}_1(m_1 + m_2)/(m_1m_2). \quad (85)$$

The vector $\hat{\mathbf{q}} = \hat{\mathbf{J}}_1 \times \hat{\mathbf{e}}_1$ completes the right-hand triad of unit vectors $(\hat{\mathbf{q}}, \hat{\mathbf{J}}_1, \hat{\mathbf{e}}_1)$. Each of the inner member masses have a spin vector $\boldsymbol{\Omega}_{s1}$ and $\boldsymbol{\Omega}_{s2}$, respectively. The time evolution equations are (where subscript 1 and 2 refer to masses m_1 and m_2):

$$\frac{1}{e_1} \frac{d\mathbf{e}_1}{dt} = (Z_1 + Z_2)\hat{\mathbf{q}} - (Y_1 + Y_2)\hat{\mathbf{J}}_1 - (V_1 + V_2)\hat{\mathbf{e}}_1, \quad (86)$$

$$\frac{1}{J_1} \frac{d\mathbf{J}_1}{dt} = -(X_1 + X_2)\hat{\mathbf{q}} - (W_1 + W_2)\hat{\mathbf{J}}_1 + (Y_1 + Y_2)\hat{\mathbf{e}}_1, \quad (87)$$

$$I_1 \frac{d\boldsymbol{\Omega}_{s1}}{dt} = \mu J_1 (X_1 \hat{\mathbf{q}} + W_1 \hat{\mathbf{J}}_1 - Y_1 \hat{\mathbf{e}}_1), \quad (88)$$

$$I_2 \frac{d\boldsymbol{\Omega}_{s2}}{dt} = \mu J_1 (X_2 \hat{\mathbf{q}} + W_2 \hat{\mathbf{J}}_1 - Y_2 \hat{\mathbf{e}}_1), \quad (89)$$

where $\mu = m_1m_2/(m_1 + m_2)$ is the reduced mass, I_1 (I_2) is the moment of inertia of mass m_1 (m_2). The vector (X, Y, Z) is the angular velocity of the $(\hat{\mathbf{q}}, \hat{\mathbf{J}}_1, \hat{\mathbf{e}}_1)$ frame and can be easily related to the Delaunay's elements in the invariable plan as (Eggleton et al. 1998):

$$X = \frac{di_1}{dt} \cos \omega_1 + \frac{d\Omega_1}{dt} \sin \omega_1 \sin i_1, \quad (90)$$

$$Y = -\frac{di_1}{dt} \sin \omega_1 + \frac{d\Omega_1}{dt} \cos \omega_1 \sin i_1, \quad (91)$$

$$Z = \frac{d\omega_1}{dt} + \frac{d\Omega_1}{dt} \cos i_1 \quad (92)$$

This set of equations gives the precession rate due to tides $d\omega_1/dt$ as well as how the other Delaunay's elements vary with time. We note that these equations (Equations 86–89) are identical to that of Eggleton & Kiseleva-Eggleton (2001) and Fabrycky & Tremaine (2007), up to the gravitational influence of the third body which they described by the tensor \mathbf{S} . In our formalism its redundant. The functional form of W, V, X, Y and Z were given in Eggleton & Kiseleva-Eggleton (2001) and are simply:

$$V_1 = \frac{9}{t_{F1}} \left(\frac{1 + 15e_1^2/4 + 15e_1^4/8 + 5e_1^6/64}{(1 - e_1^2)^{13/2}} - \frac{11\Omega_{s1,J}}{18n} \frac{1 + 3e_1^2/2 + e_1^4/8}{(1 - e_1^2)^5} \right), \quad (93)$$

$$W_1 = \frac{1}{t_{F1}} \left(\frac{1 + 15e_1^2/2 + 45e_1^4/8 + 5e_1^6/16}{(1 - e_1^2)^{13/2}} - \frac{11\Omega_{s1,J}}{n} \frac{1 + 3e_1^2 + 3e_1^4/8}{(1 - e_1^2)^5} \right), \quad (94)$$

$$X_1 = -\frac{m_2k_1R_1^5}{\mu na_1^5} \frac{\Omega_{s1,J}\Omega_{s1,e}}{(1 - e_1^2)^2} - \frac{\Omega_{s1,q}}{2nt_{F1}} \frac{1 + 9e_1^2/2 + 5e_1^4/8}{(1 - e_1^2)^5}, \quad (95)$$

$$Y_1 = -\frac{m_2k_1R_1^5}{\mu na_1^5} \frac{\Omega_{s1,J}\Omega_{s1,q}}{(1 - e_1^2)^2} + \frac{\Omega_{s1,e}}{2nt_{F1}} \frac{1 + 3e_1^2/2 + e_1^4/8}{(1 - e_1^2)^5}, \quad (96)$$

$$Z_1 = \frac{m_2k_1R_1^5}{\mu na_1^5} \left(\frac{2\Omega_{s1,J}^2 - \Omega_{s1,q}^2 - \Omega_{1s,e}^2}{2(1 - e_1^2)^2} + \frac{15k^2m_2}{a_1^3} \frac{1 + 3e_1^2/2 + e_1/8}{(1 - e_1^2)^5} \right), \quad (97)$$

where the expression for mass m_2 can be easily found by replacing subscript 1 with 2. The mean motion is

$$n = \frac{2\pi}{P_1} = \sqrt{\frac{k^2(m_1 + m_2)}{a_1^3}}. \quad (98)$$

also, k_1 is classical apsidal motion constant, which is a measure of quadrupolar deformability, and related to the Love parameter of mass m_1 by $k_L = 2k_1$. It also related to Eggleton & Kiseleva-Eggleton (2001) coefficient Q_E by

$$k_1 = \frac{1}{2} \frac{Q_E}{1 - Q_E}. \quad (99)$$

The tidal friction timescale can be expressed in terms of the viscous timescale t_{V1} (which is assume dot be constant in the tides applications in this review):

$$t_{F1} = \frac{t_{V1}}{9} \left(\frac{a_1}{R_1} \right)^8 \frac{m_1^2}{(m_1 + m_2)m_2} \frac{1}{(1 + 2k_1)^2}, \quad (100)$$

and similar equation for t_{F2} can be found by replacing 1 with 2. This formalism describes viscosity that causes the tidal bulge to lag the instantaneous direction of the companion by a constant angle $1/(2Q)$ at constant time interval. The quality factor Q can be expressed as a function of viscous timescale as well by (e.g., Fabrycky & Tremaine 2007, Hansen 2010)

$$Q = \frac{4}{3} \frac{k_1}{(1 + 2k_1)^2} \frac{k^2 m_1 t_{V1}}{R_1^3 n}. \quad (101)$$

REFERENCES

- Eggleton PP, Kiseleva LG, Hut P. 1998. *Ap. J.* 499:853
 Eggleton PP, Kiseleva-Eggleton L. 2001. *Ap. J.* 562:1012–30
 Fabrycky D, Tremaine S. 2007. *Ap. J.* 669:1298–315
 Hansen BMS. 2010. *Ap. J.* 723:285–99 Hut P. 1980. *Astron. Astrophys.* 92:167–70
 Kiseleva LG, Eggleton PP, Mikkola S. 1998. *MNRAS* 300:292–302
 Naoz S, Farr WM, Lithwick Y, Rasio FA, Teysandier J. 2013a. *MNRAS* 431:2155–71